ISSN 2521-6368

Volume 7
Number 2
2023

Journal of Baku Engineering University

PHYSICS

Journal is published twice a year
Number - 1. June, Number - 2. December

An International Journal

http://journal.beu.edu.az

Editor-in-chief

Niftali Qocayev

Co-Editor

Razim Bayramov

Editorial advisory board

Azer Ahmedov (Baku State University, Azerbaijan)
Cahangir Huseynov (Azerbaijan, Azerbaijan Pedagogical University)
Eldar Masimov (Azerbaijan, Baku State University)
Eyyub Guliyev (Azerbaijan, National Academy of Sciences)
Farhad Rustamov (Azerbaijan, İnstitute of Physical Problems)
Gulnara Akhverdiyeva (Azerbaijan, İnstitute of Physical Problems)
Izzet Efendiyeva (Azerbaijan, Baku State University)
Larisa Ismayilova (Azerbaijan, İnstitute of Physical Problems)
Kerim Allakhverdiyev (Azerbaijan, National Aviation Academy of Azerbaijan)
Nadir Gahramanov (Azerbaijan, Baku State University)
Namiq Ahmedov (Azerbaijan, İnstitute of Physical Problems)
Sajida Abdulvahabova (Azerbaijan, Baku State University)

International Advisory board

Ahmed Abdinov (Azerbaijan, Baku State University)
Anar Rustamov (Germany, Hote Frankfurt University)
Ali Javan (USA, Massachusets Institute of Technology)
Adil R. Abduragimov (USA, University of California, Los Angeles)
Amrulla Mamedov (Turkey, Bilkent Universit)
Faig Mikailzade (Turkey, Gebze Technical University, Kocaeli)
Gulshen Agayeva (Azerbaijan, İnstitute of Physical Problems)
Irada Aliyeva (Azerbaijan, Baku State University)
Garib Murshudov (York Akademy,UK, London)
Hamed Sari-Sarraf (USA, Texas Technik University)
Eden Mamut (Romania, Black Sea Universiteties Network Center)
Elsen Veli Veliyev (Turkey, Kocaeli University)
Kamran T. Mahmudov (University of Lisbon, Porugal)
Kev Salihov (Tataristan, Kazan University)
Khalil Kälantär (Displays and Optical Technologies, Japan, Tokio)
Konstantin Voldemarovich Shaitan (Russia, Moskow State Unıversıty)
M.Iqbal Choudhary (University of Karachi, Pakistan)
Natiq M. Atakishiyev (Universidad National Antonoma de Mexico)
Nizami Gasanliy (Middle East Technical University, Turkey)
Oktai Gassumov (Azerbaijan National Academy of Sceince, Baku)
Oguz Gulseren (Bilkent University, Turkey)
Olgun Guven (Turkey, Hacettepe University)
Rasim Mamedov (Azerbaijan, Baku State University)
Rauf Jafarov (Azerbaijan, Institute of Physical Problems)
Sebahattin Tuzemen (Turkey, Ataturk University)
Sevim Akyuz (Turkey, Istanbul University)
S.V. Chernyshenko (Germany, Koblenz University)
Suleyman I. Allakhverdiev (Russian, Akademy Science, Moscow)
Svetlana Demuhamedova (Azerbaijan, İnstitute of Physical Problems)
Takhmasib Aliyev (METU, Ankara,Turkey)
Taleh Yusifov (University of California, USA, Los Angeles)
Tariel Ismayilov (Azerbaijan, Baku State University)
Tarana Aliyeva (Azerbaijan, İnstitute of Physical Problems)
Tarlan Efendiyev (Belarus, National Academy of Science)
Toshi Nagata (Japan, National Institute for Natural Science)
V. Thavasi (Singapore, National University of Singapore)
Vagif Nasirov (Azerbaijan, Azerbaijan Pedagogical University)
Vladimir Pashenko (Russia, Moskow State University)
Veli Gusseynov (National Academy of Science, Baku, Azerbaijan)
Vladimir Gorbarchuk (Poland, Lyubel Polytechnic University)
Yusif Nurullayev (Azerbaijan, Baku State University)
Yusuf Sahin (Turkey, Ataturk University)

Executive Editors

Shafag Alizade

Assistant Editors

Ulker Agayeva
Lala Hajiyeva

Design

Ilham Aliyev

Contact address

Journal of Baku Engineering University
AZ0102, Khirdalan city, Hasan Aliyev str. 120, Absheron, Baku, Azerbaijan
***Tel:** 00 994 12 - 349 99 95 **Fax:** 00 994 12 349-99-90/91*

e-mail: *jr-phisics@beu.edu.az*
web: *http://journal.beu.edu.az*
facebook: *Journal Of Baku Engineering University*

Copyright © Baku Engineering University

ISSN 2521-6368

ISSN 2521-6368

Journal of Baku Engineering University

PHYSICS

Baku - AZERBAIJAN

Journal of Baku Engineering University

PHYSICS

2023. Volume 7, Number 2

CONTENTS

JOURNAL OF BAKU ENGINEERING UNIVERSITY - PHYSICS
2023. Volume 7, Number 2 *Pages 49-56*

UOT:539.196.3
PASC:61.05.-a

CONFORMATIONAL ANALYSIS OF ION BINDING POSSIBILITIES OF SYNTHETIC TETRAPEPTIDE H-ALA-ALA-ASP-ALA-OH (A_3D)

G.A. AGAEVA, N.M. GODJAEV

Institute for Physical Problems, Baku State University,

AZ-1148, Baku, Z.Khalilov Str.23, Azerbaijan

gulshen@mail.ru

ABSTRACT

The conformational peculiarities of synthetic tetrapeptide segment H-Ala-Ala-Asp-Ala-OH in the absence and presence of a model of divalent cation have been investigated by molecular mechanics method. The calculated results permitted to determine the conformational changes of tetrapeptid induced by divalent cation and to suggest the stable structural models of the chelation by tetrapeptide segment, depending on its conformational posibilities. Based on experimental data and the results of theoretical conformational analysis, an energetically preferable model for the chelation of a divalent cation by the tetrapeptide segment Ala-Ala-Asp-Ala is proposed. It is shown that tetrapeptide contain six different sites for binding of divalent ion. A comparison of the obtained calculated structures of the tetrapeptide in the free and ion-bound states made it possible to establish an increase in the conformational stability of the spatial structures of the tetrapeptide segment during the formation of the complex.

Keywords: Synthetic tetrapeptide, spatial structure, conformation, ion binding possibility.

КОНФОРМАЦИОННЫЙ АНАЛИЗ ВОЗМОЖНОСТЕЙ ИОН СВЯЗЫВАНИЯ СИНТЕТИЧЕСКОГО ТЕТРАПЕПТИДНОГО СЕГМЕНТА H-ALA-ALA-ASP-ALA-OH (A_3 D)

РЕЗЮМЕ

Методом молекулярной механики исследованы конформационные особенности синтетического тетрапептидного сегмента H-Ala-Ala-Asp-Ala-OH в отсутствие и в присутствии модельного двухвалентного катиона. Результаты расчетов позволили определить конформационные изменения тетрапептида, индуцированные двухвалентным катионом, и предложить устойчивые структурные модели хелатирования тетрапептидным сегментом в зависимости от его конформационных возможностей. На основе экспериментальных данных и результатов теоретического конформационного анализа предложена энергетически предпочтительная модель хелатирования двухвалентного катиона тетрапептидным сегментом Ala-Ala-Asp-Ala. Показано, что данный тетрапептид содержит шесть разных сайта связывания двухвалентного иона. Сравнение полученных расчетных структур тетрапептида в свободном и ион-связанном состояниях позволило конкретно установить повышение конформационной устойчивости пространственных структур тетрапептидного сегмента при образовании комплекса.

Ключевые слова: синтетический тетрапептид, пространственная структура, конформация, возможность связывания ионов.

SINTETIK H-ALA-ALA-ASP-ALA-OH (A_3D) TETRAPEPTİD SEQMENTİN İON BİRLƏŞDİRMƏ QABİLİYYƏTİNİN KONFORMASİYA ANALİZİ

XÜLASƏ

H-Ala-Ala-Asp-Ala-OH (A_3D) sintetik tetrapeptid seqmentinin konformasiya xüsusiyyətləri model ikivalent kation mövcud olduqda və olmadıqda molekulyar mexanika üsulu ilə tədqiq edilmişdir. Hesablamaların nəticələri ikivalent kation tərəfindən induksiya olunan tetrapeptidin konformasiya dəyişikliklərini təyin etməyə və onun konformasiya imkanlarından asılı olaraq tetrapeptid seqmentinin xelatlaşdırılmasının stabil struktur modellərini təklif etməyə imkan verdi. Eksperimental məlumatlara və nəzəri konformasiya analizinin nəticələrinə əsasən ikivalent kationun Ala-Ala-Asp-Ala tetrapeptid seqmenti ilə

Manuscript receved 26.04.2023

xelatlaşdırılması üçün enerji baxımından əlverişli model təklif olunur. Bu tetrapeptidin altı müxtəlif ikivalentli ion bağlama yeri olduğu göstərildi. Hesablanmış tetrapeptidin strukturlarının sərbəst və ionla bağlı vəziyyətdə müqayisəsi kompleksin əmələ gəlməsi zamanı tetrapeptid seqmentinin fəza strukturlarının konformasiya sabitliyində artımı xüsusi olaraq təyin etməyə imkan verdi.

Açar sözlər: Sintetik tetrapeptid, fəza quruluşu, konformasiya, ion bağlama imkanı.

INTRODUCTION

It is known that metal ions take an active part in the implementation of the functions of various peptide bioregulators. The role of ions, in particular divalent cations, as carriers of signals for controlling a large number of intracellular reactions is now well known. It has been shown that, in addition to a certain functional role, these ions play a significant role in stabilizing the conformation of peptide molecules. Some protein molecules contain regions consisting only of amino acids that allow the formation of strong specific bonds with divalent cations through the oxygen atoms of carbonyl and carboxylate groups [1,2]. In the present work, the conformational features of the model tetrapeptide segment H-Ala-Ala-Asp-Ala-OH, containing an aspartic acid residue, were studied as a simplified model of the ion-binding center in various proteins [3]. The ion-binding capabilities of this model peptide were previously studied by various spectral methods [3]. The conformational features of this tetrapeptide were studied both in the absence and in the presence of a model divalent cation using semi-empirical calculation of intramolecular energy. The results obtained made it possible to determine the most probable spatial structures of chelation of a divalent cation with a peptide depending on its conformational capabilities. When complexing with ions, small fragments of protein molecules appear in direct interaction with the ion. According to modern concepts, potentiation of the activity of peptides by metal ions occurs by stabilizing their active conformation during the formation of ion-peptide complexes. A necessary step in elucidating the mechanism of this process is to study the spatial structure of such ion-binding peptides to determine the type of complex and the degree of its stability, based on the conformational characteristics of the ligand peptide. Only a very specific conformation of the molecule creates the necessary conditions for ion binding to occur. In [3] the interactions of the tetrapeptide Ala-Ala-Asp-Ala (A_3D) with a divalent cation were studied potentiometrically and by optical CD and EPR spectroscopy methods. The formation of three types of complexes between the cation and A3D was recorded, differing in the number and nature of the tetrapeptide atoms coordinated by the metal atom due to their different protonation. The conformational capabilities of the free tetrapeptide ligand and the degree of stability of the resulting types of complexes were not determined in [3]. Therefore, the purpose of this study was to study in detail, using the method of molecular mechanics, the spatial structure of the tetrapeptide Ala-Ala-Asp-Ala as a free ligand in the absence of an ion, and then in the presence of an ion - a divalent cation - to establish chelation centers and the structure of the resulting stable complexes.

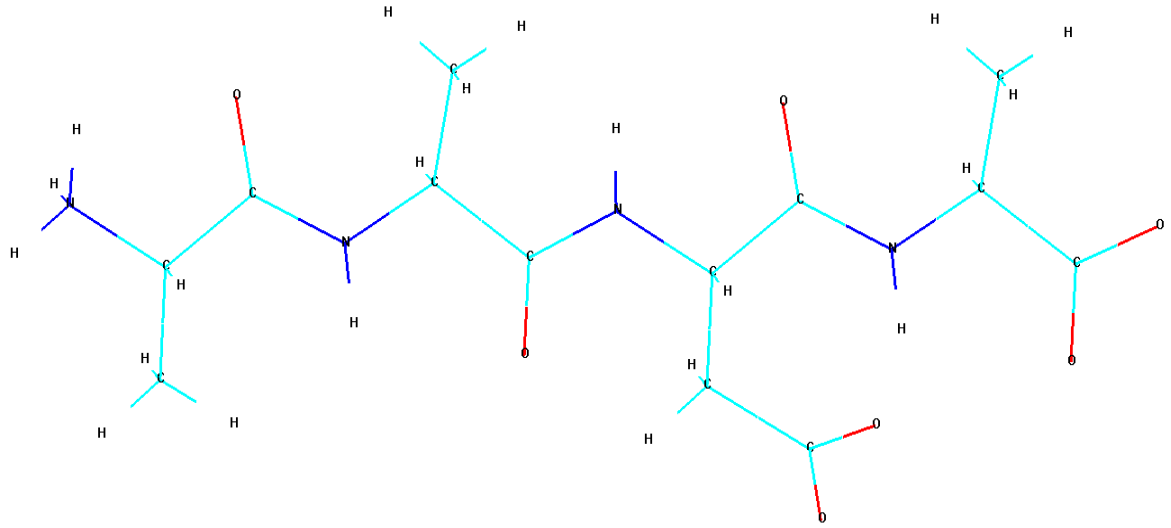

Figure. 1. The atom model of tetrapeptide segment H-Ala-Ala-Asp-Ala-OH.

METHOD

The study of the spatial structure and mechanism of ion binding by the tetrapeptide segment Ala-Ala-Asp-Ala was carried out by the method of molecular mechanics. Study of the conformational capabilities of the Ala-Ala-Asp-Ala tetrapeptide in the free state, i.e., in the absence of an ion, was carried out on the basis of the known low-energy conformational states of the individual monopeptides that make up this tetrapeptide. The conformational energy is considered the sum of independent contributions of nonbonded E_{nb}, electrostatics E_{el}, torsional interactions E_{tor} and hydrogen bonding E_{hb} energies. The first term is described by the Lennard-Jones potential with the parameters proposed by Scott and Scheraga [5-7]. The electrostatic energy is calculated in a monopole approximation, with atom centered charges obtained by Momany et al [8]. The dielectric constant is assumed to equal ten [5]. Torsional potentials and barriers to rotation about bonds N-C^{α} (φ), C^{α}-C′ (ψ), C′-N (ω), and about side chain bonds C^{α}-C^{β} (χ) were as proposed by Scheraga [6]. The hydrogen bond energy calculated from the Morse potential [7] are supposed to be weakened with maximum energy of 1.5 kcal/mol. The term "backbone form" of a peptide chain concerns the sequence of residue forms determined by the low energy areas R (φ= –180° to 0°, ψ= –180° to 0°), B (φ= –180° to 0°, ψ= 0°–180°), L (φ = 0°–180°, ψ= 0°–180°), and P (φ = 0°–180°, ψ= –180° to 0°) on the Ramachandran plot based on φ–ψ dihedral angles of the backbone. To specify the positions of a side chain of amino acid residues (χ_i) the indexes 1,2,3 corresponding to χ= 60^0, 180^0, -60^0 are used, respectively. The combination of the backbone form of the residues in each amino acid sequence will specify the backbone form of the fragment. Bonding lengths and angles are those given Corey and Pouling. Above potentials with energy and geometry parameters are used in some investigations [5,6]. Conformational energy was calculated with a universal program [9,10] The conventions used for torsion angles are those of IUPAC-IUB Commission [11]. The calculation of the conformations of the molecule was carried out under the assumption of a rigid valence scheme, i.e. at fixed values of bond lengths and bond angles of standard amino acid residues.

RESULTS AND DISCUSSION

Conformations corresponding to the minimum energy were found by studying the dependence of the total conformational energy of tetrapeptide structures on the rotation of dihedral angles in space. The study of the spatial structure of the Ala-Ala-Asp-Ala tetrapeptide in the presence of a divalent cation was carried out using the proposed calculation model of the cation (X2+), to which nonvalent parameters of the aliphatic hydrogen atom were assigned due to the simplicity of its electronic structure [4]. And since the radius of calcium (0.99 Å) is smaller than the van der Waals radius of the hydrogen atom (1.2 Å), the region of repulsion of the Lennard-Jones potentials for this atom is less steep than for any other metal atom. As is known, in peptide molecules, the oxygen atoms of carboxylate and carbonyl groups through coordination bonds participate in the chelation of metal atoms. The emergence of a coordination bond is due to the transfer of an electron pair from a completely filled orbital of the ligand (donor) to the vacant orbital of the central atom (acceptor) and the formation of a common bonding molecular orbital. Consequently, the nature of the coordination bond does not differ from the nature of an ordinary polar covalent bond. Therefore, for the convenience of calculations, the divalent cation (X2+), which was assigned the non-valent parameters of the aliphatic hydrogen atom, was attached to one oxygen atom of the carboxylate group present in the tetrapeptide at a distance of 2.3 Å with a Cγ-O-X2+ bond angle equal to 125^0 covalent communication It is borrowed this specific covalent fixation model of the divalent X2+ cation from [4]. The use of such fixation of the divalent cation makes it possible to identify chelating agents on the Ala-Ala-Asp-Ala tetrapeptide. Conformational analysis of the Ala-Ala-Asp-Ala tetrapeptide in the free state was carried out on the basis of low-energy conformational states of the corresponding amino acid residues. Figure 1 shows the computational model of the tetrapeptide under study. As can be seen from the figure, the amino acid sequence of the tetrapeptide consists of three alanine residues (Ala) and one aspartic acid residue (Asp), the side chain of which contains a negatively charged carboxylate group COO-. There is another carboxylate group at the C-terminus of the tetrapeptide. The side chains of Ala residues contain one methyl group, the rotation of which is equally likely in three positions of the side chain (60^0,180^0, -60^0). İnitial approximations for the calculated structural variants were made from the values of the dihedral angles φ and ψ of the three low-energy regions B, R and L. In this case, the angle χ1 of the side chain of the Asp residue varied in all three positions 60^0, 180^0 and -60^0. The value of the second angle χ2 of the side chain of the Asp residue was taken invariably to be 90^0. A total of 102 structural variants of the Ala-Ala-Asp-Ala tetrapeptide were compiled and calculated.

Table 1. Energy parameters of the optimal conformations of the H-Ala-Ala-Asp-Ala-OH tetrapeptide in free state.

Conformations of tetrapeptide in absence of divalent cation model						
№	Shape	Backbone form	Energetical contribution (kcal/mol)			
			E_{nb}	E_{el}	E_{tor}	E_{rel}
1.	eee	BBBB	-5.9	3.2	1.6	-1.2
		LBBR	-6.1	4.7	1.6	0.1
		RLBR	-4.0	5.2	1.6	2.9
		LLBR	-6.0	1.8	1.6	-2.7
2.	eef	BBRR	-5.5	3.5	1.6	-0.4
		LBRR	-5.7	3.3	1.6	-0.8
		RLRR	-5.0	4.5	1.9	1.0
		LLRR	-5.1	-3.1	2.7	-5.4
3.	efe	BRBR	-5.9	2.6	1.6	-1.6
		LRBR	-7.2	4.2	2.4	-0.6
4.	eff	BRRR	-5.9	2.6	1.6	-1.6
		LRRR	-6.1	-0.8	2.2	-4.7
5.	fee	RBBR	-6.8	1.5	2.2	-3.1
		BLBR	-2.3	1.2	1.1	0.0
6.	fef	RBRR	-6.1	4.0	1.6	-0.5
		BLRR	-5.7	-2.6	2.4	-5.9
7.	ffe	RRBR	-8.3	0.7	3.4	-4.1
8.	fff	RRRR	-4.0	-4.8	1.3	-7.5

As calculations showed, the conformations of the fff shape, forming an α-helical structure, turned out to be energetically preferable. Table 4.1 shows the energy parameters of the optimal tetrapeptide conformations. The relative energy range of 0-3 kcal/mol included the optimal conformations of only two shapes fff and fee, out of eight possible for the tetrapeptide. The remaining conformations have relatively high relative energy. The lowest energy conformation of the tetrapeptide RRRR of the fff shape form quasi-cyclic structures due to the formation of hydrogen bonds between the atoms of the ionized N- and C-terminal groups of the tetrapeptide. The distance between the hydrogen and oxygen atoms in these hydrogen bonds is 1.9-2.2 Å. In α-helical conformations of a tetrapeptide, the main stabilizing energy contribution is made by electrostatic interactions. In the RRRR conformation, for example, the contribution of electrostatic interactions exceeds the contribution of nonvalent interactions by 1 kcal/mol. In other conformations, on the contrary, nonvalent interactions make a decisive contribution to the stabilization of structures. However, the presence of ionized groups in the primary structure of the tetrapeptide promotes the formation of stable specific contacts of an electrostatic nature between the oppositely charged N- and C- terminal groups and the carboxylate group of the Asp residue in all structures of the molecule.

At the second stage of this study, a conformational analysis of the Ala-Ala-Asp-Ala tetrapeptide was carried out in the presence of a model divalent cation. For this purpose, the X2+ ion was attached to one oxygen atom of the carboxylate group of the tetrapeptide at a distance of 2.3 Å with a Cγ-O-X2+ bond angle of 125^0. Since the tetrapeptide contains two carboxylate groups COO-, which can participate in the chelation of the divalent cation, the model The ion was attached, in one case, to one oxygen atom of the carboxylate group of the side chain of the Asp residue, and in the other case, to one oxygen atom of the C-terminal carboxylate group. For each case separately, as initial approximations, 14 low-energy

conformations of the free tetrapeptide, included in the relative energy range of 0-5 kcal/mol, with a specifically bound X2+ ion and with six different values of the Cγ-O-X2+ dihedral angle, orienting given ion. The resulting total dihedral angle of rotation around the Cγ-O bond was determined by the position of the X2+ cation. This dihedral angle was given the original values of 0^0, $\pm60^0$, $\pm120^0$ and 180^0. The calculation showed that the most stable complex structures are realized in the case of attachment of the model cation to the oxygen atom of the carboxylate group of the Asp residue than in the case of attachment of the ion to the oxygen atom of the C-terminal group. In both cases, however, the inclusion of the model ion in the structure of the optimal tetrapeptide conformations significantly increases their conformational stability.

Table 2. The distance between oxygen atoms of the carboxylate groups in optimal conformations of the tetrapeptide H-Ala-Ala-Asp-Ala-OH in free state.

Conformation	Shape	Distance between oxygen atoms of the carboxylate groups (Å)			
		O_3-O_6	O_4-O_6	O_3-O_7	O_4-O_7
$B_1B_1B_3B_1$	*eee*	7.6	7.3	7.4	6.5
$B_1B_1R_1R_1$	*eef*	8.0	6.7	8.6	7.8
$B_1R_1B_1B_1$	*efe*	7.7	7.4	6.2	6.0
$B_1R_1R_3R_1$	*eff*	5.0	5.3	6.6	6.7
$R_1B_1B_1B_1$	*fee*	5.5	6.0	7.4	7.4
$R_1B_1R_1R_1$	*fef*	6.5	5.8	6.7	5.3
$R_1R_1B_3B_1$	*ffe*	4.6	4.2	6.0	3.7
$R_1R_1R_3R_1$	*fff*	7.6	7.4	6.2	6.0

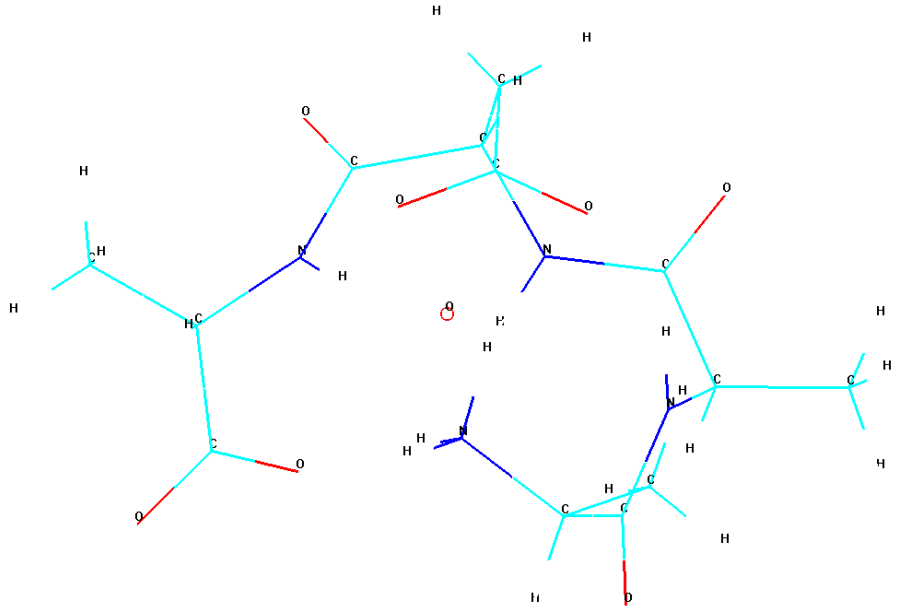

Figure 2. The calculated alpha-helical conformation in associated ion model in energetically preferable state of backbone structure RRBR.

Table 3 shows the energy and geometric parameters of the optimal tetrapeptide conformations in the presence of a divalent cation model. As can be seen from Table 3, the increase in conformational stability of optimal complex structures occurs mainly due to an increase in the contribution of electrostatic interactions.

The minimization results showed that the most suitable tetrapeptide conformations for ion chelation were those belonging to the four shapes eee, ffe, fee and efe with the corresponding main chain forms. It should be noted that the backbone forms of these conformations are characterized by the trans configuration of the Asp-X peptide bond, which appears to be a necessary structural requirement for the formation of the energetically favored complex structure. It was found that the tetrapeptide in the ion-bound state can form four types of complexes in the low-energy structures of the eee, efe, ffe and fee shapes. The energetically most favored tetrapeptide complex structure has the backbone form RRBR, which belongs to the ffe shape. Calculation of complex structures showed that ion chelation in low-energy conformations occurs with the highest coordination number (6), i.e. the interatomic distances of five oxygen atoms and one nitrogen atom in the environment of the ion can ensure its chelation. These are the four oxygen atoms of the two carboxylate groups and the oxygen and nitrogen atoms of the last peptide group of the peptide.

Table 3. Energy and geometric parameters of the optimal conformations of the H-Ala-Ala-Asp-Ala-OH tetrapeptide in presence of divalent cation model.

Conformations of tetrapeptide in absence of divalent cation model							
№	Shape	Backbone form	Coordinative number	Energy contribution (kcal/mol)			
				$E_{nb.}$	E_{el}	E_{tor}	E_{abs}
1.	eee	BBBB	6	0.9	-48.0	3.3	-43.8
		LBBR	6	-1.1	-47.9	3.9	-45.2
		RLBR	6	-1.4	-46.4	3.7	-44.2
		LLBR	6	-2.8	-46.1	4.3	-44.7
2.	eef	BBRR	4	-3.3	-34.3	3.8	-33.8
		LBRR	4	-3.6	-33.4	3.5	-33.5
		RLRR	4	-2.8	-33.2	3.8	-32.2
		LLRR	4	-3.8	-35.8	3.3	-36.4
3.	efe	BRBR	6	0.4	-49.3	3.2	-45.7
		LRBR	6	-1.0	-48.1	3.9	-45.2
4.	eff	BRRR	4	-1.6	-34.6	2.5	-33.7
		LRRR	4	-3.7	-33.1	3.3	-33.5
5.	fee	RBBR	6	0.3	-48.7	3.8	-44.6
		BLBR	6	0.9	-47.7	3.1	-43.7
6.	fef	RBRR	4	-3.2	-33.6	3.5	-33.4
		BLRR	4	-2.8	-33.5	3.8	-32.6
7.	ffe	RRBR	6	-1.3	-50.0	4.3	-47.0
8.	fff	RRRR	4	-2.6	-39.2	2.4	-39.5

Thus, it is can conclude that if for a tetrapeptide in the free state the energetically preferable conformation turned out to be a completely folded α-helical structure with the form of the main chain RRRR, then in the state bound to the ion, the unfolded conformation from the C-terminus with the form RRBR becomes energetically preferable. Hence, it can be assumed that under the influence of a divalent cation in the α-helical structure of a free tetrapeptide, the Asp-X peptide bond changes from the cis configuration to the trans configuration (RRRR→RRBR). Figure 2 shows a stereo drawing of the α-helical conformation of a tetrapeptide in the free state and in the ion-bound state with the RRRR main chain form.

CONCLUSION

The conformational analysis suggested the following mechanism of chelation of the divalent cation with the tetrapeptide Ala-Ala-Asp-Ala, according to which the complex structure is realized in its stable conformation with the trans-form of the peptide backbone of the Asp residue and where the X2+ ion is located inside the cavity formed by the main chain and is coordinated the oxygen atoms of the carboxylate group of the Asp residue and the C-terminal carboxylate group, as well as the oxygen and nitrogen atoms of the last peptide group.

Thus, based on experimental data and the results of theoretical conformational analysis, an energetically preferable model for the chelation of a divalent cation by the tetrapeptide segment Ala-Ala-Asp-Ala is proposed. A comparison of the obtained calculated structures of the tetrapeptide in the free and ion-bound states made it possible to determine the conformational changes induced by the divalent cation and specifically to establish an increase in the conformational stability of the spatial structures of the tetrapeptide segment during the formation of the complex.

ЛИТЕРАТУРА

1. Asso M., Granier C., Rietschoten J., Benlian D., *Calcium and praseodymium complexes in solution*, International Journal of Peptide and Protein Research ,Vol.26, No.1,p. 10-20, 1985
2. Asso M., Panossian R., *Copper and Nickel Interactions with Aspartate Containing Tetrapeptide*. Spectroscopy Letters, Vol.18, No.10, p. 837-842,1985
3. Decock-le R.B., Lebkiri A., Livera C. Pettit L.D. *A potentiometric and spectroscopic study of the interaction of Ala-Ala-Asp-Ala with Cu(II)* ,Inorg.Chim.Acta, Vol. 124 , No 4, p.19-22, 1986
4. Eastman M.A., Pedersen L.G., Hiskey R.G., Pique M., Koehler K.A.,Gottschalk K.E., Nemethy G., Scheraga H.A. *Conformation of the 18-23 loop region of bovine prothrombin in the absence and presence of a model Ca2+ ion. An energy minimization study.*, Int.J.Peptide Protein Res., Vol.27, p.530-553, 1986
5. Popov E.M. *Quantitative approach to conformations of proteins*, Int. J. Quant. Chem., Vol.16, pp. 707-737, 1979
6. Scheraga H.A. *Calculations of conformations of polypeptides* ,Adv. Phys. Org. Chem., Vol. 6, p.103-108,1968
7. Scheraga H.A. *Recent progress in the theoretical treatment of protein folding // Biopolymers.*, Vol. 22, p.1-14, 1983
8. Momany F.A., Mc.Guire R.F., Burgess A.W., Scheraga H.A. *Energy parameters in polypeptides : VII. Geometric parameters, partial atomic charges, nonbonded interaction for naturally occurring amino acid* , Phys. Chem., Vol. 79, p. 2361-2381, 1975
9. Maksumov I.S., Ismailova L.I., Godjaev N.M., *The program for semiempirical calculation of conformations of the molecular complexes*, J. Sruct. Khim, Vol 24, p. 147-148, 1983
10. Hermans J.Jr., Ferro D., Representation of a protein molecule as a tree and application to modular computer programs which calculate and modify atomic coordinates, Biopolymers, Vol.10, p.1121-1138,1971
11. IUPAC-IUB *Commision on Biochemical Nomenclature Abbreviations and symbols for description of conformation of polypeptide chains*, Pure Appl. Chem., Vol. 40, p. 291-308,1974

JOURNAL OF BAKU ENGINEERING UNIVERSITY - PHYSICS
2023. Volume 7, Number 2 *Pages 57-78*

PASC:61.46.-w
UOT: 359.216

PROPERTIES, SYNTHESIS METHODS, AND APPLICATION OF SEMICONDUCTOR CHALCOGENIDES CDS AND ZNS NANOPARTICLES

ZEYNAB ADDAYEVA RAMAZAN [A*], MAHAMMAD BAGHIR BAGHIROV[A]

[a] Nano Research Laboratory, Baku State University,
23 Academic Zahid Khalilov Street, Baku AZ1148
Corresponding author: Zeynab Addayeva Ramazan
zeynabramazan5399@gmail.com

ABSTRACT

This article provides a comprehensive exploration of CdS and ZnS, the prominent members of semiconductor chalcogenides resulting from the combination of group II and VI elements. The semiconductor chalcogenides have gained significant attention in recent times, owing to their distinctive electrical and optical properties. The study delves into the intrinsic characteristics of CdS and ZnS, elucidating their diverse properties and parameters, all of which are contingent upon the methods employed for their acquisition. Various production methods are scrutinized, shedding light on the impact of these techniques on the final properties of the semiconductor chalcogenides. Additionally, the article highlights the broad spectrum of applications these materials find in contemporary technological advancements. By synthesizing information on properties, production methods, and applications, this article aims to contribute to the understanding and utilization of CdS and ZnS semiconductor chalcogenides in diverse scientific and industrial domains.

Keywords: semiconductor chalcogenides, CdS, ZnS, sulfidization, band gap, solar cell, photocatalyst, sensor.

СВОЙСТВА, МЕТОДЫ СИНТЕЗА И ОБЛАСТИ ПРИМЕНЕНИЯ НАНОЧАСТИЦ ПОЛУПРОВОДНИКОВЫХ ХАЛЬКОГЕНИДОВ НА ОСНОВЕ CDS И ZNS

РЕЗЮМЕ

В данной статье представлены исследования полупроводниковых галогенидов CdS и ZnS, образующихся как сочетания II и VI групп элементов. В последнее время полупроводниковые галогениды привлекли к себе значительное внимание благодаря своим специфическим электрическим и оптическим свойствам. Исследование характеристик CdS и ZnS показало, что эти свойства зависят от методов их получения. Рассматриваются различные методы получения, которые влияют на свойства полупроводниковых галогенидов. Обобщая информацию о свойствах, методах производства и применении, эта статья может внести вклад в понимание и применение полупроводниковых галогенидов CdS и ZnS в различных научных и промышленных областях.

Ключевые слова: полупроводниковые галогениды, CdS, ZnS, сульфидизация, запрещенная зона, солнечный элемент, фотокатализатор, сенсор

YARIMKEÇİRİCİ XALKOGENİDLƏR CDS VƏ ZNS NANOZƏRRƏCİKLƏRİNİN XASSƏLƏRİ, SİNTEZ ÜSULLARI VƏ TƏTBİQ SAHƏLƏRİ

XÜLASƏ

Bu məqalədə II və VI qrup elementlərinin birləşməsindən yaranan yarımkeçirici halogenidlərin mühüm nümayəndələri olan CdS və ZnS tədqiqi təqdim edilmişdir. Yarımkeçirici halogenidlər elektrik və optik xassələrinə görə son dövrlərdə böyük diqqət qazanmışdır. CdS və ZnS halogenidlərin xüsusiyyətlərinin tədqiqi göstərdi ki, bu xassələr onların hazırlanma üsullarından asılıdır. Müxtəlif hazırlanma üsulları təqdim edilmiş və bu üsulların yarımkeçirici halogenidlərin xassələrinə təsiri öyrənilmişdir.. Xassələri, hazırlanma üsulları və tətbiqləri haqqında məlumatları analiz edərək, bu məqalə müxtəlif elm və sənaye sahələrində CdS və ZnS yarımkeçirici halogenidlərin və tətbiqinə töhfə vermək məqsədi daşıyır.

Açar sözlər: yarımkeçirici halogenidlər, CdS, ZnS, sulfidləşmə, qadağan olunmuş zona, günəş elementi, fotokatalizator, sensor.

Manuscript receved 06.05.2023

1. Introduction

In recent times, the widespread use of semiconductor chalcogenides in industry and technology has had a serious impact on their research speed. Semiconductor chalcogenides are II-VI materials formed by the combination of group II elements such as Cd, Zn, and Hg and group VI elements such as S, Se, or Te [1]. Most of these materials have a direct band gap. In materials with a direct band gap, the transition of an electron from the valence zone to the conduction zone occurs at the same pulse as in materials with an indirect band gap, and electron-hole recombination in them causes photoemission [2]. This property ensures their use in optoelectronic devices such as lasers and photodiodes. Especially microelectronics, alternative energy sources, sensors, nanomedicine, etc. CdS and ZnS are considered important elements in these areas for the development of optical, electrical, thermal, and chemical properties [3].

One of the main factors affecting the properties of this group of materials is its size and structure. In recent years, special attention has been paid to semiconductor materials with particle sizes in the nanometer range. This is due to the quantum size effect and the increase in the surface-to-volume ratio when moving into the nanoscale range. These changes strongly affect the optical properties of materials as well as other properties [4]. When moving to the nanoscale in materials in each direction, different properties of the material appear. So, when the size of the material in any direction is proportional to the de-Broyle wavelength, there are limitations in the movement of charge carriers in that direction and quant size effects subject to the laws of quantum physics are observed [5]. This article looks at 0D particles (quantum dots). The most impressive property changes in QDs with particle size smaller than ~30 nm are sharp differences in optical absorption, excitation energies, and recombination of electron-hole pairs [6]. The use of these properties requires strict control of their synthesis and structure, as their intrinsic properties depend on size, shape, defects, and impurities, and are determined by factors such as crystal structure. Due to the high surface-to-volume ratio of QDs, surface-bound electronic quantum states (called surface states) have a significant effect on the optical properties of QDs [7]. For example, about 15% of the atoms in a 5 nm CdS QDs are on the surface. Such a high surface-to-volume ratio can allow the transfer rate of photogenerated charge carriers to increase or decrease due to the high density of surface sites. The surface states of QDs (the number of electronic states present in each energy level) can affect the optical absorption, quantum efficiency, luminescence intensity, and spectrum. In general, surface states arise from loose bonds on the reformed surface and can also be affected by deficit centers [8]. The energy of these surface states is generally equal to the size of the band gap of QDs. Therefore, they can trap charge carriers and cause radiative and/or non-radiative recombination of electron-hole pairs. As a result, the surface states have a significant effect on the optical properties of QDs. The most unique feature of QDs is quantum confinement, which changes the density of states near the band edges [10]. Thus, quantum confinement modifies the density of states near the band edges and leads to discrete energy levels rather than discontinuous bands. This modification greatly affects the electronic and optical properties of the material [11,12].

Let's focus on the properties, production methods, and applications of the two main components of this group, CdS and ZnS.

1.2 CdS nanoparticles and their properties

CdS has three types of crystal structures, namely wurtzite (hexagonal), zinc blende (cubic), and high-pressure rock-salt phase. Among these, hexagonal wurtzite has been intensively studied because it is the most stable of the three phases and can be easily synthesized [13, 14]. The hexagonal phase was observed in both bulk and nanocrystalline CdS, while cubic and rock salt phases were observed only in nanocrystalline CdS. The structure of nanocrystalline materials plays an important role in determining electronic properties. The same material can crystallize in different structures during size reduction depending on the reaction conditions [15]. The internal energy difference between these two phases of CdS is very small, so the controlled synthesis of CdS nanocrystals in only one phase at a time is difficult to achieve. Some studies have found that sphalerite CdS nanoparticles exist in smaller sizes and wurtzite structure is formed by particle growth. Other researchers have shown the possibility of structural transitions from the cubic phase to the hexagonal phase when CdS nanoparticles are thermally treated between 300 and 400°C [16-18]. Others, based on the size-dependent total Gibb's free energy, have described the phase transition to the cubic phase as a metastable phase with no effect due to size reduction [19,20]. However, some different researchers have shown that the hexagonal-cubic phase transition is size-dependent with a critical transformation size ranging from 4–15 nm.

CdS with bulk structure has a band gap of 2.42 eV and a melting point of 1600 °C. An increase in the value of the band gap with decreasing particle size is a property studied by optical absorption spectroscopy [21]. The proximity of this value to visible light wavelengths gives it a colored appearance [22]. So, depending on the size, the color of nanoparticles also changes. Smaller sizes emit a lower wavelength light beam while relatively larger sizes emit a higher wavelength light beam as the particle radius decreases, the onset of absorption shifts to higher energy. In some studies, 2 nm nanoparticles have a band gap of 3.57 eV, and 2.5 nm CdS crystallites melt at temperatures as low as 400 °C [23]. In particular, CdS has been the focus of recent attention due to its large band gap that allows light emission between blue and red wavelengths. Photocells made of CdS crystals are extremely sensitive in the entire spectrum from infrared to ultraviolet, X-rays, gamma rays, and corpuscular rays [24,25].

1.3 ZnS nanoparticles and their properties

Zinc sulfide (ZnS) is an important non-toxic, chemically stable group II-VI semiconductor with luminescent properties. ZnS nanoparticles exhibit properties different from their bulk structure as their size moves to the nanoscale. For example, in the optical absorption spectrum, nanoparticles are blue-shifted at 320 nm due to quantum size effects relative to bulk ZnS (absorption frequency is blue-shifted to correspond to 320 nm) [26]. Also, the dielectric constant of ZnS, which has a low dielectric constant at high frequencies, increases when the dimensions fall into the nanoscale. Zinc sulfide (ZnS) is an important anti-toxic and has a high refractive index (12.27) [27]. Found mainly in nature as two minerals (wurtzite and sphalerite or zinc blende), the more stable and allotropic form of ZnS known as zinc blende or sphalerite is the cubic form (β-ZnS). wurtzite (α-ZnS) is hexagonal in shape. In both cubic and hexagonal structures, the Zn and S atoms are tetrahedrally bonded, where the only difference is in the stacking order of the atomic layers [28,29]. Nevertheless, the relative stability of the two phases changes with decreasing particle size.

ZnS with a bulk structure exists in nature mainly in the form of zinc alloy (cube), unlike CdS. The cubic phase is a stable low-temperature phase, while the wurtzite phase is a high-temperature polymorph and can form in bulk ZnS at temperatures higher than 1020 °C. Also, at high temperatures, the structure of ZnS, which has a cubic structure, can be transformed into a hexagonal wurtzite form [30]. The conducted studies have shown that this transformation occurs at 1013 or 1031 °C, depending on the activity of sulfur. This transformation is a very important issue in the application of ZnS. So wurtzite type has better properties than sphalerite [31-33]. Thus, as a result of theoretical studies, it was determined that the average surface energy of three-dimensional nanoparticles is greater for the sphalerite phase than for the wurtzite phase [34,35]. Another experimental study shows that zinc sulfide (ZnS) mainly has E_g in the range of 3.54 eV and 3.80 eV at 300 K, respectively, and the band gap structure differs from one another in its allotropic transitions. The conducted research shows that the E_g of hexagonal wurtzite is 3.77 eV and the E_g of cubic sphalerite is 3.72 eV. Generally speaking, we can control its electrical properties as well as some other properties by performing an allotropic transformation of ZnS, which has a flat band gap of 3.5-3.7 eV in cubic form and 3.7-3.8 eV in the hexagonal form [36].

Since the absorption limit of ZnS is shorter than 340 nm, it only allows the absorption of high-energy light. This absorption limit can be shifted to higher wavelengths, often called red-shifting, by adding a suitable additive. If semiconductors are doped with transition metals such as Ni, Fe, Mn, and Co, improved properties can be obtained due to the spin-spin interaction. The main optical property of ZnS is its luminescent character. This is explained by its direct band gap and photon emission during transition [37,38].

2. Materials and methods

2.1. Synthesis of CdS and ZnS NPs by chemical colloidal method.

It is based on the bottom-up synthesis of nanoparticles through the chemical colloidal method in an environment consisting of homogeneously distributed particles in a liquid. Even when the distance between particles in the medium is small, they attract each other with van der Waals forces [39].

2.1.1 Synthesis of CdS NP chemical colloidal method

CdS nanoparticles can be synthesized based on various reactions using different precursors through the chemical colloidal method. This article shows some of them.

I. In this method, which is one of the chemical extraction methods, the reagents are used without any additional processing. The reagents used are $CdCl_2$, Na_2S, H_2O and ethanol. First, 0.1 mol of CdC_{l2} was added to 25 ml of water to get a solution. Then, 0.1 mol of Na_2S was added to the obtained solution and heated in the range of 20-80 ^{o}C.

$CdCl_2+Na_2S$---->CdS+ 2NaCl (1)

The obtained solution was washed 5 times with ethanol and dried at 50 ^{o}C for 30 minutes to obtain CdS particles. Let's note that the reaction was carried out at different rates in the range of 20-80 ^{o}C and comparing the sizes of the nanoparticles, it was found that the size of the nanoparticles increases with the temperature. Thus, from the reaction conducted at 20 ^{o}C, 4.5 nm, 5.2 nm at 40 ^{o}C, 6.6 nm at 60^{o}C, and 7nm particles at 80^{o}C were obtained. In this method, the reagents were used without any further processing. This reaction is carried

out in aqueous medium, 250 ml of water, 1.1 g of $Cd(NO_3)_2$* $4H_2O$, 0.2M HNO_3, 0.57g of C_2H_5 NS (thioacetamide-TA)

A solution is prepared by adding 0.2 M HNO_3 to 250 ml of water. 1.1 g of $Cd(NO_3)_2$ *$4H_2O$ is added to the obtained solution. C_2H_5NS is added to the obtained mixture and immersed in a water bath at 80^o C for 30 minutes. After half an hour, the solution was left to dry at room temperature [40-42].

II. Another example of a colloidal synthesis method, which is a chemical extraction method, is the preparation of CdS nanoparticles using starch as a stabilizing agent in an aqueous medium. $Cd(CH_3COO)_2$* $2H_2O$, Na_2S, and starch are used in this method, which allows obtaining particles with a size of 2.43 nm. 50ml of 0.05M $Cd(CH_3COO)_2$* $2H_2O$+ is mixed with 4ml of 1% starch. 50ml of 0.05M Na_2S was added drop by drop to the obtained solution, stirred for 4 hours at room temperature, and allowed to settle and evaporate. Then the obtained product is washed with distilled water, filtered, and dried in a 90 °C oven [43].

III. This process with the presence of sodium dodesulfate, thiourea (C_2H_5NS), and $CdCl_2$ was carried out at room temperature. Sodium dodesulfate is stirred for 5 minutes and 0.25 M $CdCl_2$ is added dropwise and mixed. After the addition is complete, the solution is stirred for another 10 minutes and finally 0.25M C_2H_5 NS solution is added dropwise and stirred after 30 minutes. In the conducted reaction, the amount of sodium dodesulfate was changed (0.0025M, 0.005M, or 0.01M) and its pH and electrical conductivity were measured. It was determined that increasing the amount of SDS did not affect the pH of the system containing CdS nanoparticles, but the electrical conductivity of the nanoparticles increased with the increase in the amount of SDS [44].

IV. Cadmium oxide (CdO, SCR, 99.9%), sulfur (S, SCR, 99.5%), 1-octadecene (ODE, Fisher, 90%), oleic acid (OA, SCR, 90%) and acetone and chloroform (SCR) was used directly without further treatment. Typically, 1 mmol of CdO, 4.5 mmol of OA, and ODE (5 mL total) are mixed and heated to 150°C under nitrogen for 1 h with vigorous stirring to prepare a clear, yellow, cadmium-precursor solution. Meanwhile, a stock solution of sulfur was prepared by dissolving 1 mmol of sulfur powder in ODE (total 5 mL) at 150°C for 1.5 h under magnetic stirring. The microfluidic reactor includes a precursor transfer system, a convective micromixer, and a polytetrafluoroethylene capillary (length = 50 cm). Equal volume solutions of Cd and S precursors were delivered with a syringe injector at the same flow rate, and the precursors were combined and mixed in a magnetic micromixer. Then, the mixture of precursors was placed in a heated PTFE capillary where nucleation and growth of NCs occurred at a constant reaction temperature of 220 °C. A thermally stable oil bath was used as the heat source and the precursor flow rate was set at 4.47 mL/h to achieve a residence time of 68 s. During the optimization process for OA concentration, different amounts of OA were replaced by ODE, keeping the solution volume constant. The samples were collected and diluted with chloroform for further characterization of their spectra. The whole process takes place in the air [45,46].

2.1.2 Synthesis of ZnS NPs by chemical colloidal method

In recent times, the chemical colloidal method, which is considered to be an efficient production method for obtaining ZnS, is widely used as a one-step reaction. The reactions

selected for these processes are designed to be simple, rapid, and obtain high quantities of the desired products. Let's get acquainted with some of them [47,48].

I. The preparation of ZnS involves the use of chemical reagents, especially $ZnCl_2$ and $ZnSO_4$, as well as a source of sulfur derived from Na_2S. sulfate is included as a source of sulfur due to its ability to undergo hydrolysis and form S^{2-}ions. The reaction mixture also includes organic solvents such as methanol, ethanol, and ethylene glycol. A small amount of acid or base is added to catalyze the reaction. Organic stabilizers are used to provide precise control of physical properties such as surface area, pore size, and pore volume. These stabilizers play an important role in shaping the properties of ZnS particles. Although the one-pot synthesis process achieves high-purity ZnS particles, it is limited by the necessity of high temperatures. To solve this, the subsequent calcination process-thermal treatment process is carried out. This step serves to remove organic stabilizers and solvent media, increasing the purity of the ZnS product. The chemical transformation involves the binding of S^{2-} ions with Zn^{2+}, which leads to the formation of ZnS as a precipitate. This approach, characterized by its simplicity, efficient reactions, and control over physical properties, proves to be a convenient and efficient method for the synthesis of ZnS, although it is initially dependent on high temperatures. A subsequent calcination step ensures the removal of organic components, resulting in a refined and highly pure ZnS product [49-51].

$$S^{-2}O_3^{2-}+H_2O\text{-----}SO_4^{2-}+H_2S \quad (2)$$

$$H_2S + Zn^{2+}\text{-------}ZnS + 2H^+ \quad (3)$$

II. One of the ZnS production reactions carried out in one pot is the synthesis process with the presence of organic surfactants. The lower toxicity of ZnS nanoparticles obtained during this process than ZnO ensures its use in biology and medicine. In the synthesis, zinc acetate and TAA were dissolved in Fc-loaded DDAB vesicle solution. The final concentration of zinc acetate in the solution was 22.7 mM, and the molar ratio of $Zn(Ac)_2$/TAA/DDAB was 16:16:1. The solution was stirred until complete dissolution and then the resulting solution was heated to 80C in a water bath. The reaction was kept on a magnetic stirrer for 6 hours and the color of the solution turned milky white. Finally, the solution was cooled to room temperature. for the drying process, the products were collected by centrifugation, washed several times with ultrapure water to remove impurities, and then vacuum dried. Some studies have studied the control of toxicity and properties of ZnS by changing the solvents [52].

III. Zinc sulfide nanoparticles (ZnS NPs) were synthesized using zinc acetate ($C_4H_6O_4Zn.2H_2O$) as a metal precursor. Various concentrations of sodium dodecyl sulfate (SDS) were used in the process - specifically, 0.001M, 0.002M, or 0.004 M. The SDS solution was stirred for 5 min to ensure uniform dispersion. Then, a solution containing zinc acetate ($Zn(CH_3COO)_2$) at a concentration of 0.05 M was added dropwise to the SDS solution and stirred for an additional 10 min. After adding the zinc acetate solution, thioacetamide at a concentration of 0.05 M was added dropwise to the reaction solution. The entire synthesis process was carried out under continuous stirring, allowing the reaction to proceed for an additional 30 min. In the synthesis, the effect of different concentrations of SDS on the electrical conductivity of nanoparticles and the pH of the solution containing nanoparticles was investigated, and it was found that, unlike CdS, it had no significant effect [44].

2.2 Synthesis of CdS and ZnS NPs by sol-gel method

In recent times, one of the methods used in obtaining solid phases is the sol-gel method. In this method, which is a multi-step process, Zol is prepared first. A gel is formed as a result of hydrolysis and condensation processes in the prepared sol-colloidal solution. After the gel is formed, the washing and drying process is carried out. The dimensions and properties of the obtained products are controlled by controlling the stabilizers and the process time. In particular, great attention should be paid to the gel formation time to obtain small-sized particles. Metal-based alkoxide materials are mainly used as the main chemical reagents that are part of the sol-gel formation [53].

2.2.1 Synthesis of CdS NPs by sol-gel method

Cadmium acetate ($Cd(CH_3COO)_2.2H_2O$), diaminobenzene, thioacetamide (CH_3CSNH_2), and deionized water acted as the main reagents in the synthesis process. A low reaction temperature chemical extraction technique was used to synthesize CdS nanoparticles. First, 2.66 grams (10 mmol) of cadmium acetate hydrate and 2.16 grams (20 mmol) of diaminobenzene were dissolved in deionized water and stirred on a magnetic stirrer for 4 h. Then, 1.52 grams (20 mmol) of thioacetamide was added to the solution, and the mixture was stirred with a magnetic stirrer for an additional 4 hours. During the reaction, the color of the solution turned light yellow, indicating the formation of CdS nanoparticles, and a homogeneous solution was obtained. After stirring with a magnetic stirrer for 4 h, the resulting precipitate was separated by centrifugation at 3000 rpm. The obtained precipitate was washed several times with deionized water and then subjected to a drying time of 2 h. To prepare CdS, deionized water was boiled, continuously sprayed in an ice bath, and then cooled to room temperature. This rigorous purification process ensured the quality of the solvent used in CdS synthesis. The average diameter of the synthesized CdS nanoparticles was determined to be 40 nm [54].

2.2.2 Synthesis of ZnS NPs by sol-gel method

Deionized water was used as a solvent in the experiment. Zinc acetate $Zn(CH_3COO)_2{\cdot}2H_2O$ (2.194 g) and $Na_2S{\cdot}9H_2O$ (4.8038 g) were dissolved separately in deionized water. The two solutions were then mixed and stirred at room temperature for 15 min. The mixture was heated to 80°C on a magnetic stirrer while maintaining a constant stirring speed. Within 10 minutes, a gel was formed, indicating the initial stage of the reaction. The resulting viscous gel was dried in an oven at 60°C for 10 hours to remove excess water. The dried powder was then subjected to further thermal treatment at 300°C, 400°C, 500°C and 600°C, respectively, to obtain the final product. The size of the obtained ZnS particles with a cubic structure varies between 15-24 nm [55,56].

2.3 Synthesis of CdS and ZnS NPs by gas-liquid phase method.

Obtaining nanoparticles in a gas-liquid environment with the presence of a vacuum and an inert gas environment causes them to be cleaner than other chemical methods. It is possible to control the particle sizes and their parameters by controlling the pressure of the vacuum and the inert gas entering, as well as the temperature [57,58].

2.3.1 Synthesis of CdS NPs by gas-liquid phase method.

The reaction is carried out using a suitable Schlenk line apparatus under a nitrogen atmosphere. The device is provided with an inert gas environment (nitrogen) and vacuum. The reaction flask is heated through a hot oil bath to obtain the temperature. A description of the synthesis process is shown in Figure 1.

1 mM cadmium nitrate is poured into a three-necked flask and heated to 140^0C with 15 ml of oleylamine ($C_{18}H_{37}N$) added to form the Cd-oleylamine complex. The transparent color of the solution confirms the formation of a metal complex. Then the temperature is raised to 160^0C and the reaction temperature for this reaction is 160^0C. After reaching the reaction temperature, H_2S gas is introduced into the metal complex solution. H_2S gas is obtained from the thermal treatment reaction of FeS with HCl. When H_2S gas is introduced into the flask, the color of the solution starts to change from colorless to light yellow. Short-core detonation occurs through supersaturation of the precursor to limit the particle size. After 10 minutes of H_2S, the reaction is stopped by removing the flask from the heating mantle. After that, the reaction mixture is cooled to 100 ^{0}C and the necessary amount of chloroform is added to remove the unreacted oleylamine. After the addition of ethanol, the yellow product is precipitated and centrifuged 5 times at 6000 rpm for 5 minutes each time. The purified and centrifuged yellow powder was dried under a vacuum at 70^0C. The same reaction is carried out at 200^0C and 240^0C, respectively, and to measure the use of the samples in solar panels, their photovoltaic parameters were compared, and it was revealed that the samples taken at 200 and 240 degrees had higher charge carrying capacity [59,60].

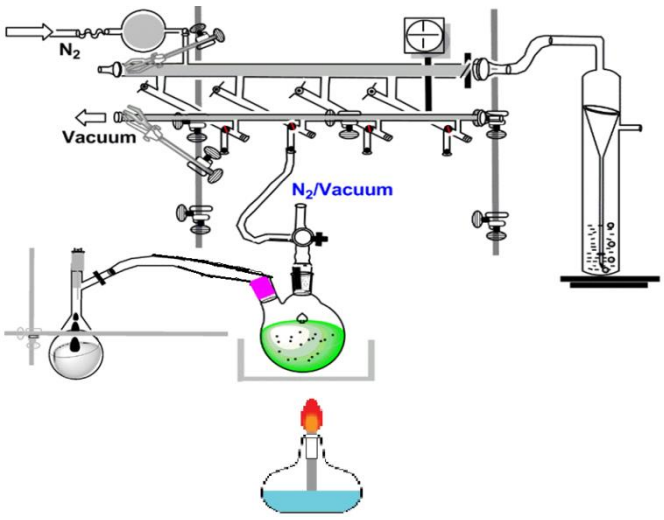

Figure 1. Description of the synthesis process of CdS NPs.

2.3.2 Synthesis of ZnS NPs by gas-liquid phase method

ZnO plates are used as a source of Zn in the production of ZnS in the liquid-vapor phase. ZnO is sulphided using supercritical fluids H_2S and H_2S/H_2O under appropriate temperature and pressure in a special facility. The main part of the device has an internal diameter of 1.7 cm; and is a stainless steel tubular reactor with volume V = 57 cm^3. The reactor includes high-pressure vessels for introducing H_2S (V = 49 cm^3) and H_2O (V = 420 cm^3

), a part for cooling precursors with liquid nitrogen, and a vessel for collecting products (V = 3.2 dm^3).

The main parts of the installation of the 12Cr18Ni10Ti reactor: are a nest for products cooled by liquid nitrogen (V = 35 cm^3); a first-stage vacuum pump; mass spectrometer vacuum unit. The experimental setup is equipped with a computer-based device for pressure and temperature control. The reactor is heated by external resistance heaters and the temperature is controlled by software. Temperature is measured with chrome-alumni thermocouples with an accuracy of ±1°C. The pressure is measured by membrane tension sensors with an accuracy of 0.25% of the measured value [61].

The object of study was zinc plates made of high-purity zinc, high-purity hydrogen sulfide, and distilled water. It was determined by mass spectrometric analysis of hydrogen sulfide that it contains 0.9908 and 0.1315 mol.% of CS (carbon mono sulfide) and CS_2 (carbon di sulfide) respectively. Saturated hydrogen sulfide vapor in a standard aluminum balloon (V = 1.5 dm^3) was recorded in a pre-vacuum vessel cooled with liquid nitrogen. After cooling, the pressure of H2S in the vessel was ≈35 MPa at room temperature, which provided the operating pressure in the reactor. Studies show that reaction equipment is sulphided by supercritical fluid. Therefore, it can be concluded that the structural elements of the reactor must be sulphided/oxidized with H_2S/H_2O supercritical fluid several hours before the experiment. This allows us to minimize the error when determining the amount of hydrogen formed during the interaction of zinc plates with H_2S and H_2O molecules.

A zinc plate of weight m, thickness h, and geometric surface S is placed along the axis of the reactor in a horizontal position. In this study, to investigate the changes in the parameters of ZnS as the dimensions change, synthesis was carried out in pots of different sizes. All procedures, including mechanical cleaning of zinc oxides from the surface of the plates, their weighing, and loading into the reactor, were carried out under an N_2 atmosphere. All volumes were evacuated with a first-stage vacuum pump before H_2S and H_2O were injected into the reactor. Sulphidation/oxidation of zinc was determined by the weight gain of the plate. The mass was calculated based on the amount of hydrogen produced as a result of the reaction. The process was carried out at a temperature of 400°C. In the conducted research, the sulfidation process was carried out by changing the heating time and pressure, and also with and without water. ZnS obtained in the form of plates leads to obtaining nanoparticles in the next step with a top-down approach using different methods [62,63].

2.4 Synthesis of CdS and ZnS NPs by electrochemical deposition method

During the synthesis by the electrochemical precipitation method, the phenomenon of accumulation of electrolyte ions on the electrodes occurs with the action of electric current. The properties of the collected substances depend on the applied voltage, the type of electrolyte, and also the degree of purity of the substances from which the electrodes are made. Thus, an electrolyte solution consisting mainly of metal salts or precursors of the desired nanoparticles is prepared. The choice of electrolyte determines the type of nanoparticles to be synthesized. The potential difference between the anode and the cathode leads to the reduction of electrolytes, and as a reduction product, nanoparticles of the precursors settle on the electrodes. So, first, as metal ions are reduced, nucleation centers are formed on the surface of the electrode. These cores are then transformed into nanoparticles by continuous reduction of metal ions [64].

2.4.1 Synthesis of CdS NPs by electrochemical deposition method

The solution used for electrochemical deposition consists of cadmium fluoride (CdF_2) and sodium fluoride (NaF) dissolved in water. The CdF2 concentration is 1.0 millimolar (mM) and the NaF concentration is 0.1 molar (M). The pH value of the solution is about 6.2. Larger cadmium oxide nanocrystals, especially those with radii greater than 30 angstroms, undergo spontaneous oxidation in solution when the circuit is open. After the oxidation process, the graphite sheet is removed from the electrolysis unit, washed with ultrapure water, and placed in a quartz tube. H_2S gas flows for 10 minutes over the graphite layer subjected to thermal treatment at a temperature of 300^0C. At this time, the transformation of cadmium oxide (CdO) nanocrystals into cadmium sulfide (CdS) nanocrystals occurs. The obtained products are sulfide-coated CdS nanoparticles. The 17-50A sulfur shell (30A) of the purchased products prevents CdS from agglomerating and helps to maintain its effective properties [65-67].

2.4.2 Synthesis of ZnS NPs by electrochemical deposition method

Electrolyte solutions were prepared using sodium sulfide and deionized water. Mass electrosynthesis was carried out by potentiostatic electrolysis in a single-cell unit using a programmable power supply system. The working electrode consisted of a zinc plate with a geometric surface area of 2 cm^2, and the cathode consisted of a platinum mesh electrode.

Electrochemical synthesis two-electrode electrolysis system (zinc electrode acts as anode and platinum as cathode). conducted at room temperature (22 ±1 ºC) in a Pyrex container (V= 400 cm^3). Before electrolysis, platinum and zinc electrodes were cleaned with detergent and electrochemically polished. During all experiments, electrode types and sizes, electrolysis time, and temperature were determined. The synthesis was carried out for 30 min at different applied constant potentials. To collect the product, the solution was filtered and the resulting precipitate was washed three times with ethanol and then dried at 80 ºC for 3 h.

The results of this study show that the preparation of zinc sulfide nanoparticles by electrolysis is simple, clean, and relatively fast. Furthermore, electrodeposition is a better option to control the product morphology by changing the electrolysis variables [68].

2.5 Synthesis of CdS and ZnS NPs by biological method

Green synthesis of nanoparticles is an environmentally friendly and sustainable method used to produce nanoparticles using natural sources such as plants, bacteria, fungi, or other biological materials, as well as environmentally friendly chemicals. In this context, the term "green" emphasizes the use of more environmentally friendly methods compared to traditional nanoparticle synthesis approaches, which often involve the use of toxic chemicals and high-energy processes [70]. The main aspects of the green synthesis of nanoparticles are as follows:

1. Biological Resources:

a) Plant extracts: Bioactive compounds present in various parts of plants (leaves, stems, roots) can serve as both reducing and stabilizing agents in the synthesis of nanoparticles.

b) Microorganisms: Certain bacteria, fungi, and algae are used for their ability to produce enzymes or metabolites that facilitate the reduction of metal ions to form nanoparticles.

c) Other Biological Sources: Natural polymers such as chitosan or proteins can also be used in the synthesis of nanoparticles.

2. Reducing precursors: Bioactive compounds in the selected biological resource act as reducing agents to convert metal ions from metal precursors (e.g., metal salts) into metal nanoparticles.

3. Stabilizers: The same bioactive compounds also act as stabilizers that prevent the agglomeration of nanoparticles and stabilize the resulting nanomaterial.

4. Easy reaction conditions: Green synthesis methods often occur under mild reaction conditions, avoiding the need for high temperatures, pressures, or toxic chemicals [71,72].

2.5.1 Synthesis of CdS NPs by biological method

The tea plant was used in the biological synthesis of CdS nanoparticles. A 0.1M $Na_2S.H_2O$ solution was prepared in a clear water solution, then the tea solution was slowly added to this solution with vigorous stirring, and a black tea-colored solution was formed. Then the prepared 0.1M $CdSO_4.8H_2O$ solution was added to the above mixture. At this stage, the solution turned yellow and finally 1M NaOH was added to it to adjust the pH value to about 11 and a brownish-yellow solution was formed. The resulting solution was continuously stirred vigorously for 4 hours to obtain a precipitate. The temperature maintained during the mixing process was 90^0C. The precipitate thus obtained was washed several times with methanol, and the final solution was centrifuged, and dried, and a brownish-yellow powder was synthesized [73].

2.5.2 Synthesis of ZnS NPs by biological method

Jatropha curcas L. Latex is used for the synthesis of ZnS. The latex of J. curcas L. was collected early in the morning because the plant has more latex synthesis in the early morning. Crude latex was obtained by cutting the green stems of J. curcas plants. The milky white latex was stored at -40 C until further use. All aqueous solutions were prepared in triple distilled de-ionized water. In a typical reaction mixture, 1 mL of crude latex was diluted to 300 mL with triple-distilled deionized water to make it 0.3%, and 20 mL of this latex solution was taken and mixed with 20 mL of 2.5 mM aqueous zinc acetate solution. The mixture was kept at room temperature (27 °C) with continuous stirring for 24-48 hours using a magnetic stirrer in a laboratory environment. After 25 hours, the solution was observed to have a distinct yellowish-brown precipitate at the bottom of the flask. UV-visible spectra and photoluminescence of ZnS nanoparticles were taken at different time intervals of 25, 30, and 35 hours. After the reaction is complete, the precipitate is washed several times with distilled water. The final precipitate is dried in a vacuum oven at 50^o C for 1 hour. After the formation of ZnS nanoparticles, the suspension was sonicated to separate particles and one or two drops of the suspension was placed on porous carbon-coated copper grids and dried in a drying chamber [74].

3. Application

Nowadays, the rapid development of industrialization and urbanization results in a shortage of global energy resources and releases significant amounts of toxic and harmful chemical pollutants into the environment around us. to solve the aforementioned energy and environmental crises; thus, great efforts have been made to develop the science and technology required for sustainable and clean energy production.

Solar energy is the most abundant and clean source and creates artificial photosynthetic systems that can convert solar energy into energy. chemical fuels are highly desirable. Among the many proposed technologies, semiconductor photocatalytic technology has been recognized as one of the most studied solar-fuel strategies to address global energy shortages and environmental pollution.

On the one hand, semiconductor photocatalytic technology uses solar energy to produce several valuable chemical fuels, such as hydrogen, from the photocatalytic splitting of water through the reduction of hydrocarbons and carbon dioxide. On the other hand, the technology can clean the environment by photocatalytic degradation of various toxic and harmful chemical pollutants.

Semiconductor photocatalytic technology generally involves the excitation of photogenerated charge carriers by light photoabsorption, bulk diffusion, and surface reaction of photogenerated electrons. One of the biggest challenges is how to increase the efficiency of photocatalytic materials to increase the absorption of excitation light and reduce the aggregation of conjugated photocarbons. It depends on the properties of the photocatalytic materials, such as the width of E_g and the crystal structure. In general, photocatalytic materials, such as titanium dioxide, absorb only ultraviolet light when the E_g of the semiconductor is relatively large. The most suitable conventional semiconductor photocatalyst, titanium dioxide, has a wide band gap of 3.2 eV, and it can only absorb ultraviolet light with wavelengths less than 387 nm, which is about 3–5% of the total solar energy.

The photocatalytic efficiency of titanium dioxide is severely limited under sunlight irradiation. Conversely, if a semiconductor has a relatively narrow band gap, it can absorb the vast majority of visible light. As is well known, metal sulfides have a favorable conduction band position and associated narrow band gap, and thus are used as photocatalytic materials that respond to visible light [75].

3.1. Application of CdS and ZnS in solar cells

Due to its interesting optoelectronic properties, cadmium sulfide has various applications, one of which is solar panels. Structurally, CdS structures made using CdS thin films and CdS composites are used especially as a buffer layer in solar cells, where its superior optoelectronic properties play an important role in increasing device performance.

One of the distinguishing features of CdS thin films is that they can be precisely tuned for optical transparency through variations in thickness. An optimized thickness of 120 nm has been identified for solar cell applications, allowing for higher efficiency levels reaching an impressive 21%.

The preparation of CdS thin films has been studied using various chemical and physical methods. Among these methods, Chemical Vapor Deposition (CVD) is a particularly promising and cost-effective approach to obtain compact thin films. The preference for CVD is attributed to its ability to produce a highly compact layer that seamlessly surrounds the Transparent Conductive Oxide (TCO) layer. This compactness is crucial to ensure efficient electron transport in the structure of solar panels. Moreover, the choice of CVD is even more effective with its ability to impart chemical and thermal stability to the cadmium telluride (CdTe) thin film. This stability is important for the overall robustness and longevity of the solar cell device. Researchers consistently highlight the effectiveness of this method in producing high-performance solar cells with the highest efficiency when using CdS thin films made via CVD. However, the use of cadmium in solar cells is an environmental concern due to its toxicity. Therefore, CdS is mainly replaced by ZnS and its composites. Thus, even though it is less toxic, ZnS solar panels may face problems in achieving high efficiency. Ongoing research is focused on optimizing material properties and device architecture [76-78].

3.2. Application of CdS and ZnS in photocatalysis

In recent times, they prefer clean energy sources instead of fuel-based energy reserves. Currently, hydrogen energy is considered the cleanest type of energy in the world. Because its combustion produces only water vapor. There are different ways to get hydrogen, one of them is the process of splitting water. This division can be done in different ways. One of these methods is the electrolysis process. The use of electricity during electrolysis is one of the main disadvantages of this method. The next process is the photocatalysis process. During photocatalysis, light rays are used as a catalyst. The electrons of the substance that absorbs light rays pass from the valence band to the conduction band and generate an electron-hole pair. The resulting electrons and holes participate in redox (reduction-oxidation) reactions with water or other molecules adsorbed on the surface of the photocatalyst [79-81].

$$2H_2O + 2e^- \rightarrow H_2 + 2OH^+ \quad (4)$$

$$2H_2O \rightarrow O_2 + 4H^+ + 4e^- \quad (5)$$

Electrons can reduce certain compounds in reactions. Light rays can be absorbed only by compounds whose forbidden zone width is equal to the energy of UV and visible light rays. These are mainly semiconductor materials. In general, when the E_g of the semiconductor is relatively large (E_g < 3.0 eV), photocatalytic materials, such as titanium dioxide, can only absorb ultraviolet light. The most suitable traditional semiconductor photocatalyst, titanium dioxide, has a wide bandgap of 3.2 eV, and it can only accept ultraviolet light with a wavelength of less than 387 nm, which is about 3–5% of the total solar energy. Conversely, if the bandgap length of a semiconductor is relatively narrow (E_g < 3.0 eV), it can absorb the vast majority of visible light. As is well known, metal sulfides have a favorable conduction band position and associated narrow bandgap, and thus are used as visible light-responsive photocatalytic materials. Cadmium sulfide, a visible-light-responsive photocatalyst with a band gap of 2.4 eV, is one of the best semiconductors photocatalysts among various sulfides for photocatalytic H_2 production [82].

CdS has two negative aspects. First, since CdS nanoparticles are usually chemically active, they are subject to processes such as oxidation and photo corrosion, which negatively affect the quality of photocatalysis. Therefore, creating binary CdS-based nanocomposites, that is, combining CdS photocatalysts with other catalysts, is considered an attractive strategy for photocatalytic hydrogen production. Therefore, many studies have been conducted on CdS/ZnO nanocomposites, CdS/TiO_2 nanocomposites, binary CdS/graphene nanocomposites, and other binary CdS-based photocatalytic materials [83].

The second is its toxic property, which can be overcome by surfactants and surface modifications. Also, due to this deficiency of CdS, it is replaced by ZnS during use. Thus, ZnS has many advantages such as excellent charge-carrying properties (reduced carrier scattering and recombination), essentially n-type semiconductor, good thermal stability, toxicity, water insolubility, and relatively cheap price. Let's pay attention to the role of these structures in the photocatalysis process.

ZnS nanostructures are interesting objects for catalytic activities due to their excellent chemical stability against oxidation and hydrolysis. In addition, ZnS is abundant and non-toxic. Therefore, ZnS can play an important role as a catalyst in environmental protection by removing organic and toxic pollutants from water. ZnS has been used as a semiconductor photocatalyst for photoreduction dehalogenation of halogenated benzene derivatives, photocatalytic degradation of water pollutants, and photocatalytic reduction of toxic metal ions. In addition, recently ZnS photocatalyst also exhibited high activity for photocatalytic H_2 production.

The ZnS photocatalyst exhibits high activity for photocatalytic H_2 production even without any cocatalyst such as Pt. Doping foreign elements into ZnS is one of the strategies used to modify its electronic structure and prepare visible light-responsive materials due to their large E_g of 3.66 eV. The conducted studies show that hydrogen production increases by photocatalysis from materials obtained by doping the surface of ZnS with metals such as Cu Bi Pt. To explain the mechanism of addition, let's focus on the stages of the catalysis process. In general, the semiconductor photocatalytic cycle consists of three stages. In the first step, illumination causes electrons to move from the valence band to the conduction band, leaving an equal number of vacancies (holes). Excited electrons and holes migrate to the surface. They then react with absorbed electron donors (D) and electron acceptors (A), respectively. In the second stage, most of the electron-hole pairs recombine, transferring the incoming energy in the form of heat or emitted light. A commonly used approach to prevent the recombination of electron-hole pairs is to incorporate co-catalysts such as Pt, Pd, NiO, and RuO_2 on the semiconductor surface. The heterojunctions formed between the base semiconductor and the co-catalyst provide an internal electric field that facilitates the separation of electrode pairs and results in faster charge transport. Moreover, these co-catalysts exhibit better conductivity, lower overpotential, and higher catalytic activity than the parent semiconductor. Therefore, they are often used for the development of photocatalytic reactions [84,85].

3.3. Application of CdS and ZnS in sensors

In recent years, with the development of industry and increased traffic of internal combustion engines such as motorcycles and vehicles, air pollution has become serious due to hazardous exhaust gases such as volatile organic compounds, CO, SO_2, H_2S NH_3, and NO_2.

is a problem related to its harmful effects on plants, aquatic animals and human health. Therefore, the development of highly sensitive gas sensors for monitoring these toxic gases is extremely important in terms of improving the quality of the environment and protecting people from excessive exposure to such hazardous gases. In the past, various metal oxide semiconductor materials with different morphologies have been investigated for gas sensor applications. The gas sensor mechanism for semiconducting metal oxides can be attributed to the change in electrical conductivity caused by the chemical interaction of gas molecules with the surface of metal oxides. This mechanism mainly involves gas adsorption, charge transfer, and desorption processes. Typically, after metal oxides come in contact with air, oxygen molecules are adsorbed on the surface, and ionized oxygen species (O^{2-}, or O^{-}) are formed by capturing electrons from the conduction band of the metal oxides. metal oxides exhibit a high resistance state in air due to the formation of a contact zone. When reductive gas molecules approach the surface, they react with oxygen species, which results in the release of electrons into the surface layer of metal oxides. thus, the permeability increases. Compared to metal oxides, sensors based on ZnS nanostructures exhibit high chemical stability, but this area has been little explored. ZnS is also used in the preparation of humidity and biosensors in ion sensors [86].

The unique properties of structures based on cadmium sulfide (CdS) nanoparticles are currently used for various sensor applications. CdS/CdTe heterostructure devices were fabricated using the RF sputter deposition method in nanoparticle research. These devices exhibited effective electrical resistivity higher than 10^6 Ohm-cm for CdS and 10^9 Ohm-cm for CdTe thin films. These heterojunction devices are specifically designed for X-ray imaging sensors, demonstrating their potential in high-performance applications. In addition, CdS and CdSe sensors for oxygen gas detection were investigated with different fabrication methods. For CdS, electrohydrodynamic sputtering was applied, while CdSe was thermally evaporated. Analysis of these sensors included X-ray and photoelectron Spectroscopy measurements, which revealed important insights. The shift in communication energy was observed to vary in response to the chemical nature of the oxygen radicals, which provides valuable information on the sensitivity and selectivity of the sensors to different oxygen species. These advances highlight the versatility of CdS-based structures in sensor technology, with applications ranging from high-resistance X-ray imaging sensors to oxygen gas sensors. The tailored properties of CdS nanoparticles and their integration into heterostructure devices demonstrate their potential to address specific sensing needs, and ongoing research in this area continues to explore new approaches and applications [87-90].

In some studies, CdS-based sensors have been compared with other commonly used sensors to explain their properties. CdS-based sensors are fabricated by a fabrication process involving the deposition of partially crystalline CdS powder from an aqueous suspension onto an alumina substrate. These deposited layers are reinforced with catalysts from platinum (Pt) group metals. The sensors have demonstrated significant sensitivity to different gas molecules when modulated by light of specific frequencies. The degree of sensitivity depended on the catalyst and the concentration of impurities. The properties of these sensors, including dark resistance and photosensitivity, were thoroughly investigated for various parameters such as gas concentration, sensor temperature, and frequency of modulating light. A recent advance in sensor technology involved the development of a new fiber-optic surface plasmon resonance sensor. This sensor has metal semiconductor core

nanocomposite layers composed of CdS, PbS, ZnO, and CdSe. The performance of the sensor was systematically investigated concerning various metals and evaluations were made based on sensitivity and signal-to-noise ratio. Comparisons were made with an Au-SiO_2 surface plasmon resonance sensor. In addition, UV sensors were fabricated using high-resistivity CdS and ZnSe layers grown on the CdS surface. These UV sensors exhibited high quantum efficiency. Thin films of CdS (from 30 to 200 nm) and CdSe (from 10 to 100 nm) were involved in the preparation of nano and microcrystalline sensors by physical vapor deposition. The thin films exhibited crystallite sizes of 8 nm, and CdS photoconductive devices were observed to be more sensitive to various substances including water, ethanol, ammonia, acetone, and iodine compared to CdSe photoconductive sensors [91-93].

3.4. Application of CdS and ZnS in bionanotechnology

By combining the engineering of biomolecules with nanoscale materials, the development of hybrid materials becomes possible. These hybrids combine the intrinsic properties of biomaterials with the exceptional optoelectronic and catalytic properties of nanoscale materials to offer novel optimized recognition and response-enhancing properties.

Significant progress has been made in the use of CdS nanomaterials for various biological applications. In particular, microscopic sensing devices have been successfully developed using fluorescent nanoparticles that can precisely attach to biological molecules. Recent advances include the development of nanoparticles composed of CdS and silicon dioxide, capped with polymer chains containing biotin at the ends. This innovative approach demonstrates the integration of multiple materials, each with unique properties, to create hybrid structures with enhanced functionality for biological research and detection applications [94-96].

The synergistic combination of CdS nanomaterials with biological objects opens up possibilities for the development of advanced biosensors, diagnostic tools, and other bioanalytical devices. The reported developments demonstrate the potential to exploit the unique properties of nanoscale materials to enhance the performance and versatility of biological applications. Ongoing research in this area continues to explore new combinations of materials and innovative engineering approaches to further advance the capabilities of hybrid nanomaterial-bioentity systems.

For example, sulfur-containing nanomaterials possess nanometric scale, water dispersibility, excellent catalytic activity, conductivity, biosafety, photoactivity, and fascinating optical properties, which make them useful in various biosensing applications. Metal sulfide nanomaterials have been used as photoactive materials in biosensing systems to generate light-excited photocurrent [97].

CdS QDs outperform conventional fluorescent materials due to their photostability and wide range of excitation wavelengths. CdS NPs are the most promising nanomaterials for coating electrodes because they have outstanding photocatalytic activity, significant band gap, and high electrical conductivity. Sulfur-containing QDs can stably bind to biomolecules due to their functional groups (eg, amine, carboxyl, and sulfhydryl groups), which act as common reaction sites in biological systems. The toxic properties of CdS nanoparticles are their biggest drawback and also enable their use in medicine. The positive charge of CdS NPs changes the internal structure of bacterial cells and creates an electrostatic interaction

with the negatively charged proteins on their surface as they pass through the membrane. When thiol groups in proteins interact with ions released from NPs, ROS are generated, which disrupt cell structure and subsequently cell function. After binding CdS NPs to the protein layer, inhibition of active transport, dehydrogenase, and enzymatic activity occurs in the periplasmic zone, thus inhibiting the synthesis of DNA, RNA, and proteins, followed by cell lysis. The scientists' research shows that CdS NPs showed greater antibacterial and antifungal activity than conventional drugs when tested against several food pathogens, including Pseudomonas aeruginosa, Bacillus licheniformis, Escherichia coli and Aspergillus flavus [98-100].

CdS NPs vary in toxicity depending on their size, chemical composition, and coating. NPs are thought to have high cytotoxic potential due to their unique properties such as small size, high surface-to-volume ratio, and gradual release capabilities. Cell death can occur due to the generation of reactive oxygen species (ROS) or the release of internal cadmium ion (Cd^{+2}) from CdS NPs into the cellular environment. Surface oxidation of CdS NPs leads to the release of cadmium ions from CdS NPs into the cellular environment. Based on this property, it is used in the preparation of drugs for the destruction of cancer cells [101]

Conclusion

In conclusion, the polymorphism observed in ZnS and CdS, particularly in their hexagonal and cubic crystal structures, plays a pivotal role in determining their electronic and optical properties. The band gap, emerges as a critical parameter impacted by the crystal structure, showcasing distinctive behaviors in the two materials. Notably, ZnS exhibits a larger band gap in its hexagonal form compared to the cubic structure, whereas CdS nanoparticles display an increased band gap in the hexagonal structure relative to their cubic counterparts

The significance of this polymorphism is further underscored by the intricate relationship between material dimensions and properties. As evidenced by various research studies, the synthesis methods employed exert a profound influence on the size and morphology of ZnS and CdS nanoparticles. Quantum confinement effects come into play, elucidating the variation in band gaps as a consequence of nanoparticle size. This dynamic interplay between crystal structure and dimensionality not only enhances our fundamental understanding of these materials but also expands the range of potential applications.

The conducted studies collectively underscore the versatility of ZnS and CdS, presenting opportunities to tailor their properties for specific applications by manipulating their crystal structure and dimensions. The diverse range of properties that evolve with changing dimensions, such as band gap modulation, positions these materials as promising candidates across multiple technological domains. This review contributes to the burgeoning field of semiconductor nanomaterials, fostering a deeper appreciation for the intricate relationship between crystallography, synthesis methods, and the resultant properties of ZnS and CdS. The insights gleaned from this exploration pave the way for future advancements and applications in areas such as optoelectronics, sensors, and catalysis.

REFERENCE

1. Prabhu, R. R., & Khadar, M. A. (2005). Characterization of chemically synthesized CdS nanoparticles. Pramana, 65, 801-807.
2. Sivasubramanian, V., Arora, A. K., Premila, M., Sundar, C. S., & Sastry, V. S. (2006). Optical properties of CdS nanoparticles upon annealing. Physica E: Low-dimensional Systems and Nanostructures, 31(1), 93-98.
3. Rao, B. S., Kumar, B. R., Reddy, V. R., Rao, T. S., & Chalapathi, G. J. C. L. (2011). Preparation and characterization of CdS nanoparticles by chemical co-precipitation technique. Chalcogenide Lett, 8(3), 177-185.
4. Chandra, B. P., Chandra, V. K., & Jha, P. (2015). Luminescence of II-VI semiconductor nanoparticles. Solid State Phenomena, 222, 1-65.
5. Singh, V., Sharma, P. K., & Chauhan, P. (2011). Synthesis of CdS nanoparticles with enhanced optical properties. Materials Characterization, 62(1), 43-52.
6. Jacak, L., Hawrylak, P., & Wojs, A. (2013). Quantum dots. Springer Science & Business Media.
7. Qutub, N., & Sabir, S. (2012). Optical, thermal, and structural properties of CdS quantum dots synthesized by a simple chemical route. International Journal of Nanoscience and Nanotechnology, 8(2), 111-120.,
8. Subila, K. B., Kishore Kumar, G., Shivaprasad, S. M., & George Thomas, K. (2013). Luminescence properties of CdSe quantum dots: role of crystal structure and surface composition. The Journal of Physical Chemistry Letters, 4(16), 2774-2779.
9. Firsov, D., Vorobjev, L., Panevin, V., Fedosov, N., Shalygin, V., Samsonenko, J., ... & Werner, P. (2005). Light absorption and photoluminescence in quantum dots and artificial molecules. Acta Physica Polonica A, 107(1), 158-162.
10. Ahamad, T., Majeed Khan, M. A., Kumar, S., Ahamed, M., Shahabuddin, M., & Alhazaa, A. N. (2016). CdS quantum dots: growth, microstructural, optical, and electrical characteristics. Applied Physics B, 122, 1-8.
11. Lakowicz, J. R., Gryczynski, I., Gryczynski, Z., & Murphy, C. J. (1999). Luminescence spectral properties of CdS nanoparticles. The Journal of Physical Chemistry B, 103(36), 7613-7620.
12. Ekimov, A. I., Efros, A. L., & Onushchenko, A. A. (1985). Quantum size effect in semiconductor microcrystals. Solid State Communications, 56(11), 921-924.
13. Jassim, S., Abbas, A., AL-Shakban, M., & Ahmed, L. (2021). Chemical Vapour Deposition of CdS Thin Films at Low Temperatures from Cadmium Ethyl Xanthate. Egyptian Journal of Chemistry, 64(5), 2533-2538.
14. Nan, W., Niu, Y., Qin, H., Cui, F., Yang, Y., Lai, R., ... & Peng, X. (2012). Crystal structure control of zinc-blende CdSe/CdS core/shell nanocrystals: synthesis and structure-dependent optical properties. Journal of the American Chemical Society, 134(48), 19685-19693.
15. Furey, W. F., Robbins, A. H., Clancy, L. L., Winge, D. R., Wang, B. C., & Stout, C. D. (1986). Crystal structure of Cd, Zn metallothionein. Science, 231(4739), 704-710
16. Xiong, Y., Zhang, J., Huang, F., Ren, G., Liu, W., Li, D., ... & Lin, Z. (2008). Growth and phase-transformation mechanisms of nanocrystalline CdS in Na2S solution. The Journal of Physical Chemistry C, 112(25), 9229-9233.
17. Hullavarad, N. V., Hullavarad, S. S., & Karulkar, P. C. (2008). Cadmium sulfide (CdS) nanotechnology: synthesis and applications. Journal of nanoscience and nanotechnology, 8(7), 3272-3299.
18. Warner, J. H., & Tilley, R. D. (2005). Synthesis and Self-Assembly of Triangular and Hexagonal CdS Nanocrystals. Advanced Materials, 17(24), 2997-3001.
19. Soltani, N., Gharibshahi, E., & Saion, E. (2012). Band gap of cubic and hexagonal cds quantum dots-experimental and theoretical studies. Chalcogenide Lett, 9(7), 321-328.
20. Yong, K. T., Sahoo, Y., Swihart, M. T., & Prasad, P. N. (2007). Shape control of CdS nanocrystals in one-pot synthesis. The Journal of Physical Chemistry C, 111(6), 2447-2458.
21. Ballentyne, D. W. G., & Ray, B. (1961). Electroluminescence and crystal structure in the alloys system ZnS-CdS. Physica, 27(3), 337-341.
22. Suresh, S. (2014). Studies on the dielectric properties of CdS nanoparticles. Applied Nanoscience, 4, 325-329.

23. Li, F., Bi, W., Kong, T., Wang, C., Li, Z., & Huang, X. (2009). Effect of sulfur sources on the crystal structure, morphology, and luminescence of CdS nanocrystals prepared by a solvothermal method. Journal of alloys and compounds, 479(1-2), 707-710.
24. Jamali, S., SAEIVAR, I. Z. E., & Farjami, S. S. (2007). Synthesis, optical, and structural characterization of CdS nanoparticles.
25. Hao, E., Sun, H., Zhou, Z., Liu, J., Yang, B., & Shen, J. (1999). Synthesis and optical properties of CdSe and CdSe/CdS nanoparticles. Chemistry of materials, 11(11), 3096-3102.,
26. Vacassy, R., Scholz, S. M., Dutta, J., Plummer, C. J. G., Houriet, R., & Hofmann, H. (1998). Synthesis of controlled spherical zinc sulfide particles by precipitation from homogeneous solutions. Journal of the American Ceramic Society, 81(10), 2699-2705.
27. Mehmood, R. Y., Afsar, M. F., Jamil, A., Fareed, S., Siddique, F., Bhatti, M. H., ... & Rafiq, M. A. (2021). Study of electric conduction mechanisms, dielectric relaxation behavior, and density of states in zinc sulfide nanoparticles. Journal of Taibah University for Science, 15(1), 1144-1155.
28. Woods-Robinson, R., Han, Y., Zhang, H., Ablekim, T., Khan, I., Persson, K. A., & Zakutayev, A. (2020). Wide band gap chalcogenide semiconductors. Chemical Reviews, 120(9), 4007-4055.
29. HURMA, Tülay. Structural and optical properties of nanocrystalline ZnS and ZnS: Al films. Journal of Molecular Structure, 2018, 1161: 279-284.
30. Bhushan, M., Jha, R., & Bhardwaj, R. (2019). Reduced band gap and diffusion controlled spherical n-type ZnS nanoparticles for absorption of UV-Vis region of the solar spectrum. Journal of Physics and Chemistry of Solids, 135, 109021.
31. Fang, X., Zhai, T., Gautam, U. K., Li, L., Wu, L., Bando, Y., & Golberg, D. (2011). ZnS nanostructures: from synthesis to applications. Progress in Materials Science, 56(2), 175-287.
32. Kole, A. K., & Kumbhakar, P. (2012). Cubic-to-hexagonal phase transition and optical properties of chemically synthesized ZnS nanocrystals. Results in physics, 2, 150-155.
33. La Porta, F. A., Andres, J., Li, M. S., Sambrano, J. R., Varela, J. A., & Longo, E. (2014). Zinc blende versus wurtzite ZnS nanoparticles: control of the phase and optical properties by tetrabutylammonium hydroxide. Physical Chemistry Chemical Physics, 16(37), 20127-20137.
34. Saravanan, R. S. S., Pukazhselvan, D., & Mahadevan, C. K. (2012). Studies on the synthesis of cubic ZnS quantum dots, capping, and optical–electrical characteristics. Journal of alloys and compounds, 517, 139-148.,
35. Kaur, N., Kaur, S., Singh, J., & Rawat, M. (2016). A review on zinc sulfide nanoparticles: from synthesis, properties to applications. J Bioelectron Nanotechnol, 1(1), 1-5.
36. La Porta, F. A., Ferrer, M. M., De Santana, Y. V., Raubach, C. W., Longo, V. M., Sambrano, J. R., ... & Varela, J. A. (2013). Synthesis of wurtzite ZnS nanoparticles using the microwave-assisted solvothermal method. Journal of Alloys and Compounds, 556, 153-159.
37. Li, S., & Yang, G. W. (2010). Phase transition of II-VI semiconductor nanocrystals. The Journal of Physical Chemistry C, 114(35), 15054-15060.
38. Wang, Z., Daemen, L. L., Zhao, Y., Zha, C. S., Downs, R. T., Wang, X., ... & Hemley, R. J. (2005). Morphology-tuned wurtzite-type ZnS nanobelts. Nature materials, 4(12), 922-927
39. Kozhevnikova, N. S., Vorokh, A. S., & Rempel', A. A. (2010). Preparation of stable colloidal solution of cadmium sulfide CdS using ethylenediaminetetraacetic acid. Russian Journal of General Chemistry, 80, 391-394.
40. Borah, J. P., Barman, J., & Sarma, K. C. (2008). Structural and optical properties of ZnS nanoparticles. Chalcogenide Lett, 5(9), 201-208.
41. Dalei, K. (2014). Synthesis and characterization of cadmium sulfide nanoparticles and their utilization in the removal of cadmium from aqueous solution (Doctoral dissertation).
42. Raghavan, U. (2011). Using aqueous foams to synthesize cadmium sulfide nanoclusters.
43. Regmi, A., Basnet, Y., Bhattarai, S., & Gautam, S. K. (2023). Cadmium Sulfide Nanoparticles: Synthesis, Characterization, and Antimicrobial Study. Journal of Nanomaterials, 2023.
44. Carrillo, A. (2018). Low-temperature synthesis of CdS and ZnS nanoparticles by solution method using an anionic surfactant. Instituto de Ingeniería y Tecnología.

45. Yu, W. W., & Peng, X. (2002). Formation of high-quality CdS and other II–VI semiconductor nanocrystals in noncoordinating solvents: tunable reactivity of monomers. Angewandte Chemie International Edition, 41(13), 2368-2371.
46. Wan, Z., Yang, H., Luan, W., Tu, S. T., & Zhou, X. (2010). Facile synthesis of monodisperse CdS nanocrystals via micro reaction. Nanoscale Research Letters, 5, 130-137.
47. Haggata, S. W., Li, X., Cole-Hamilton, D. J., & Fryer, J. R. (1996). Synthesis and characterization of II–VII semiconductor nanoparticles by the reaction of a metal alkyl polymer adduct with hydrogen sulfide. Journal of Materials Chemistry, 6(11), 1771-1780.
48. Üzar, N., & Arikan, M. Ç. (2011). Synthesis and investigation of optical properties of ZnS nanostructures. Bulletin of Materials Science, 34, 287-292.
49. Dewi, R. P., Nurdiana, A., Astuti, L., Ragadita, R., & Nandiyanto, A. B. D. (2021). Synthesis of Zinc Sulfide Nanoparticles by Various Methods. Arabian Journal of Chemical and Environmental Research, 8(02), 355-371.
50. Hamed, Z. H., Ahmed, K. E. A., & Elsheikh, H. A. (2021). Synthesis and characterization of ZnS nanoparticles by chemical precipitation method. Aswan University Journal of Environmental Studies, 2(2), 147-154.
51. Suresh, S. (2013). Synthesis, structural, and dielectric properties of zinc sulfide nanoparticles. International Journal of Physical Sciences, 8(21), 1121-1127.
52. Li, G., Zhai, J., Li, D., Fang, X., Jiang, H., Dong, Q., & Wang, E. (2010). One-pot synthesis of monodispersed ZnS nanospheres with high antibacterial activity. Journal of Materials Chemistry, 20(41), 9215-9219.
53. Ummartyotin, S., & Infahsaeng, Y. (2016). A comprehensive review on ZnS: From synthesis to an approach on solar cell. Renewable and Sustainable Energy Reviews, 55, 17-24.
54. Sonker, R. K., Yadav, B. C., Gupta, V., & Tomar, M. (2020). Synthesis of CdS nanoparticle by the sol-gel method as low-temperature NO2 sensor. Materials Chemistry and Physics, 239, 121975.
55. Abd Al-Zahra, A., & Al-Sammarraie, A. K. M. A. (2022). Synthesis and Characterization of Zinc Sulfide Nanostructure by Sol-Gel Method. Chemical Methodologies, 6(1), 67-73. doi: 10.22034/chemm.2022.1.7
56. Sanchez-Lopez, J. C., Reddy, E. P., Rojas, T. C., Sayagues, M. J., Justo, A., & Fernández, A. (1999). Preparation and characterization of CdS and ZnS nanosized particles obtained by the inert gas evaporation method. Nanostructured Materials, 12(1-4), 459-462
57. Mazumdar, S., Tamilselvan, M., & Bhattacharyya, A. J. (2015). Optimizing Photovoltaic Response by Tuning Light-Harvesting Nanocrystal Shape Synthesized Using a Quick Liquid–Gas Phase Reaction. ACS Applied Materials & Interfaces, 7(51), 28188-28196.
58. Fuller, E. N., Schettler, P. D., & Giddings, J. C. (1966). New method for prediction of binary gas-phase diffusion coefficients. Industrial & Engineering Chemistry, 58(5), 18-27.
59. Husain, S., & Haryanti, N. H. (2021, February). Synthesize of CdS nanoparticles using the liquid-gas method. In Journal of Physics: Conference Series (Vol. 1816, No. 1, p. 012112). IOP Publishing.
60. Haryanti, N. H. SYNTHESIZE OF CDS NANOPARTICLES USING LIQUID-GAS METHOD.
61. Chen, J., Li, Y., Wang, Y., Yun, J., & Cao, D. (2004). Preparation and characterization of zinc sulfide nanoparticles under a high-gravity environment. Materials Research Bulletin, 39(2), 185-194.
62. Fedyaeva, O. N., Vostrikov, A. A., Sokol, M. Y., & Shatrova, A. V. (2014). Zinc sulfidation by H2S and H2S/H2O supercritical fluids: Synthesis of nanoparticles and catalytic effect of water. The Journal of Supercritical Fluids, 95, 669-676.
63. Sanchez-Lopez, J. C., Reddy, E. P., Rojas, T. C., Sayagues, M. J., Justo, A., & Fernández, A. (1999). Preparation and characterization of CdS and ZnS nanosized particles obtained by the inert gas evaporation method. Nanostructured Materials, 12(1-4), 459-462.
64. Paunovic, M., & Schlesinger, M. (2006). Fundamentals of electrochemical deposition. john wiley & sons.
65. Granot, E., Patolsky, F., & Willner, I. (2004). Electrochemical assembly of a CdS semiconductor nanoparticle monolayer on surfaces: Structural properties and photoelectrochemical applications. *The Journal of Physical Chemistry B*, *108*(19), 5875-5881.
66. Ameen, S., Akhtar, M. S., Kim, Y. S., & Shin, H. S. (2012). Synthesis and electrochemical impedance properties of CdS nanoparticles decorated polyaniline nanorods. *Chemical Engineering Journal*, *181*, 806-812.

67. Yang, Y. J., He, L. Y., & Xiang, H. (2006). Electrochemical synthesis of free-standing CdS nanoparticles in ethylene glycol. *Russian Journal of Electrochemistry*, *42*, 954-958.
68. Gorer, S., Ganske, J. A., Hemminger, J. C., & Penner, R. M. (1998). Size-selective and epitaxial electrochemical/chemical synthesis of sulfur-passivated cadmium sulfide nanocrystals on graphite. *Journal of the American Chemical Society*, *120*(37), 9584-9593.
69. Rahimi-Nasarabadi, M. (2014). Electrochemical synthesis and characterization of zinc sulfide nanoparticles. Journal of Nanostructures, 4(2), 211-216.
70. Hussain, I., Singh, N. B., Singh, A., Singh, H., & Singh, S. C. (2016). Green synthesis of nanoparticles and its potential application. *Biotechnology letters*, *38*, 545-560.
71. Gour, A., & Jain, N. K. (2019). Advances in green synthesis of nanoparticles. *Artificial cells, nanomedicine, and biotechnology*, *47*(1), 844-851.
72. Rafique, M., Sadaf, I., Rafique, M. S., & Tahir, M. B. (2017). A review on green synthesis of silver nanoparticles and their applications. *Artificial cells, nanomedicine, and biotechnology*, *45*(7), 1272-1291.
73. Dabhane, H., Ghotekar, S., Tambade, P., Pansambal, S., Murthy, H. A., Oza, R., & Medhane, V. (2021). A review on environmentally benevolent synthesis of CdS nanoparticle and their applications. Environmental Chemistry and Ecotoxicology, 3, 209-219.
74. Hudlikar, M., Joglekar, S., Dhaygude, M., & Kodam, K. (2012). Latex-mediated synthesis of ZnS nanoparticles: green synthesis approach. Journal of Nanoparticle Research, 14, 1-6.
75. Coughlan, C., Ibanez, M., Dobrozhan, O., Singh, A., Cabot, A., & Ryan, K. M. (2017). Compound copper chalcogenide nanocrystals. Chemical Reviews, 117(9), 5865-6109.
76. Amiri, O., Emadi, H., Hosseinpour-Mashkani, S. S. M., Sabet, M., & Rad, M. M. (2014). Simple and surfactant-free synthesis and characterization of CdS/ZnS core–shell nanoparticles and their application in the removal of heavy metals from aqueous solution. RSC Advances, 4(21), 10990-10996.
77. Castillo, R. H., Acosta, M., Riech, I., Santana-Rodríguez, G., Mendez-Gamboa, J., Acosta, C., & Zambrano, M. (2017). Study of ZnS/CdS structures for solar cell applications. Optik, 148, 95-100.
78. Reddy, C. V., Shim, J., & Cho, M. (2017). Synthesis, structural, optical, and photocatalytic properties of CdS/ZnS core/shell nanoparticles. Journal of Physics and Chemistry of Solids, 103, 209-217.
79. Soltani, N., Saion, E., Yunus, W. M. M., Erfani, M., Navasery, M., Bahmanrokh, G., & Rezaee, K. (2014). Enhancement of visible light photocatalytic activity of ZnS and CdS nanoparticles based on organic and inorganic coating. Applied Surface Science, 290, 440-447.
80. Fatahi, P., Roy, A., Bahrami, M., & Hoseini, S. J. (2018). Visible-light-driven efficient hydrogen production from CdS nanorods anchored with co-catalysts based on transition metal alloy nanosheets of NiPd, NiZn, and NiPdZn. ACS Applied Energy Materials, 1(10), 5318-5327.
81. Reddy, C. V., Shim, J., & Cho, M. (2017). Synthesis, structural, optical, and photocatalytic properties of CdS/ZnS core/shell nanoparticles. Journal of Physics and Chemistry of Solids, 103, 209-217.
82. Khodamorady, M., & Bahrami, K. (2023). A novel ZnS-CdS nanocomposite as a visible active photocatalyst for degradation of synthetic and real wastewaters. Scientific Reports, 13(1), 2177.
83. Cheng, L., Xiang, Q., Liao, Y., & Zhang, H. (2018). CdS-based photocatalysts. Energy & Environmental Science, 11(6), 1362-1391.
84. Hoang, A. T., Pandey, A., Chen, W. H., Ahmed, S. F., Nizetic, S., Ng, K. H., ... & Nguyen, X. P. (2023). Hydrogen production by water splitting with the support of metal and carbon-based photocatalysts. ACS Sustainable Chemistry & Engineering, 11(4), 1221-1252.
85. Páll, B., Mersel, M. A., Pekker, P., Makó, É., Vágvölgyi, V., Németh, M., ... & Horváth, O. (2023). Photocatalytic H2 Production by Visible Light on Cd0. 5Zn0. 5S Photocatalysts Modified with Ni (OH) 2 by Impregnation Method. International Journal of Molecular Sciences, 24(12), 9802.
86. Bai, X., Zhang, Y., Gao, W., Zhao, D., Yang, D., & Jia, N. (2020). Hollow ZnS–CdS nanocage-based photoelectrochemical sensor combined with molecular imprinting technology for sensitive detection of oxytetracycline. Biosensors and Bioelectronics, 168, 112522.
87. Borgohain, R., Boruah, P. K., & Baruah, S. (2016). Heavy-metal ion sensor using chitosan-capped ZnS quantum dots. Sensors and Actuators B: Chemical, 226, 534-539.

88. Prokopenko, S. L., Gunya, G. M., Makhno, S. M., & Gorbyk, P. P. (2017). Room-temperature gas sensor based on semiconductor nanoscale heterostructures ZnS/CdS. Хімія, фізика та технологія поверхні, (8,№ 4), 432-438.
89. Navale, S. T., Mane, A. T., Chougule, M. A., Shinde, N. M., Kim, J., & Patil, V. B. (2014). Highly selective and sensitive CdS thin film sensors for detection of NO 2 gas. RSC Advances, 4(84), 44547-44554.
90. Tanne, J., Schafer, D., Khalid, W., Parak, W. J., & Lisdat, F. (2011). Light-controlled bioelectrochemical sensor based on CdSe/ZnS quantum dots. Analytical chemistry, 83(20), 7778-7785.
91. Zhang, L., Dong, R., Zhu, Z., & Wang, S. (2017). Au nanoparticles decorated ZnS hollow spheres for highly improved gas sensor performances. Sensors and Actuators B: Chemical, 245, 112-121.
92. Willoughby, A., Capper, P., & Kasap, S. Wiley Series in Materials for Electronic and Optoelectronic Applications.
93. Yadava, L., Verma, R., & Dwivedi, R. (2010). Sensing properties of CdS-doped tin oxide thick film gas sensor. Sensors and Actuators B: Chemical, 144(1), 37-42.
94. Mahle, R., Kumbhakar, P., Nayar, D., Narayanan, T. N., Sadasivuni, K. K., Tiwary, C. S., & Banerjee, R. (2021). Current advances in bio-fabricated quantum dots emphasize the study of mechanisms to diversify their catalytic and biomedical applications. Dalton Transactions, 50(40), 14062-14080
95. Athinarayanan, J., Periasamy, V. S., & Alshatwi, A. A. (2020). Simultaneous fabrication of carbon nanodots and hydroxyapatite nanoparticles from fish scale for biomedical applications. Materials Science and Engineering: C, 117, 111313.
96. Ehtesabi, H., Hallaji, Z., Najafi Nobar, S., & Bagheri, Z. (2020). Carbon dots with pH-responsive fluorescence: a review on synthesis and cell biological applications. Microchimica Acta, 187, 1-18.
97. Kaur, J., Saxena, M., & Rishi, N. (2021). An overview of recent advances in biomedical applications of click chemistry. Bioconjugate Chemistry, 32(8), 1455-1471.
98. Wang, J., & Qiu, J. (2016). A review of carbon dots in biological applications. Journal of materials science, 51, 4728-4738.
99. Ghasempour, A., Dehghan, H., Ataee, M., Chen, B., Zhao, Z., Sedighi, M., ... & Shahbazi, M. A. (2023). Cadmium Sulfide Nanoparticles: Preparation, Characterization, and Biomedical Applications. Molecules, 28(9), 3857.
100. Li, G., Zhai, J., Li, D., Fang, X., Jiang, H., Dong, Q., & Wang, E. (2010). One-pot synthesis of monodispersed ZnS nanospheres with high antibacterial activity. Journal of Materials Chemistry, 20(41), 9215-9219.
101. Swartjes, J. J., Sharma, P. K., Kooten, T., van der Mei, H. C., Mahmoudi, M., Busscher, H. J., & Rochford, E. T. (2015). Current developments in antimicrobial surface coatings for biomedical applications. Current Medicinal Chemistry, 22(18), 2116-2129.

JOURNAL OF BAKU ENGINEERING UNIVERSITY - PHYSICS
2023. Volume 7, Number 2 *Pages 79-89*

UOT: 537.6/.8
PACS: 75.75.CD; 82.35.NP

RECENT ADVANCES IN THE USE OF POLYMER NANOCOMPOSITES AS ELECTROMAGNETIC WAVE SCREENING MATERIALS: A REVIEW

HABIBA SHIRINOVA
Baku State University
Department of Chemical Physics of Nanomaterials
h.shirinova@bk.ru
BAKU, AZERBAIJAN

ABSTRACT

Devices and equipment working based on electromagnetic waves play an important role in all areas of our daily lives. However, electromagnetic interference can cause serious problems with human health, information security, etc. One of the main tasks of materials science is the preparation and development of effective materials that protect against electromagnetic interference. Currently, polymer-based nanocomposite materials have great potential for shielding electromagnetic waves. The incorporation of magnetic nanoparticles into thermoplastic polymers also offers an attractive alternative. Devices and equipment that operate on the basis of electromagnetic waves play an important role in our daily lives. However, electromagnetic interference can cause serious problems with human health, information security, etc. One of the main tasks of materials science is the preparation and development of effective materials that protect against electromagnetic interference. Currently, polymer-based nanocomposite materials have great potential for shielding electromagnetic waves. Nanocomposites produced by incorporation of magnetic nanoparticles into thermoplastic polymers also should be highlighted as an attractive alternative. This article provides a review of the literature on the unique properties of polymer nanocomposites compared to traditional materials used for shielding electromagnetic waves, in particular the prospects for using magnetic nanoparticles as fillers for these nanocomposites. Meanwhile, the article also raises remaining open-questions related to the mechanism of shielding of electromagnetic waves by polymer nanocomposites.

KEY WORDS: polymer nanocomposites, magnetic nanocomposites, electromagnetic interference shielding

ПОСЛЕДНИЕ ДОСТИЖЕНИЯ В ИСПОЛЬЗОВАНИИ ПОЛИМЕРНЫХ НАНОКОМПОЗИТОВ В КАЧЕСТВЕ МАТЕРИАЛОВ ЭКРАНИРУЮЩИХ ЭЛЕКТРОМАГНИТНЫЕ ВОЛН: ОБЗОР

РЕЗЮМЕ

Устройства и оборудование, работающие на основе электромагнитных волн, играют важную роль в нашей повседневной жизни. Тем не менее, электромагнитные помехи могут вызвать серьезные проблемы со здоровьем человека, информационной безопасностью и т. д. Одной из основных задач материаловедения является подготовка и разработка эффективных материалов, защищающих от электромагнитных помех. В настоящее время нанокомпозитные материалы на основе полимеров имеют большой потенциал для экранирования электромагнитных волн. В качестве привлекательной альтернативы также следует выделить нанокомпозиты, полученные путем включения магнитных наночастиц в термопластичные полимеры.. В данной статье представлен обзор литературы об уникальных свойствах полимерных нанокомпозитов по сравнению с традиционными материалами, используемыми для экранирования электромагнитных волн, в частности о перспективах использования магнитных наночастиц в качестве наполнителей для этих нанокомпозитов. Тем временем, в статье также поднимаются темы, оставшиеся открытыми, связанные с механизмом экранирования электромагнитных волн полимерными нанокомпозитами.

КЛЮЧЕВЫЕ СЛОВА*: *полимерные нанокомпозиты, магнитные нанокомпозиты, защита от электромагнитных помех

POLIMER NANOKOMPOZITLƏRIN ELEKTROMAQNIT DALĞALARINA QARŞI EKRANLAYICI KIMI ISTIFADƏSINDƏ SON NAILIYYƏTLƏR : İCMAL

XÜLASƏ

Elektromaqnit dalğaları əsasında çalışan cihaz və avadanlıqlar bizim gündəlik həyatımızda vacib rol oynayır. Buna baxmayaraq, elektromaqnit dalğalarının yaratdığı küylər insan sağlamlığı, informasiya təhlükəsizliyi və s. ilə bağlı ciddi problemlərə səbəb ola bilər. Materialşünaslığın qarşısında duran əsas məsələlərdən biri elektromaqnit küylərdən qoruya bilən effektiv materialların alınması və işlənməsidir. Hazırda polimer əsaslı nanokompozit materiallar elektromaqnit dalğalarına qarşı ekranlaşdırıcıların hazırlanması üçün böyük potensiala malikdir. Maqnit nanohissəciklərin termoplastik polimerlərə daxil edilməsi ilə alınan nanokompozitlər də cəlbedici alternativ kimi qeyd edilməlidir. Bu məqalə elektromaqnit dalğalarını ekranlaşdıran ənənəvi materiallarla müqayisədə polimer nanokompozitlərin unikal xüsusiyyətlərinə dair ədəbiyyat icmalı, xüsusən də bu nanokompozitlər üçün doldurucu kimi maqnit nanohissəciklərdən istifadənin perspektivləri təqdim edilmişdir. Eyni zamanda, məqalədə elektromaqnit dalğalarının polimer nanokompozitlər tərəfindən ekranlaşdırılmasının mexanizmi ilə bağlı açıq qalan mövzulara da toxunulmuşdur.

AÇAR SÖZLƏR: polimer nanokompozitlər, maqnit nanokompozitlər, elektromaqnit küylərdən qorunma

1. INTRODUCTION

Electric devices certainly make life easier, however electromagnetic radiation pollutesthe environment and endangers human health [1]. The diversity of electromagnetic radiation (EMR) sources is growing. A vast range of frequencies are employed in electromagnetic radiation [2-3]. It is inevitable that the combined effects of electromagnetic radiation will have an impact on biological and technical object functionality as well as life activity. The technique of electromagnetic(EM) shielding involves employing special materials, tools, and technologies to lower the intensity of electromagnetic waves to a predetermined level [4-7]. Field intensity reduction is required to shield personnel or property from electromagnetic radiation's effects or to stop information from unintentionally leaking through electromagnetic radiation [8]. Moreover, semiconductor components [9] and integrated circuits [10] can be harmed by interference caused by strong fields . In order to ensure shielding, specific screens that allow radiation to be reflected, absorbed, scattered, or a combination of these processes can be created [11-14].

Creating shielding systems that protect against electromagnetic radiation is a challenging and significant task. Finding a complete answer to the problem of EM radiation protection while maintaining information security is the primary technical requirement placed on such systems. One of the goals of contemporary material science is to develop new kinds of materials that can be used as protective coatings against electromagnetic radiation and guarantee information security [15]. Many materials have been created and used for this purpose.

2.1. Traditional materials for EMI shielding application

Materials derived from metals and metal alloys were thought to be the most widely used shielding coatings until today. Electromagnetic interference (EMI) shielding materials based on metal and metal oxide are frequently used to shield electronic devices from uninvited electromagnetic radiation [16-18]. Common materials for electromagnetic shielding include various metals such as iron, copper, chromium, aluminum, brass, nickel, silver, steel, and tin [19-21]. The physical properties of the metal that influence shielding effectiveness are conductivity, permeability, thickness, and weight [22-24]. Less conductive metals like steel or

stainless steel absorb magnetically dominant waves, while highly conductive metals like copper, silver, and brass reflect electrically dominant waves [25]. Excellent conductivity makes materials like copper, aluminum, and their alloys useful for EMI shielding [26].

Despite the fact that every material on this list is effective against electromagnetic radiation, there are a number of restrictions on their use. Their fatal flaws prevented them from being widely used[26-30].

Metal-based coatings have relatively higher densities. For example, materials made of steel are heavy because of their high density . It should be also highlighted in particular that metal-based coatings are not very elastic, corrode easily, that is why it is relatively difficult to manufacture them for practical use [31-32]. In addition compared to pure metals like copper or aluminum, some metal alloys may be more costly or difficult to produce [33].

Furthermore, metal coatings are limited to the frequency ranges in which each material can function. Coatings based on metals are highly electrically conductive. Because of current dissipations brought on by high electrical conductivity, permeability rapidly decreases at high frequencies, and their absorption bandwidth is comparatively small [34]. For example, copper coatings are limited to use as only radiofrequency radiation shields.

2.2.Polymer-based materials as an alternative to metal-based materials for EMI shielding applications.

Light weight, high shielding, the ability to operate in a wide frequency range, and multifunctionality are the characteristics of an ideal EM wave absorber [35]. Low densities, processibility, and even electromagnetic properties of polymers allow them to overcome the aforementioned issues and aid in the design of the perfect EM wave absorber [36]. Conductive polymers- or carbon-based materials can be used as an alternative to metal-based materials for eletromagnetic interference shielding applications [37]. Polymer-based materials have been seen as having great potential as a potential replacement for the listed methods of protecting against electromagnetic radiation in recent years [38-40]. The following are some significant benefits of applying polymer-based nanocomposites in this situation:

- Since polymer-based nanocomposites are naturally light, they can be used in applications where weight is an important consideration [41-42].
- Design versatility that may be difficult to achieve with conventional metal-based solutions is provided by polymer-based nanocomposites, which are flexible and readily molded into a variety of shapes [43-44].
- The electrical conductivity and electromagnetic interference shielding efficacy of polymer-based nanocomposites can be tailored by manipulating variables such as the type and portions of nanoparticles incorporated into the polymer matrix [45-46].
- Polymer-based nanocomposites, in contrast to metals, are typically resistant to corrosion, which makes them appropriate for use in harsh environments [47-48].
- Polymer nanocomposites can effectively shield electromagnetic fields from various wavelengths of radiation over a wide frequency range [49-50].

The polymer-based materials utilized for EM shielding can be polymers with conducting functional groups or polymer composites with special additives [51]. Thermoplastic polymers are the favored matrix material when using polymer-based composite materials to create EM shieldings [52-53]. A particular kind of polymer known as a thermoplastic melts to a soft or liquid state at high temperatures and returns to its original strength upon cooling. Most of the time, the molecules of thermoplastic polymers have a random arrangement with a linear or branching structure [54-56]. Temperature affects their physical states, but it has no effect on the chemical composition of the structure. It is possible to repeat the process of changing an aggregate's form from hard to soft and back again, but the properties remain unchanged even after multiple processings. The raw materials are pliable, moldable, and scalable. Thermoplastic materials offer an unparalleled blend of strength, light weight, and resistance to corrosion, enabling the partial removal of metal.

It should be mentioned that there is special interest in the research of metal- and metal-oxide-thermoplastic polymer- based nanocomposite materials for EMI shielding [57]. Specifically, due to their futures like relatively low density, salability in open air conditions, metal oxides are widely used as conductive additives for thermoplastic polymer in the preparation of shielding materials against electromagnetic radiation. Nanocomposites produced by dispersion of the metals or metal-oxide nanoparticles in the thermoplastic polymer are appealing solutions for EMI-related problems due to their unique properties. The selection of the nanoparticles [58] and thermoplastic polymer [59], dispersion of the filler in matrix [60], interphase interaction between components [61] are important parameters thermoplastic polymer- metal-oxide nanoparticles-based nanocomposites for EMI shielding. Consistent EMI shielding performance depends on achieving uniform dispersion of metal-oxide nanoparticles within the polymer matrix. Various metal oxides can be used as nanoparticles for EMI shielding applications, including iron oxide nanoparticles(hematite (α-Fe_2O_3) [62] and magnetite (Fe_3O_4) [63-66], magnesium Oxide (MgO) [67], tungsten oxide nanoparticles (WO_3) [68], nickel oxide nanoparticles (NiO) [69], cobalt oxide nanoparticles(CoO) [70], bismuth oxide (Bi_2O_3) nanoparticles [71].

2.3. Carbon nanotubes-thermoplastic polymer- based nanocomposites for EMI shielding application

Single or several concentric cylinders made from graphene sheets make up carbon nanotubes (CNTs). Due to their small diameter and relatively long length CNTs possess a very high aspect ratio[14]. Furthermore, CNTs have additional advantages such as low weight high electrical conductivity, and mechanical strength, which make them perfect fillers for polymer nanocomposites that screen electromagnetic waves [72-73]. Carbon nanotubes can be single-walled and multi-walled [74]. Electromagnetic interference shielding applications have demonstrated the potential of both single-walled and multi-walled carbon nanotubes (SWCNTs and MWCNTs). Since MWCNTs and SWCNTs have distinct mechanical, thermal, and electrical characteristics, they are both great options for EMI shielding. SWCNTs can organize into dense networks that efficiently block EM waves at a variety of frequencies [75]. However, compared to MWCNTs, SWCNTs are often more costly to make [76]. As fillers in shielding materials, multi-walled carbon nanotubes also (MWCNTs) have several drawbacks despite their many benefits for EMI shielding [72-76].

- For MWCNTs to be used effectively in the nanocomposite creation, they must be uniformly dispersed throughout the matrix without damaging it. However, CNT dispersion in a polymer matrix is still a challenging process
- While MWCNTs can enhance the mechanical properties of materials when properly dispersed, their incorporation can also lead to trade-offs in mechanical performance.
- Depending on the needs of the application, high MWCNT concentrations may cause the material to become more brittle or stiff, which might be undesirable.

2.4. Magnetic nanoparticle-thermoplastic polymer- based nanocomposites for EMI shielding application

The incorporation of magnetic metal-oxide nanoparticles into thermoplastic polymers offers an attractive alternative for (EMI) shielding applications requiring both electromagnetic and magnetic shielding capabilities. Higher perspectives are thought to apply to magnetic nanocomposites made of submicron-sized ferrite particles as coatings that absorb high-frequency electromagnetic waves.

An essential component of magnetism is the presence of transition metals and rare earths with incomplete 3d and 4f shells, respectively [77]. Massive ferromagnets in an equilibrium (demagnetized) state contain uniformly magnetized areas—domains—separated by regions with a nonuniform distribution of magnetization—domain walls [78]. If to reduce the size of the sample, then there comes a moment when its volume can become commensurate with the equilibrium dimensions of the domains. The main reason for the appearance of single-domain particles is the fact that as the particle size decreases, the specific weight of the surface energy of the boundary layers between the domains increases, and it becomes comparable or even greater than the volumetric energy of the sample. In this case, the single-domain state becomes energetically more favorable [79]. The effect of superparamagnetism is the most notable distinction between the magnetic characteristics of a single-domain nanoparticle and those of a bulk ferromagnet. Superparamagnetism is a vital future that influences the effectiveness of the magnetic nanoparticles-nanocomposites for their EMI shielding application [80]. The superparamagnetic characteristics of the nanoparticle may be used to explain how magnetic nanoparticles interact with electromagnetic radiation. Particles' magnetic moments, which are in a single-domain condition, can reverse direction in response to outside stimuli. Even at temperatures below the Curie or Néel points, superparamagnetic particles exhibit paramagnetic behavior in the presence of an external magnetic field. Compared to paramagnets, these particles have a substantially higher magnetic susceptibility. Accordingly, superparamagnetic nanoparticle-containing nanocomposites have low coercitivity and high magnetic permeability, making them effective in absorbing electromagnetic radiation.

Ramazanov and his team showed that polymer nanocomposites on the basis of isotactic polypropylene (PP) and superparamagnetic magnetite (Fe_3O_4) nanoparticles are able to shield ultra-high-electromagnetic-waves (UHEMW) in the frequencies range from 0.1 to 30 GHz [81].

2.5. EMI Shielding Mechanisms

Through a variety of mechanisms, such as electromagnetic wave reflection, absorption, and scattering, metal-oxide nanoparticles aid in electromagnetic interference shielding. The overall effectiveness of the shielding is largely dependent on the electrical conductivity, dielectric characteristics, and interactions of the metal oxides with the polymer matrix. The shielding efficiency(SE) of the material interacting with electromagnetic waves is determined as the sum of reflection, re-reflection and absorption losses:

$$SE_T=SE_R+SE_A+SE_M \quad (1)$$

Here SE_R – energy attenuation of the incident waves due to reflection at the boundary of the media. SE_A- energy attenuation due to the energy losses in the thickness of the screen. SE_M –energy attenuation due to manifold reflections in the screen itself and the role of this attenuation is negligible. So, the shielding efficiency(SE) of the material mainly depends on SE_R and SE_A [82].

The SE_A is significantly influenced by the field frequency, electrical conductivity, and magnetic permeability of the shield material, configuration, dimensions, and thickness of the shield [83]. It should be noted here that, unlike a homogeneous system, the electrophysical parameters of a heterogeneous system itself depend on various parameters like the system composition, the nature and amount of the components, and their mutual interactions. If the shielding material is the nanocomposite, the difference in the electrical conductivities, magnetic permeabilities, and the process on the boundary of the components play vital roles in the shielding effects[65, 81-85].

Given their multi-interface structure and ability to enhance the frequency of numerous reflections and scatterings, nanocomposites are regarded as one of the most efficient materials for electromagnetic interference shielding [86-87].

However, unique and groundbreaking advancements in the realm of EMI shielding materials are still a long way off. There are still obstacles in the way of producing materials with the best possible performance, affordability, and sustainability, even with continuous research and development efforts [88].

The need to address changing technology trends, satisfy environmental goals, and improve performance will drive innovation in EMI shielding materials in the future. In the coming years, EMI shielding materials' full potential must be realized through cross-disciplinary cooperation and ongoing research.

REFERENCES

1. Lin, J. C. (2016). Human exposure to RF, Microwave, and Millimeter-Wave electromagnetic Radiation [Health Effects]. *IEEE Microwave Magazine*, *17*(6), 32–36. https://doi.org/10.1109/mmm.2016.2538540
2. Cress, G. O., Brady, B. H. G., & Rowell, G. A. (1987). Sources of electromagnetic radiation from fracture of rock samples in the laboratory. *Geophysical Research Letters*, *14*(4), 331–334. https://doi.org/10.1029/gl014i004p00331
3. Krafft, G., & Priebe, G. (2010). Compton sources of electromagnetic radiation. *Reviews of Accelerator Science and Technology*, *03*(01), 147–163. https://doi.org/10.1142/s1793626810000440
4. Fionov, A. S., Kraev, I., Yurkov, G. Y., Solodilov, V. I., Zhukov, A., Surgay, A., Kuznetsova, I., & Kolesov, V. (2022). Radio-Absorbing materials based on polymer composites and their application to solving the problems of electromagnetic compatibility. *Polymers*, *14*(15), 3026. https://doi.org/10.3390/polym14153026
5. Geetha, S., Kumar, K. K. S., Rao, C. R., Vijayan, M., & Trivedi, D. (2009). EMI shielding: Methods and materials—A review. *Journal of Applied Polymer Science*, *112*(4), 2073–2086. https://doi.org/10.1002/app.29812
6. Shahzad, F., Alhabeb, M., Hatter, C. B., Anasori, B., Hong, S. M., Koo, C. M., & Gogotsi, Y. (2016). Electromagnetic interference shielding with 2D transition metal carbides (MXenes). *Science*, *353*(6304), 1137–1140. https://doi.org/10.1126/science.aag2421
7. Cao, M., Cai, Y., He, P., Shu, J., Cao, W., & Yuan, J. (2019). 2D MXenes: Electromagnetic property for microwave absorption and electromagnetic interference shielding. *Chemical Engineering Journal*, *359*, 1265–1302. https://doi.org/10.1016/j.cej.2018.11.051
8. Ryan, K. (2018). Return of the hidden number problem. IACR Transactions on Cryptographic Hardware and Embedded Systems, 146–168. https://doi.org/10.46586/tches.v2019.i1.146-168
9. Serkov, A., Breslavets, V., Breslavets, Y., & Yakovenko, I. (2023). Influence of electromagnetic radiation on resistance of semiconductor devices. Sistemi Upravlìnnâ, Navìgacìï Ta Zv'âzku, 1(71), 177–181 . https://doi.org/10.26906/sunz.2023.1.177
10. Öngel, K., Gümral, N., & Özgüner, İ. F. (2013). The Potential Effects of Electromagnetic Field: A review. DergiPark (Istanbul University)

    https://dergipark.org.tr/tr/pub/sducmfrr/issue/20738/221701
11. Liu, Z., Bai, G., Huang, Y., Ma, Y., Du, F., Li, F., Guo, T., Chen, Y. (2007). Reflection and absorption contributions to the electromagnetic interference shielding of single-walled carbon nanotube/polyurethane composites. Carbon, 45(4), 821-827 . https://doi.org/10.1016/j.carbon.2006.11.020
12. Bansala, T., Mukhopadhyay, S., Joshi, M., Doong, R., & Chaudhary, M. (2016). Synthesis and shielding properties of PVP-stabilized-AgNPs-based graphene nanohybrid in the Ku band. Synthetic Metals, 221, 86–94. https://doi.org/10.1016/j.synthmet.2016.07.034
13. Jayalakshmi, C., Inamdar, A., Anand, A., & Kandasubramanian, B. (2018). Polymer matrix composites as broadband radar absorbing structures for stealth aircrafts. Journal of Applied Polymer Science, 136(14). https://doi.org/10.1002/app.47241
14. Al-Saleh, M. H., & Sundararaj, U. (2009). Electromagnetic interference shielding mechanisms of CNT/polymer composites. Carbon, 47(7), 1738–1746. https://doi.org/10.1016/j.carbon.2009.02.030
15. Zhang, L., & Chen, Y. (2010). Performance Analysis and Function Simulation of Protective Clothing from Electromagnetic Radiation. Journal of Fiber Bioengineering and Informatics, 3(3), 153–158. https://doi.org/10.3993/jfbi12201006
16. Rajavel, K., Hu, Y., Zhu, P., & Wong, C. (2020). MXene/metal oxides-Ag ternary nanostructures for electromagnetic interference shielding. Chemical Engineering Journal, 399, 125791. https://doi.org/10.1016/j.cej.2020.125791
17. Sharma, V., Manna, K., Srivastava, S. K., & Chandra, A. (2018). Hollow nanostructures of metal oxides as efficient absorbers for electromagnetic interference shielding. Journal of Physics D: Applied Physics, 52(1), 015301. https://doi.org/10.1088/1361-6463/aae4f5
18. Uzun, S., Han, M., Strobel, C. J., Hantanasirisakul, K., Goad, A., Dion, G., & Gogotsi, Y. (2021). Highly conductive and scalable Ti3C2T -coated fabrics for efficient electromagnetic interference shielding. *Carbon*, *174*, 382 -389.

    https://doi.org/10.1016/j.carbon.2020.12.021

19. Shukla, V. (2019). Review of electromagnetic interference shielding materials fabricated by iron ingredients. *Nanoscale Advances*, *1*(5), 1640–1671. https://doi.org/10.1039/c9na00108e
20. Cheng, K. B., Ramakrishna, S., & Lee, K. (2000). Electromagnetic shielding effectiveness of copper/glass fiber knitted fabric reinforced polypropylene composites. *Composites Part A: Applied Science and Manufacturing*, *31*(10), 1039–1045. https://doi.org/10.1016/s1359-835x(00)00071-3
21. Huang, J. (1995). EMI shielding plastics: A review. *Advances in Polymer Technology*, *14*(2), 137–150. https://doi.org/10.1002/adv.1995.060140205
22. Roh, J., Chi, Y., Kang, T. J., & Nam, S. (2008). Electromagnetic shielding effectiveness of multifunctional metal composite fabrics. *Textile Research Journal*, *78*(9), 825–835. https://doi.org/10.1177/0040517507089748
23. Palanisamy, S., Tunáková, V., Hu, S., Yang, T., Dana, K., Venkataraman, M., Petrů, M., & Militký, J. (2021). Electromagnetic interference shielding of metal coated ultrathin nonwoven fabrics and their factorial design. Polymers, 13(4),484 https://doi.org/10.3390/polym13040484
24. Song, Q., Chen, B., Zhou, Z., & Lu, C. (2021). Flexible, stretchable and magnetic Fe3O4@Ti3C2Tx/elastomer with supramolecular interfacial crosslinking for enhancing mechanical and electromagnetic interference shielding performance. *Science China Materials*, *64*(6), 1437–1448. https://doi.org/10.1007/s40843-020-1539-2
25. Huang, J. (1995b). EMI shielding plastics: A review. *Advances in Polymer Technology*, *14*(2), 137–150. https://doi.org/10.1002/adv.1995.060140205
26. Pandey, R. K., Tekumalla, S., & Gupta, M. (2020). EMI shielding of metals, alloys, and composites. In *Elsevier eBooks* (pp. 341–355). https://doi.org/10.1016/b978-0-12-817590-3.00021-x
27. Yin, J., Ma, W., Gao, Z., Lei, X., & Cui, J. (2022). A review of electromagnetic shielding fabric, Wave-Absorbing fabric and Wave-Transparent fabric. *Polymers*, *14*(3), 377. https://doi.org/10.3390/polym14030377
28. Sankaran, S., Deshmukh, K., Ahamed, M. B., & Pasha, S. K. K. (2018). Recent advances in electromagnetic interference shielding properties of metal and carbon filler reinforced flexible polymer composites: A review. *Composites Part A: Applied Science and Manufacturing*, *114*, 49–71. https://doi.org/10.1016/j.compositesa.2018.08.006
29. Lai, Z., Cheng, K., Zhao, T., Zhu, P., Liŭ, D., Liang, X., & Sun, R. (2023). A facile process to fabricate copper/nickel-coated polyurethane composite with high electromagnetic interference shielding performance. *Composites Communications*, *38*, 101487. https://doi.org/10.1016/j.coco.2022.101487
30. Liu, J., Yu, M., Yu, Z., & Nicolosi, V. (2023). Design and advanced manufacturing of electromagnetic interference shielding materials. Materials Today, 66, 245–272. https://doi.org/10.1016/j.mattod.2023.03.022
31. Luo, X., Wei, Y., Shen, J., Ma, N., & Li, C. (2023). Breaking the trade off between corrosion resistance and fatigue lifetime of the coated Mg alloy through cold spraying submicron-grain Al alloy coatings. *Journal of Magnesium and Alloys*. https://doi.org/10.1016/j.jma.2022.12.011
32. Wei, L., & Gao, Z. (2023). Recent research advances on corrosion mechanism and protection, and novel coating materials of magnesium alloys: a review. *RSC Advances*, *13*(12), 8427–8463. https://doi.org/10.1039/d2ra07829e
33. Hamilton, J. C. (1979). Prediction of surface segregation in binary alloys using bulk alloy variables. *Physical Review Letters*, *42*(15), 989–992. https://doi.org/10.1103/physrevlett.42.989
34. Guan, H., & Chung, D. (2020). Radio-wave electrical conductivity and absorption-dominant interaction with radio wave of exfoliated-graphite-based flexible graphite, with relevance to electromagnetic shielding and antennas. *Carbon*, *157*, 549–562. https://doi.org/10.1016/j.carbon.2019.10.071
35. Peymanfar, R., Dogari, H., Selseleh-Zakerin, E., Hedayatzadeh, M. H., Daneshvar, S., Amiri-Ramsheh, N., Ghafuri, H., Mirkhan, A., Ji, G., & Aslibeiki, B. (2023). Recent advances in microwave-absorbing materials fabricated using organic conductive polymers. *Frontiers in Materials*, *10*. https://doi.org/10.3389/fmats.2023.1133287
36. Kausar, A., & Ahmad, I. (2023). Conducting Polymer Nanocomposites for Electromagnetic Interference Shielding—Radical Developments. *Journal of Composites Science*, *7*(6), 240. https://doi.org/10.3390/jcs7060240
37. Liu, C., Wang, L., Liu, S., Tong, L., & Liu, X. (2020). Fabrication strategies of polymer-based electromagnetic interference shielding materials. *Advanced Industrial and Engineering Polymer Research*, *3*(4), 149–159. https://doi.org/10.1016/j.aiepr.2020.10.002

38. More, C. V., Alsayed, Z., Badawi, M. S., Thabet, A. A., & Pawar, P. P. (2021). Polymeric composite materials for radiation shielding: a review. *Environmental Chemistry Letters*, *19*(3), 2057–2090. https://doi.org/10.1007/s10311-021-01189-9
39. Kruželák, J., Kvasničáková, A., Hložeková, K., & Hudeč, I. (2021). Progress in polymers and polymer composites used as efficient materials for EMI shielding. *Nanoscale Advances*, *3*(1), 123–172. https://doi.org/10.1039/d0na00760a
40. Maraveas, C., Kyrtopoulos, I., Arvanitis, K. G., & Bartzanas, T. (2024). The Aging of Polymers under Electromagnetic Radiation. *Polymers*, *16*(5), 689. https://doi.org/10.3390/polym16050689
41. Paul, D. R., & Robeson, L. M. (2008). Polymer nanotechnology: Nanocomposites. *Polymer*, *49*(15), 3187–3204. https://doi.org/10.1016/j.polymer.2008.04.017
42. Gacitúa, E. W., Ballerini, A., & Zhang, J. (2005). POLYMER NANOCOMPOSITES: SYNTHETIC AND NATURAL FILLERS A REVIEW. *Maderas-ciencia Y Tecnologia*, *7*(3). https://doi.org/10.4067/s0718-221x2005000300002
43. Ghazzy, A., Naik, R. R., & Shakya, A. K. (2023). Metal–Polymer nanocomposites: a promising approach to antibacterial materials. *Polymers*, *15*(9), 2167. https://doi.org/10.3390/polym15092167
44. Fattahi, M., Hsu, C., Ali, A. A., Mahmoud, Z. H., Dang, N., & Kianfar, E. (2023). Severe plastic deformation: Nanostructured materials, metal-based and polymer-based nanocomposites: A review. *Heliyon*, *9*(12), e22559. https://doi.org/10.1016/j.heliyon.2023.e22559
45. Mahmoodi, M., Arjmand, M., Sundararaj, U., & Park, S. (2012). The electrical conductivity and electromagnetic interference shielding of injection molded multi-walled carbon nanotube/polystyrene composites. *Carbon*, *50*(4), 1455–1464. https://doi.org/10.1016/j.carbon.2011.11.004
46. Ramírez-Herrera, C. A., González, H. C. F., De La Torre, F., Benitez, L., Cabañas-Moreno, J. G., & Lozano, K. (2019). Electrical properties and electromagnetic interference shielding effectiveness of interlayered systems composed by carbon nanotube filled carbon nanofiber mats and polymer composites. *Nanomaterials*, *9*(2), 238. https://doi.org/10.3390/nano9020238
47. Pourhashem, S., Saba, F., Duan, J., Rashidi, A., Guan, F., Nezhad, E. G., & Hou, B. (2020). Polymer/Inorganic nanocomposite coatings with superior corrosion protection performance: A review. *Journal of Industrial and Engineering Chemistry*, *88*, 29–57. https://doi.org/10.1016/j.jiec.2020.04.029
48. Ulaeto, S. B., Ravi, R. P., Udoh, I. I., Mathew, G. M., & Rajan, T. (2023). Polymer-Based coating for steel protection, highlighting Metal–Organic Framework as functional actives: A review. *Corrosion and Materials Degradation*, *4*(2), 284–316. https://doi.org/10.3390/cmd4020015
49. Liang, C., Gu, Z., Zhang, Y., Ma, Z., Qiu, H., & Gu, J. (2021). Structural Design Strategies of Polymer Matrix composites for Electromagnetic Interference shielding: A review. *Nano-Micro Letters*, *13*(1). https://doi.org/10.1007/s40820-021-00707-2
50. Kim, H. W., Abdala, A., & Macosko, C. W. (2010). Graphene/Polymer nanocomposites. *Macromolecules*, *43*(16), 6515–6530. https://doi.org/10.1021/ma100572e
51. Tofail, S. a. M., Koumoulos, E. P., Bandyopadhyay, A., Bose, S., O'Donoghue, L. M., & Charitidis, C. A. (2018). Additive manufacturing: scientific and technological challenges, market uptake and opportunities. *Materials Today*, *21*(1), 22–37. https://doi.org/10.1016/j.mattod.2017.07.001
52. Zhou, J., & Lubineau, G. (2013). Improving electrical conductivity in polycarbonate nanocomposites using highly conductive PEDOT/PSS coated MWCNTs. *ACS Applied Materials & Interfaces*, *5*(13), 6189–6200. https://doi.org/10.1021/am4011622
53. Idris, F. M., Hashim, M., Abbas, Z., Ismail, I., Nazlan, R., & Ibrahim, I. R. (2016). Recent developments of smart electromagnetic absorbers based polymer-composites at gigahertz frequencies. *Journal of Magnetism and Magnetic Materials*, *405*, 197–208. https://doi.org/10.1016/j.jmmm.2015.12.070
54. Heckele, M., & Schomburg, W. K. (2003). Review on micro molding of thermoplastic polymers. *Journal of Micromechanics and Microengineering*, *14*(3), R1–R14. https://doi.org/10.1088/0960-1317/14/3/r01
55. Giboz, J., Copponnex, T., & Mélé, P. (2007). Microinjection molding of thermoplastic polymers: a review. *Journal of Micromechanics and Microengineering*, *17*(6), R96–R109. https://doi.org/10.1088/0960-1317/17/6/r02

56. Kargarzadeh, H., Huang, J., Lin, N., Ahmad, I., Marcos, M., Dufresne, A., Thomas, S., Gałęski, A. (2018). Recent developments in nanocellulose-based biodegradable polymers, thermoplastic polymers, and porous nanocomposites. Prog. Polym. Sci. 87, 197–227. https://doi.org/10.1016/j.progpolymsci.2018.07.008
57. Omana, L., Chandran, A., John, R. E., Wilson, R., George, K. C., Unnikrishnan, N. V., Varghese, S. S., George, G., Simon, S. M., & Paul, I. (2022). Recent Advances in Polymer nanocomposites for Electromagnetic Interference shielding: A review. *ACS Omega*, *7*(30), 25921–25947. https://doi.org/10.1021/acsomega.2c02504
58. Li, S., Lin, M., Toprak, M. S., Kim, D. K., & Muhammed, M. (2010). Nanocomposites of polymer and inorganic nanoparticles for optical and magnetic applications. Nano Reviews, 1(1), 5214. https://doi.org/10.3402/nano.v1i0.5214
59. Mahesh, V., Joladarashi, S., & Kulkarni, S. M. (2021). A comprehensive review on material selection for polymer matrix composites subjected to impact load. *Defence Technology*, *17*(1), 257–277. https://doi.org/10.1016/j.dt.2020.04.002
60. Bölük, M. Y., & Schreiber, H. P. (1990). Interfacial interactions and mechanical properties of filled polymers. *Journal of Applied Polymer Science*, *40*(9–10), 1783–1794. https://doi.org/10.1002/app.1990.070400931
61. Pramatarova, L., Radeva, E., Pecheva, E., Hikov, T., Krasteva, N., Dimitrova, R., Mitev, D., Montgomery, P., Sammons, R., & Altankov, G. (2011). The Advantages of Polymer Composites with Detonation Nanodiamond Particles for Medical Applications. In *InTech eBooks*. https://doi.org/10.5772/22903
62. Chen, K., Gupta, S., & Tai, N. (2021). Reduced graphene oxide/Fe2O3 hollow microspheres coated sponges for flexible electromagnetic interference shielding composites. *Composites Communications*, *23*, 100572. https://doi.org/10.1016/j.coco.2020.100572
63. Shirinova, H. A., Di Palma, L., Sarasini, F., Tirillò, J., Рамазанов, M. A., Hajiyeva, F. V., Sannino, D., Polichetti, M., & Galluzzi, A. (2016). Synthesis and characterization of magnetic nanocomposites for environmental remediation. *Chemical Engineering Transactions*, *47*, 103–108. https://doi.org/10.3303/cet1647018
64. Ramazanov, M. A., Shirinova, H. A., Hajiyeva, F. V., Sultanova, J. R., & Alizade, R. A. (2020). Magnetic properties of iron nanoparticles distributed in polymer matrix: theoretical and Experimental approach. *Acta Physica Polonica A*, *138*(6), 787–793. https://doi.org/10.12693/aphyspola.138.787
65. Ramazanov, M. A., Shirinova, H. A., Hajiyeva, F. V., & Bychanok, D. (2020). New Polymeric Three-Phase nanocomposites based on polyvinylidene fluoride, magnetite nanoparticles and Multi-Walled Carbon nanotubes: production, structure and properties. *J. Inorganic and Organometallic Polymers and Materials*, *30*(11), 4783–4791. https://doi.org/10.1007/s10904-020-01648-w
66. Ramazanov, M. A., Shirinova, H. A., & Hajiyeva, F. V. (2020). The impact of manufacturing technology, of the polypropylene matrix and iron oxide nanoparticles based magnetodielectric nanocomposites on electrophysical parameters. *Materials Chemistry and Physics*, *253*, 123287. https://doi.org/10.1016/j.matchemphys.2020.123287
67. Wang, W., Cui, R., Zhang, P., Wan, C., & Pan, W. (2021). High electromagnetic interference shielding effectiveness in MgO composites reinforced by aligned graphene platelets. *Journal of the American Ceramic Society*, *104*(6), 2868–2878. https://doi.org/10.1111/jace.17667
68. Sastry, D. N., Revanasiddappa, M., Suresh, T., Kiran, Y. T. R., & Raghavendra, S. C. (2018). Electromagnetic shielding effectiveness studies on polyaniline/CSA-WO3 composites at KU band frequencies. *AIP Conference Proceedings*. https://doi.org/10.1063/1.5032914
69. Dinakaran, K., Senthamilselvi, S., Gayathri, T., Kavitha, N., & Roy, D. (2023). Enhanced electromagnetic interference shielding in nickel oxide and graphene composite nanostructures loaded polyvinylidene difluoride thin films. *Journal of the Indian Chemical Society*, *100*(10), 101091. https://doi.org/10.1016/j.jics.2023.101091
70. Paul, B. K., Mondal, D., Bhattacharya, D., Datta, S., Kundu, M., Mondal, I., Halder, P., Sarkar, S. K., Ghosh, A., Mandal, T., & Das, S. (2023). Transition metal impregnated nanostructured oxide material for broadband electromagnetic interference shielding: A theoretical and experimental insight. *Chemical Engineering Journal*, *459*, 141560. https://doi.org/10.1016/j.cej.2023.141560
71. Maestre, C. V., & Santos, G. N. C. (2023). Effect of bismuth oxide nanoparticle on the electromagnetic interference shielding and thermal stability of industrial waste based-geopolymer composites. *Scientific Reports*, *13*(1). https://doi.org/10.1038/s41598-023-27623-2

72. Saito, R., Dresselhaus, G., & Dresselhaus, M. S. (1998). *Physical properties of carbon nanotubes*. https://doi.org/10.1142/p080
73. Thostenson, E. T., Z, R., & Chou, T. (2001). Advances in the science and technology of carbon nanotubes and their composites: a review. *Composites Science and Technology*, *61*(13), 1899–1912. https://doi.org/10.1016/s0266-3538(01)00094-x
74. Kumar, M., & Ando, Y. (2010). Chemical vapor deposition of carbon nanotubes: A review on growth mechanism and mass production. *Journal of Nanoscience and Nanotechnology*, *10*(6), 3739–3758. https://doi.org/10.1166/jnn.2010.2939
75. Bocchini, S., Annibale, E., Frache, A., & Camino, G. (2008). MWNT Surface Self-Assembling in Fire Retardant Polyethylene-Carbon nanotubes nanocomposites. *E-polymers*, *8*(1). https://doi.org/10.1515/epoly.2008.8.1.209
76. De Volder, M., Tawfick, S., Baughman, R. H., & Hart, A. J. (2013). Carbon Nanotubes: present and future commercial applications. *Science*, *339*(6119), 535–539. https://doi.org/10.1126/science.1222453
77. Baczewski, L. T., Givord, D., Alameda, J. M., Diény, B., Nozières, J. P., Rebouillat, J., & Préjean, J. (1993). Magnetism in Rare-Earth-Transition metal systems. Magnetization reversal and Ultra-High susceptibility in sandwiched thin films based on rare-Earth and cobalt alloys. *Acta Physica Polonica A*, *83*(5), 629–641. https://doi.org/10.12693/aphyspola.83.629
78. Bar'yakhtar, V. G., Bogdanov, A. N., & Yablonskiĭ, D. A. (1988). The physics of magnetic domains. *Soviet Physics, Ycnexu*, *31*(9), 810–835. https://doi.org/10.1070/pu1988v031n09abeh005621
79. Ulusoy, U. (2023). A review of particle shape effects on material properties for various engineering applications: from macro to nanoscale. *Minerals*, *13*(1), 91. https://doi.org/10.3390/min13010091
80. Held, G. A., Grinstein, G., Doyle, H., Sun, S., & Murray, C. B. (2001). Competing interactions in dispersions of superparamagnetic nanoparticles. *Physical Review*, *64*(1). https://doi.org/10.1103/physrevb.64.012408
81. Ramazanov, M. A., Hajiyeva, F. V., Maharramov, A. M., Di Palma, L., Sannino, D., Takafuji, M., Mammadov, H. M., Hasanova, U., Shirinova, H. A., & Bayramova, Z. A. (2017). New magnetic polymer nanocomposites on the basis of isotactic polypropylene and magnetite nanoparticles for adsorption of ultrahigh frequency electromagnetic waves. *Polymer-plastics Technology and Engineering*, *57*(5), 449–458. https://doi.org/10.1080/03602559.2017.1320721
82. Chung, D. (2000). Materials for electromagnetic interference shielding. *Journal of Materials Engineering and Performance*, *9*(3), 350–354. https://doi.org/10.1361/105994900770346042
83. Orasugh, J. T., & Ray, S. S. (2023). Functional and Structural Facts of Effective Electromagnetic Interference shielding materials: a review. *ACS Omega*, *8*(9), 8134–8158. https://doi.org/10.1021/acsomega.2c05815
84. Shahapurkar, K., Gelaw, M., Tirth, V., Soudagar, M. E. M., Shahapurkar, P., Mujtaba, M., Mc, K., & Ahmed, G. M. S. (2022). Comprehensive review on polymer composites as electromagnetic interference shielding materials. *Polymers and Polymer Composites*, *30*, 096739112211021. https://doi.org/10.1177/09673911221102127
85. Zecchi, S., Cristoforo, G., Bartoli, M., Tagliaferro, A., Torsello, D., Rosso, C., Boccaccio, M., & Acerra, F. (2024). A Comprehensive Review of Electromagnetic Interference Shielding Composite Materials. *Micromachines*, *15*(2), 187. https://doi.org/10.3390/mi15020187
86. Thomassin, J., Jérôme, C., Pardoen, T., Bailly, C., Huynen, I., & Detrembleur, C. (2013). Polymer/carbon based composites as electromagnetic interference (EMI) shielding materials. *Materials Science and Engineering: R: Reports*, *74*(7), 211–232. https://doi.org/10.1016/j.mser.2013.06.001
87. Manna, K., & Srivastava, S. K. (2020). Tuning of Shells in Trilaminar Core@Shell Nanocomposites in Controlling Electromagnetic Interference through Switching of the Shielding Mechanism. *Langmuir*, *36*(16), 4519–4531. https://doi.org/10.1021/acs.langmuir.9b03313
88. Ayub, S., Guan, B. H., & You, K. Y. (2023). Electromagnetic interference shielding mechanisms of MMG@PVDF composites for a broadband frequency range. *Materials Today Communications*, *35*, 106273. https://doi.org/10.1016/j.mtcomm.2023.106273

JOURNAL OF BAKU ENGINEERING UNIVERSITY - PHYSICS
2023. Volume 7, Number 2 *Pages 90-99*

PACS: 11.15.-p
UOT: 539.193/.194

SPATIAL STRUCTURE OF THE SERORPHINE MOLECULE

Leyla AGAYEVA
Baku State University
leylanamig@mail.ru

ABSTRACT

The serorphine molecule belongs to the class of opioids derived from food substances. To study the spatial structure of the serorphin molecule, the potential energy of the system was chosen as the sum of non-valent, electrostatic, torsional interaction energies and hydrogen bond energy. The spatial structure of the Tyr1-Gly2-Phe3-Asn4-Ala5 serorphin molecule was studied by the method of theoretical conformational analysis based on the low-energy conformations of the amino acid residues tyrosine, glycine, phenylalanine, asparagine and alanine that form it. The collection of stable conformations of the serorphin molecule, the values of their dihedral rotation angles, and the inter- and internal interaction energies of the amino acid residues that stabilize them were determined. It has been shown that the spatial structure of this molecule is represented by eight forms of the main chain falling in the energy range of 0-4 kcal/mol. In low-energy conformations, the conformations of the two BRR and RRR forms of the main chain of the C-side tripeptide fragment of the molecule were favorable.

Keywords: nutrients, opioid, serorphin, spatial structure, conformation.

ПРОСТРАНСТВЕННАЯ СТРУКТУРА МОЛЕКУЛЫ СЕРОРФИНА

РЕЗЮМЕ

Молекула серорфина принадлежит к классу опиоидов, получаемых из пищевых веществ. Для изучения пространственной структуры молекулы серорфина потенциальная энергия системы была выбрана как сумма энергий невалентного, электростатического, торсионных взаимодействия и энергии водородной связи. Пространственную структуру молекулы серорфина Tyr1-Gly2-Phe3-Asn4-Ala5 изучали методом теоретического конформационного анализа, основанного на низкоэнергетических конформациях образующих ее аминокислотных остатков тирозина, глицина, фенилаланина, аспарагина и аланина. Определен набор стабильных конформаций молекулы серорфина, значения углов их двугранного поворота, а также энергии меж- и внутреннего взаимодействия аминокислотных остатков, стабилизирующих их. Показано, что пространственная структура этой молекулы представлена восемью формами основной цепи, попадающими в диапазон энергий 0–4 ккал/моль. В низкоэнергетических конформациях благоприятными оказались конформации двух форм BRR и RRR основной цепи С-стороннего трипептидного фрагмента молекулы.

Ключевые слова: нутриенты, опиоид, серорфин, пространственная структура, конформация.

SERORFİN MOLEKULUNUN FƏZA QURULUŞU

XÜLASƏ

Serorfin molekulu ərzaq maddələrindən alınmış opioidlər sinfinə mənsubdur. Serorfin molekulunun fəza quruluşunu öyrənmək üçün sistemin potensial enerjisi qeyri-valent, elektrostatik, torsion qarşılıqlı təsir enerjilərinin və hidrogen rabitəsi enerjisinin cəmi şəklində seçilmişdir. Nəzəri konformasiya analizi üsulu ilə Tyr1-Gly2-Phe3-Asn4-Ala5 serorfin molekulunun fəza quruluşu onu əmələ gətirən tirozin, qlisin, fenilalanin, asparagin və alanin aminturşu qalıqlarının aşağıenerjili konformasiyaları əsasında tədqiq olunmuşdur. Serorfin molekulunun stabil konformasiyaları yığımı, onların ikiüzlü fırlanma bucaqlarının qiymətləri, onları stabilləşdirən aminturşu qalıqları arası və daxili qarşılıqlı təsir enerjiləri müəyyən edilmişdir. Göstərilmişdir ki ,bu molekulun fəza quruluşu 0 – 4 kkal/mol enerji intervalına düşən əsas zəncirin səkkiz formasının konformasiyaları ilə təmsil edilir. Aşağıenerjili konformasiyalarda molekulun C-tərəf tripeptid fraqmentinin əsas zəncirinin iki BRR və RRR formalarının konformasiyaları əlverili olmuşdur.

Açar sözlər: qida maddələri, opioid, serorfin, fəza quruluşu, konformasiya.

Introduction

The study of the relationship between the biological functions and structures of peptide molecules is the basis of the study of their mechanisms of action at the molecular level. During such studies, the sequence of amino acids and the active center of which the peptide molecule is composed attract more attention. Because, precisely, the active center is responsible for their contact with receptors, transport and immunological activity. In addition, the study of modified analogues of natural peptides with longer duration of action is of great interest.

Regulatory peptides, first discovered in the second half of the twentieth century, are actively studied by both physiologists and pharmacologists, since the range of biological activity of peptides is extremely wide. They are one of the main links that unite the three regulatory systems of the body - nervous, endocrine and immune into a single whole. Currently, more than 9,000 physiologically active peptides have been characterized in different animal species and humans. These are short chains of amino acids (2-70 residues) that perform the function of signaling molecules. Most of these peptides cannot be confidently classified as either neurotransmitters or hormones, since they are synthesized both by neurons (transmitting a signal at the synapse level) and by cells of peripheral tissues (transmitting a signal over longer distances, like hormones). Regulatory peptides are characterized by an immediate effect on many systems of the body.

Opioid peptides are currently considered the most studied group of peptide signaling substances. Opium causes pain relief, sedation and sleep, as well as a euphoric state and a number of vegetative reactions. These peptides come in animal and plant origin. A number of exogenous peptides obtained from food have opiate-like properties. Such peptides were called exorphins. The discovery of the opioid activity of peptide food components has suggested that some foods may have effects on the central nervous system similar to opiate drugs. A number of milk exorphins have been discovered that have opioid receptor antagonist properties. These include casoxins A, B, C, human casoxin D, as well as lactoferroxins A, B and C, rubiscolines, soymorphins, lactorphines, serorphine. The possibility of the formation of these peptides during the hydrolysis of the corresponding proteins by peptidases of the gastrointestinal tract has been proven in vitro.

Casoxins and casomorphins are peptides that act on the opioid system, which influences the rate of digestion. Casomorphins are opioid agonists (activators), and casoxins are opioid antagonists. Casein is high in casoxins and casomorphins, which explains the reduced gastric capacity after consumption (as activation of the opioid system reduces intestinal motility). The physiological effects of antagonistic exorphins are still very poorly studied. Some milk exorphins (casomorphins, casoxins, lactoferroxins) can not only be formed during the digestion of milk in the gastrointestinal tract, but also contained in cheeses, since the technology for making cheese is associated with enzymatic processing [1-4].

Materials and methods

We have studied the structural and functional organizations of the opioid peptides enkephalins, endorphins, endomorphins, dynorphins, neoendorphins, adrenorphin, and the spatial structure of exorphins is currently being studied. This work is a continuation of our previous studies [5-15].

The molecule was calculated using the method of theoretical conformational analysis. The potential function of the system is chosen as the sum of nonvalent, electrostatic and torsional interactions and the energy of hydrogen bonds. Non-valent interactions were assessed using the Lennard-Jones potential. Electrostatic interactions were calculated in the monopole approximation according to Coulomb's law using partial charges on atoms. The conformational capabilities of the serorphin molecule were studied in an aqueous environment, and therefore the dielectric constant was taken to be 10. The energy of hydrogen bonds was estimated using the Morse potential. Our above-mentioned works detail the potential features used.

When presenting the calculation results, a classification of peptide structures according to conformations, main chain shapes, and peptide backbone shapes was used. Conformational states are completely determined by the values of the dihedral angles of the main and side chains of all amino acid residues included in a given molecule. The backbone forms of a fragment are formed by combinations of the forms of R, B, L residues in a given sequence. The forms of the dipeptide backbone can be divided into two classes - folded (f) and unfolded (e) forms, which are called shapes. All conformations are grouped by main chain shapes, and shapes by shapes. To designate the conformational states of residues, identifiers of the Xij type are used, where X defines the low-energy regions of the conformational map and ij...=11...,12...,13...,21... determines the position of the side chain, with index 1 corresponding to the angle value ranging from 0 to 120°, 2 – from 120° to -120°, and 3 – from -120° to 0°. Designations and readings of rotation angles correspond to the IUPAC-IUB nomenclature [16]. To calculate the spatial structure of peptide molecules was used a program developed by N.M.Godjaev and his staff [17].

Results and Discussion

Serorphin molecule consists of five amino acid residues, 75 atoms, 22 dihedral rotation angles. Serorphin molecule consists of tyrosine, glycine, phenylalanine, asparagine and alanine amino acid residues. The spatial structure of the serorphin molecule was studied based on the low-energy conformations of the amino acid residues forming it.

In order to study the spatial structure of the serorphin molecule, Tyr1 and Phe3 were taken in the R,B forms of the main chain, the χ angle was taken in the 60°, 180° and -60° states, which were possible due to the torsion potential, and the χ_2 angle was taken in the 90° state, which was possible due to the torsion potential. The χ_3 angle of the tyrosine amino acid side chain has two favorable states for the torsion potential: 0° and 180°. When changing from one of these states to another, the state of only one hydrogen atom in space changes, which does not affect the formation of the overall spatial structure of the molecule. The side chain of glycine amino acid consists of one atom, so its ψ and φ angles have large rotational freedom. R, B, L, P forms of glycine amino acid backbone were all chosen as starting variants. For the Asn4 amino acid residue, the R, B forms of the main chain, the 60°, 180°, and -60° states of the χ1 angle, which are possible according to the torsion potential, and the 90° and -90° states of the χ_2 angle, which are possible according to the torsion potential, were selected as the starting conformations. For Ala5 amino acid residue R, B forms of main chain, only χ_1=180° value of χ_1 were selected as starting conformations. The χ_1 angle also has three favorable states for the torsion potential, 60°, 180°, and -60°, but when switching from one to the other, one hydrogen atom replaces the other, so they have the same energy.

The number of possible shapes in a given molecule is 16. For this reason, the conformations of 16 shapes were calculated. Since the starting conformations were chosen as mentioned above, the conformations of the main chain 32 forms were calculated. As can be seen from the sequence of amino acid residues of the molecule, the molecule includes amino acid residues tyrosine and phenylalanine with two aromatic side chains, glycine and alanine amino acids with wide conformational possibilities, and aspartic amino acid with a polar side chain. At first glance, it can be assumed that there may be a favorable interaction between the side chain of the Tyr1 amino acid residue and the side chain of the Phe3 amino acid residue. Therefore, the possible conformations of the tripeptide fragment Tyr1-Gly2-Phe3 in the low-energy B-B conformation of Asn4 and Ala5 were initially calculated. For this, the interaction of Tyr1 and Phe3 amino acid residues in the 16 forms of the main chain of the Tyr1-Gly2-Phe3 tripeptide fragment was examined. In the first approximation, 144 conformations of the pentapeptide molecule were calculated. Calculations show that there is a sharp differentiation in the energies of the shapes and conformations of the main chain. Some of the calculated conformations were not spherically possible.

The number of possible shapes in a given molecule is 16. For this reason, the conformations of 16 shapes were calculated. Since the starting conformations were chosen as mentioned above, the conformations of the main chain 32 forms were calculated. As can be seen from the sequence of amino acid residues of the molecule, the molecule includes amino acid residues tyrosine and phenylalanine with two aromatic side chains, glycine and alanine amino acids with wide conformational possibilities, and aspartic amino acid with a polar side chain. At first glance, it can be assumed that there may be a favorable interaction between the side chain of the Tyr1 amino acid residue and the side chain of the Phe3 amino acid residue. Therefore, the possible conformations of the tripeptide fragment Tyr1-Gly2-Phe3 in the low-energy B-B conformation of Asn4 and Ala5 were initially calculated. For this, the interaction of Tyr1 and Phe3 amino acid residues in the 16 forms of the main chain of the Tyr1-Gly2-Phe3 tripeptide fragment was examined. In the first approximation, 144 conformations of the pentapeptide molecule were calculated. Calculations show that there is a sharp differentiation in the energies of the shapes and conformations of the main chain. Some of the calculated conformations were not spherically possible.

In the second stage of the study of the spatial structure of the serorphin molecule, in each of the 16 conformations selected in the first stage, the possible conformations of the angles χ_1 and χ_2 of the side chain in the R and B forms of the main chain of Asn4 according to the torsional potential energy were selected as the starting option. Therefore, in the first approximation, several hundred conformations of the main chain 32 forms belonging to the 16 shapes were calculated. The results of the calculations show that there is a sharp differentiation according to the energies of the 32 forms of the main chain, three forms of the main chain have high energy. The total energies of the calculated conformations of the 29 forms of the main chain vary in the range of (-11.4) – (-0.6) kcal/mol. The lowest energy conformation of each of the 29 forms of the main chain was selected, their shapes, non-valent, electrostatic, torsional interaction energies, total and relative energies are shown in table 1.

Table 1. Optimum conformations of the serorphin molecule, their shapes, the shapes of their main chains, the energy contribution of non-valent, electrostatic, torsion interactions, the total and relative energies.

№	Shapes	Conformation	U_{nv}	U_{el}	U_{tor}	U_{tot}	U_{rel}
1.	*feff*	$B_2LR_2R_{11}R_2$	-16.3	2.2	2.7	-11.4	0
		$R_2BR_2R_{11}R_2$	-15.9	4.0	3.0	-8.9	2.5
2.	*fefe*	$B_2LR_2B_{11}B_2$	-11.6	3.3	2.4	-5.9	5.5
		$R_2BR_2B_{11}B_2$	-14.4	2.2	2.8	-9.4	2.0
3.	*feef*	$B_2LB_1R_{11}R_2$	-15.6	4.0	2.0	-9.7	1.7
		$R_3BB_1R_{21}R_2$	-13.6	4.6	2.0	-6.9	4.5
4.	*feee*	$B_2LB_1B_{11}B_2$	-13.6	4.2	2.0	-7.3	4.1
		$R_3BB_1B_{11}B_2$	-12.1	4.8	2.2	-5.1	6.3
5.	*efef*	$B_3RB_1R_{11}R_2$	-15.1	3.4	2.8	-8.9	2.5
6.	*efee*	$R_3PB_2B_{31}B_2$	-14.7	5.2	2.5	-7.1	4.3
		$B_3RB_1B_{11}B_2$	-12.6	3.6	2.7	-6.4	5.0
7.	*ffff*	$B_2PR_2R_{31}R_2$	-14.3	3.5	2.0	-8.8	2.6
		$R_2RR_1R_{21}R_2$	-9.3	1.1	2.9	-7.6	3.8
8.	*fffe*	$R_2RR_1B_{21}B_2$	-8.2	2.2	2.2	-3.9	7.5
		$B_2PR_2B_{11}B_2$	-8.4	3.2	1.2	-4.0	7.4
9.	*ffef*	$B_2PB_1R_{31}R_2$	-13.9	3.1	2.8	-8.7	2.7
		$R_2RB_2R_{31}R_2$	-13.5	3.1	2.8	-7.6	3.8
10.	*ffee*	$B_2PB_1B_{11}B_2$	-12.4	3.0	2.2	-7.2	4.2
		$R_2RB_2B_{11}B_2$	-12.0	3.3	3.0	-5.7	5.7
11.	*effe*	$B_1RR_2R_{21}R_2$	-10.8	1.7	0.1	-8.4	3.0
12.	*efee*	$B_1RR_2B_{11}B_2$	-10.5	3.2	1.0	-6.3	5.1
13.	*eeef*	$B_2BB_2R_{21}R_2$	-15.6	4.9	2.8	-7.9	3.5
		$R_3LB_1R_{11}R_2$	-14.5	4.5	3.4	-6.6	4.8
14	*eeee*	$B_2BB_2B_{31}B_2$	-15.1	4.9	2.8	-7.4	4.0
		$R_3LB_1B_{11}B_2$	-11.0	5.1	1.5	-4.4	7.0
15.	*eeff*	$R_3LR_2R_{21}R_2$	-13.1	2.6	3.0	-7.5	3.9
		$B_2BR_2R_{11}R_2$	-12.9	4.6	2.2	-6.1	5.3
16.	*eefe*	$B_2BR_2B_{11}B_2$	-12.3	3.9	2.3	-6.1	5.3
		$R_3LR_2B_{11}B_2$	-11.6	4.2	2.1	-5.3	6.1

As can be seen from the table, the contribution of non-valent interaction energies to these conformations is in the range of (-16.3) – (-8.2) kcal/mol, electrostatic interaction energies are in the range of (-1.1) – (5.1) kcal/mol, torsional interaction energy (1.2) – (3.4) kcal/mol, total energy varies between (-11.4) – (-3.9) kcal/mol, and relative energy varies between (0.0) – (7.0) kcal/mol. The physiological functions performed by the serorphin molecule can in principle be performed in these spatial structures. As can be seen, the number of optimal conformations presented in table 1 is large. When analyzing those conformations, it becomes possible to select more compact structures in which they are formed. If you choose suitable structural types within those conformations, their number will be eight can be reduced to When selected as mentioned, it is possible to present eight structural types of the serorphin molecule. The low-energy conformations of the serorphin molecule, their shapes, the share, total and relative energies of non-valent, electrostatic, and torsion interaction energies are shown in table 2.

Table 2. Low-energy conformations of the serorphin molecule, their shapes, the shapes of their main chains, the energy contribution of non-valent, electrostatic, torsion interactions, the total and relative energies.

№	Shapes	**Conformation**	U_{nv}	U_{el}	U_{tor}	U_{tot}	U_{rel}
1.	*feff*	$B_2LR_2R_{11}R_2$	-16.3	2.2	2.7	-11.4	0
2.	*feef*	$B_2LB_1R_{11}R_2$	-15.6	4.0	2.0	-9.7	1.7
3.	*efef*	$B_3RB_1R_{11}R_2$	-15.1	3.4	2.8	-8.9	2.5
4.	*ffff*	$B_2PR_2R_{31}R_2$	-14.3	3.5	2.0	-8.8	2.6
5.	*ffef*	$B_2PB_1R_{31}R_2$	-13.9	3.1	2.8	-8.7	2.7
6.	*efff*	$B_1RR_2R_{21}R_2$	-10.8	1.7	0.1	-8.4	3.0
7.	*eeef*	$B_2BB_2R_{21}R_2$	-15.6	4.9	2.8	-7.9	3.5
8.	*eeff*	$R_3LR_2R_{21}R_2$	-13.1	2.6	3.0	-7.5	3.9

The contribution of non-valent interaction energies to the low-energy conformations shown in Table 2 is in the range of (-16.3) – (-10.8) kcal/mol, electrostatic interaction energy is in the range of (1.7) – (4.9) kcal/mol, torsional interaction energy (0.1) – (3.0) kcal/mol, total energy (-11.4) – (-7.5) kcal/mol, relative energies (0) – (4.0) kcal/mol. Various interaction energies that play a role in the stabilization of all the conformations shown in Table 2, monopeptide, dipeptide, tripeptide, tetrapeptide, pentapeptide interaction energies within an amino acid residue, between amino acid residues were calculated, their roles were determined, and their relative energies which smaller from (3.0) kcal/mol are shown in table 3, and the spatial arrangement of atoms in those conformations is shown in figure 1, 2, 3 and 4.

Table 3. Energy inside and between residual interactions in the conformations of the molecule serorphine: $B_2LR_2R_{11}R_2$ (U_{rel}=0 kcal/mol, first line), $B_2LB_1R_{11}R_2$ (U_{rel}=1.7 kcal/mol, second line), $B_3RB_1R_{11}R_2$ (U_{rel}=2.5 kcal/mol, third line), $B_2PR_2R_{31}R_2$ (U_{rel}=2.6 kcal/mol, fourth line), $B_2PB_1R_{31}R_2$ (U_{nis}= 2.7 kcal/mol, fifth line)

Tyr1	**Gly2**	**Phe3**	**Asn4**	**Ala5**	
2.0	-1.7	-0.8	-0.7	-7.5	
2.0	-1.9	-3.4	-0.5	-2.5	**Tyr1**
3.6	-0.9	-7.1	-1.1	-2.7	
3.8	-1.8	-1.8	-4.6	-2.3	
1.9	-1.6	-3.7	-1.2	-2.5	
	1.3	-1.0	-0.4	-2.3	
	1.3	-2.0	-0.2	-0.1	**Gly2**
	1.2	-1.0	-0.3	-0.1	
	1.3	-0.6	-2.0	0	
	1.3	-1.0	-0.1	0	
		0.1	-1.6	-1.6	
		-0.2	-1.5	-3.0	**Phe3**
		1.0	-1.5	-3.1	
		0.2	-1.2	-2.5	
		0.2	-1.8	-2.7	
			0	-1.5	
			-0.1	-1.6	**Asn4**
			-0.1	-1.5	
			0.1	-1.1	
			0.1	-1.2	
				1.6	
				1.6	**Ala5**
				1.6	
				1.7	
				1.6	

The global conformation of the molecule is $B_2LR_2R_{11}R_2$ belonging to the feff shape. This conformation is favorable due to both non-valent and electrostatic interaction energies.

As can be seen from Table 2, in this conformation, the non-valent interaction energy is up to (-16.3) kcal/mol, the electrostatic interaction energy is up to (2.2) kcal/mol, the torsional interaction energy is up to (2.7) kcal/mol gives share. This conformation forms the twisted structure of the molecule as the L-form of the Gly2 main chain, with a favorable electrostatic interaction between the positively charged N-side Tyr1 and the negatively charged C-side Ala5 of the molecule. Stabilization of the conformation depends on Tyr1-Gly2 (-1.7) kcal/mol, Tyr1-(Phe3-Asn4) (-1.5) kcal/mol, Tyr1-Ala5 (-7.5) kcal/mol, Gly2-Phe3 (-1.0) kcal/mol, Gly2-Ala5 (-2.3) kcal/mol, Phe3-Asn4 (-1.6) kcal/mol, Phe3-Ala5 (-1.6) kcal/mol, Asn4-Ala5 (-1.5) kcal/mol contribute (Table 3) .

The second stable conformation of the serorphin molecule is $B_2LB_1R_{11}R_2$ belongs to feef shape, its relative energy is (1.7) kcal/mol (Table 3). Apparently, this conformation differs from the global conformation due to the shape of the main chain of Phe3. The main chain of Phe3 in the B form separates the N-terminal Tyr1-Gly2 dipeptide fragment of the molecule from the C-terminal Asn4-Gly5 dipeptide fragment of the molecule. The contribution of the non-valent interaction energy to the conformation is less than the global conformation by (0.7) kcal/mol, and the contribution of the electrostatic interaction energy (1.8) kcal/mol is higher. The contribution of the torsional interaction energy is less (0.7) kcal/mol.

In general, the contribution of the interactions of Tyr1 with other amino acid residues to the stabilization of the conformation is (-8.3) kcal/mol, the contribution of the interaction of Gly2 with other amino acid residues is (-3.7) kcal/mol, Phe3 (Asn4-Ala5) The share given by (-3.2) kcal/mol, the share given by Asn4 with Ala5 is (-1.5) kcal/mol (Table 3).

The relative energy of the $B_3RB_1R_{11}R_2$ conformation of efef shape is (2.5) kcal/mol. Non-valent interaction energy (-15.1) kcal/mol, electrostatic interaction energy (3.4) kcal/mol, and torsional interaction energy (2.8) kcal/mol contribute to the stabilization of this conformation. Conformation stabilization is contributed by Tyr1-Gly2 (-0.9) kcal/mol, Tyr1-Phe3 (-7.1) kcal/mol, Tyr1-Asn4 (-1.1) kcal/mol, Tyr1-Asn5 (-2.7) kcal/mol, Phe3-Asn4 (-1.5) kcal/mol, Phe3-Ala5 (-3.1) kcal/mol, Asn4-Ala5 (-1.5) kcal/mol and stabilizes it.

The study of the spatial structure of the serorphin molecule shows that the molecule has such a set of spatial structures that it can perform various biological functions and interact with various receptor molecules. The results obtained from the study of the spatial structure of the serorphin molecule can be used to propose the synthesis of its artificial analogues that perform certain functions.

The relative energy of the fully rotated backbone $B_2PR_2R_{31}R_2$ is (2.6) kcal/mol. Conformation stabilization is contributed by non-valent interaction energy (-14.3) kcal/mol, electrostatic interaction energy (3.5) kcal/mol, and torsional interaction energy (2.0) kcal/mol. In this conformation, the share of the effective energy with the amino acid residues following the conformation of Tyr1 to the total energy is (-10.5) kcal/mol, and the share of the impact energy with the amino acid residues following the conformation of Gly2 is (-2.6) kcal/mol. . The effective energy of Phe3 with Asn4-Ala5 is (-1.1) kcal/mol.

The $B_2PB_1R_{31}R_2$ conformation differs from the previous conformation due to the conformation of Phe3. Therefore, the relative energy of this conformation was (2.7) kcal/mol.

The interaction energy of Tyr1 with the following tetrapeptide fragment is up to (-9.0) kcal/mol, the interaction energy of Gly2 with the following tripeptide fragment is up to (-4.5) kcal/mol, Asn4-Ala5 (-1.2) kcal/mol and stabilizes the conformation by contributing up to.

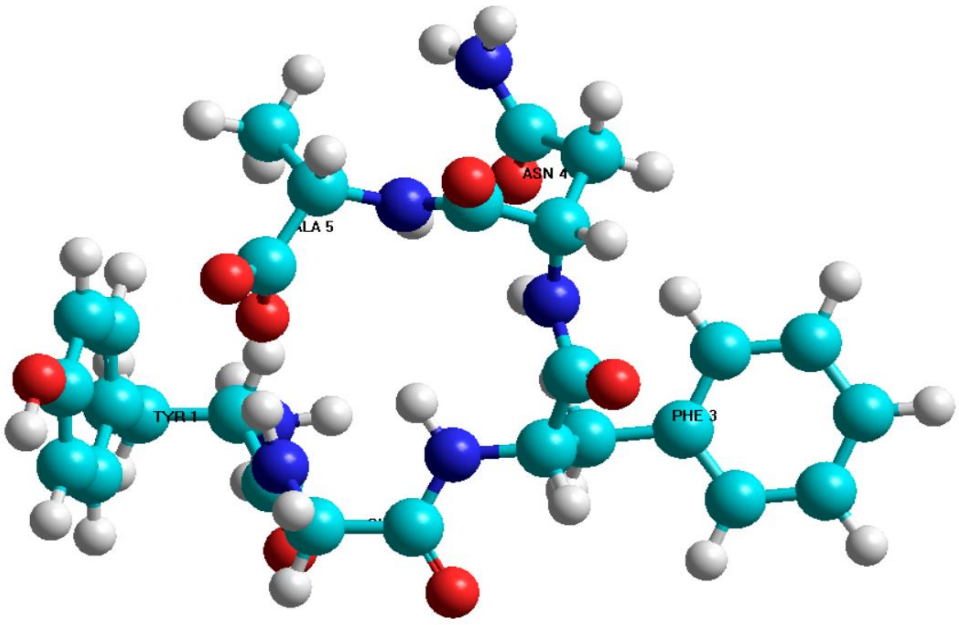

Figure 1. Spatial structure of the conformation $B_2LR_2R_{11}R_2$ of the serorphin molecule with a relative energy of 0 kcal/mol

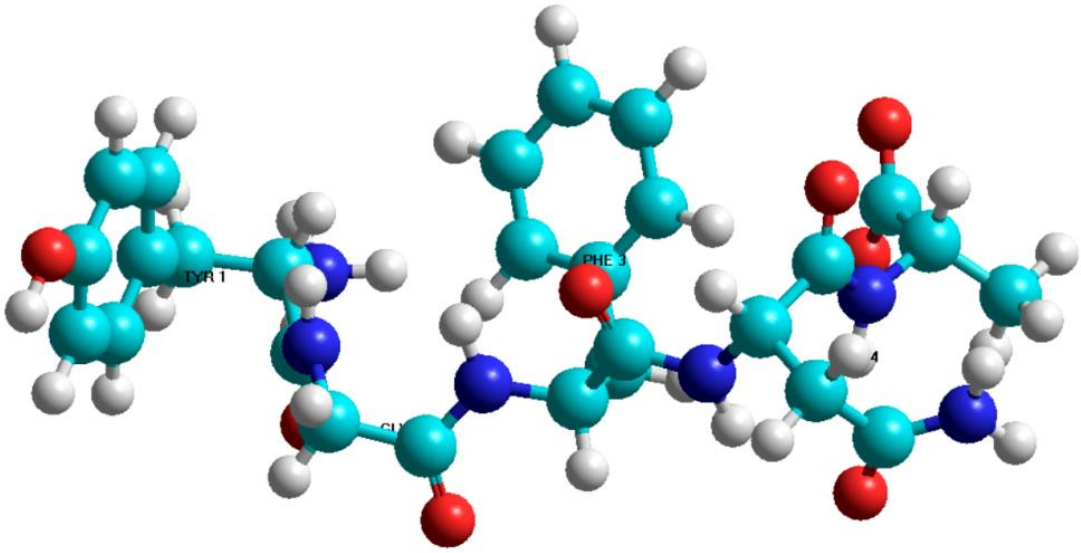

Figure 2. Spatial structure of the conformation $B_2LB_1R_{11}R_2$ of the serorphin molecule with a relative energy of 1.7 kcal/mol

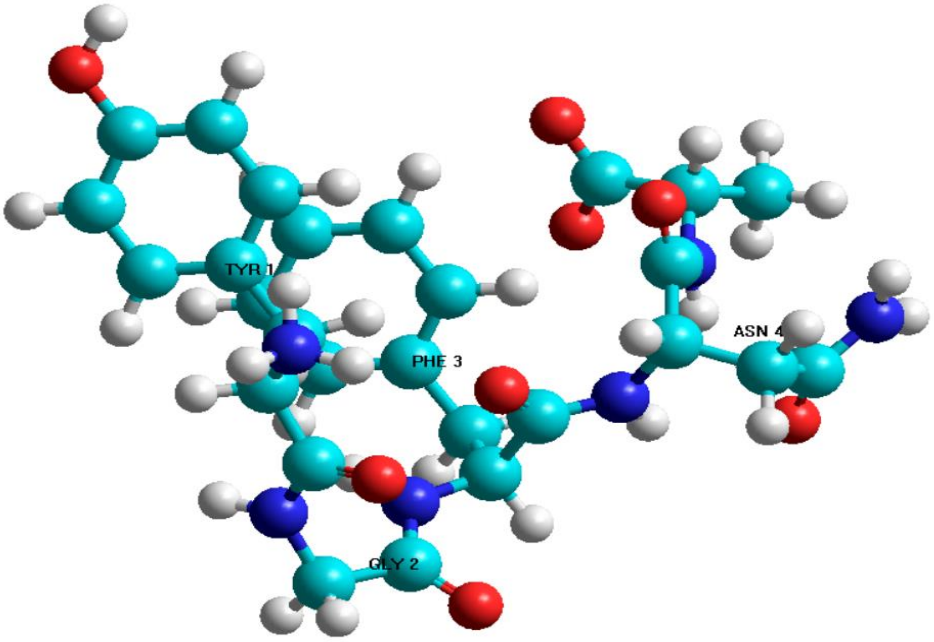

Figure 3. Spatial structure of the conformation $B_3RB_1R_{11}R_2$ of the serorphin molecule with a relative energy of 2.5 kcal/mol

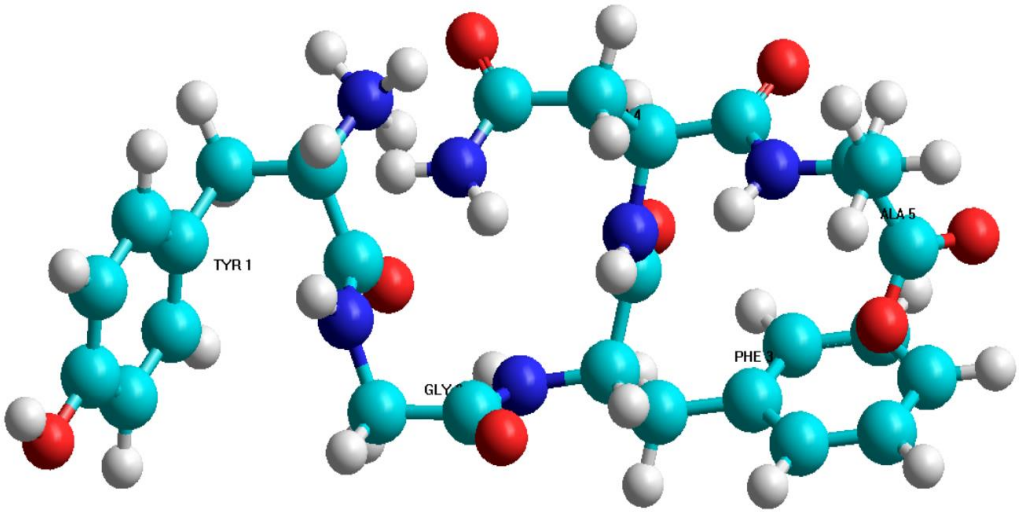

Figure 4. Spatial structure of the conformation $B_2PR_2R_{31}R_2$ of the serorphin molecule with a relative energy of 2.6 kcal/mol

Conclusion

The set of possible conformations of the serorphin molecule was studied by the method of theoretical conformational analysis and it was shown that the spatial structure of the molecule is represented by eight low-energy conformations.

It was determined that the N-side dipeptide fragment of the serorphin molecule is in labile conformation possibilities, and the C-side tripeptide fragment is in a rigid conformation.

The roles of different interaction energies and interactions between amino acid residues in the formation of low-energy conformations of the serorphin molecule were determined.

The values of the dihedral rotation angles of the low-energy conformations of the serorphin molecule have been determined.

It has been shown that the molecule has such a set of spatial structures that it can perform various biological functions and interact with various receptor molecules. The results obtained from the study of the spatial structure of the serorphin molecule can be used to propose the synthesis of its artificial analogues that perform certain functions.

REFERENCES

1. Chesnokova E.A., Sarycheva N.Y., Dubynin V.A., Kamensky A.A. Food-Derived Opioid Peptidesand Their Neurological Impact. Advances in Physiological Sciences, Vol.46, №1, p.22-46, 2015 (In Russ.).
2. Sokolov O.Yu., Kost N.V., Andreeva O.O., Korneeva E.V., Meshavkin V.K., Tarakanova Yu.N., Dadayan A.K., Zolotarev Yu.A., Grachev S.A., Mikheeva I.G., Zozulya A.A. The possible role of casomorphins in pathogenesis of autism. Psixiatriya. Vol.46, №3, p.29-35, 2010. (In Russ.).
3. Sienkiewiez-Szlapka E., Jarmolowska B., Krawczuk S., Kostyara E. Contents of agonistic and antagonistic opioid peptides in different cheese varieties. Int Dairy J. Vol.19, №4, p.258-263, 2009.
4. Meisel H., FitzGerald R.J. Opioid peptides encryptrd in intact milk protein sequences. British J.Nutrition.Vol.84, p.27-31,2000.
5. Akhmedov N.A. Teoretical conformation analysis of β-cazomorphin, valmuceptin and morphiceptin molecules. Molecular. Biol.,Vol.23, p.240-240,1989 (In Russ.).
6. Akhmedov N.A., Godjaev N.M., Suleymanova E.V., Popov E.M. Structural organization of the [Met] encephalin and endorphins molecules, Vol.16, p. 649-667,1990 (In Russ.).
7. Akhmedov N.A., Agayeva L.N., Ismailova L.I., Godjaev N.M. The spatial structure of
8. the cardio active peptides. Current Topics in Peptide and Protein Research, Vol.11, p. 87-93, 2010.
9. Gadjieva Sh.N., Akhmedov N.A., Masimov E.A., Godjaev N.M. Spatial Structure of Thr-Pro-Ala-Glu-Asp-Phe-Met-Arg-Phe-NH_2.Biophysics, Vol.58, p.587-590,2013(In Russ.).
10. Akhmedov N.A., Ismailova L.I., Abbasli R.M. et al. Spatial Structure of Octarphin molecule. IOSR J. Applied Physics (IOSR-JAP).Vol.8, p.66-70,2016.
11. Akhmedov N.A., Abbasli R.M., Agayeva L.N., Ismailova L.I. Three-dimensional structure of exorpin B5 molecule.Conference proceedings Modern Trends In Physics. p.201-104,2019.
12. Akhmedov N.A., Agayeva L.N., Akverdieva G.A., Abbasli R.M., Ismailova L.İ. Spatial structure of the ACTH-(6-9)-PGP molecule. J.Chem.Soc.Pak.,Vol. 43. №5, p.500-504, 2021.
13. Agayeva L.N, Abdinova A.A, Akhmedova S.R., .Akhmedov N.A .Spatial Structure of the ACTH-(7-10) Molecule. Biophyics, Vol.66, No4, p.531-534,2021.
14. Agaeva L.N, Abdinova A.A., Akhmedova S.R., Akhmedov N.F., and Akhmedov N.A. Spatial structure of Soymorphin-6 Molecule. Biophyics, Vol.68, № 6 ,p.1122-1127, 2023.
15. Ismailova L.I., Akverdieva G.A., Demukhamedova S.D., Akhmedov N.A. Molecular modelling of Pro-Gly gliproline and its complexes. Moscow University Physics Bulletin.Vol. 78, № 5, p. 668-680, 2023.
16. IUPAC-IUB. Quantities, Units and Symbols in Physical Chemistry, Blackwell Scientific, Oxford, 1993.
17. Maksumov I.S., Ismailova L.I., Godjaev N.M. Program for semi-empirical calculation of conformations of molecular complexes on a computer. J. Struk. Chemistry, Vol. 24, p.147-148, 1983.

JOURNAL OF BAKU ENGINEERING UNIVERSITY - PHYSICS
2023. Volume 7, Number 2 *Pages 100-109*

PACS: *14.60. Lm, 14.60. St, 12.15.-y, 13.38.-b, 14.70. Fm, 97.10. Ld, 91.25.-r*
UOT:*530.1:51-72*

DOES EXTERNAL MAGNETIC FIELD AFFECT WEAK INTERACTION IN SCATTERING OF ELECTRON NEUTRINO BY ELECTRON?

VALI A. HUSEYNOV[1,2,3,4*], RASMIYYA E. GASIMOVA[5,6], RANIA ROUGGANI MERZOUKI[3],

[1] *Laboratory for Physics of Cosmic Ray Sources, Institute of Physics, Baku, Azerbaijan,* vgusseinov@yahoo.com;

[2] *Department of Engineering Physics and Electronics, Azerbaijan Technical University, Baku, Azerbaijan;*

[3] *Department of Physics, Baku Engineering University, Khirdalan, Azerbaijan;*

[4] *Department of Physics and its Teaching Methods, Sumgayit State University, Sumgayit, Azerbaijan;*

[5] *Department of Theoretical Astrophysics and Cosmology, Shamakhy Astrophysical Observatory, Baku, Azerbaijan,* gasimovar@yahoo.co.uk;

[6] *Department of General Physics, Azerbaijan State Pedagogical University, Baku, Azerbaijan.*

* Corresponding Author

ABSTRACT

We investigate the scattering of a sufficiently low-energy electron neutrino by the transversely polarized ultra-relativistic electron in a constant homogeneous magnetic field with a strength much less than the Schwinger field strength in the framework of the Weinberg-Salam electroweak interactions theory. We clarify whether the external magnetic field with a strength much less than the Schwinger field strength affects weak interaction in the scattering of a relic electron neutrino by the electron of the energy $\sim 10^2 GeV$. It is determined that the weak interaction that is involved in the process $\nu_e e^- \to \nu_e' e^{-\prime}$ is unaffected by the magnetic fields whose strengths are much less than the Schwinger field strength. We analyze the importance of the propagator effects and calculate the matrix element and amplitude of the process.

Keywords: neutrinos, electroweak interactions, intermediate bosons, W bosons, stellar magnetic fields, terrestrial magnetic fields

XARİCİ MAQNİT SAHƏSİ ELEKTRON NEYTRİNOSUNUN ELEKTRONDAN SƏPİLMƏSİNDƏ ZƏİF QARŞILIQLI TƏSİRƏ TƏSİR EDİRMİ?

XÜLASƏ

Biz Weinberg-Salam elektrozəif qarşılıqlı təsir nəzəriyyəsi çərçivəsində induksiyasının qiyməti Şvinqer sahə qiymətindən çox-çox kiçik olan sabit bircins maqnit sahəsində kifayət qədər aşağı enerjili elektron neytrinosunun eninə polyarlaşmış ultra-relativistik elektronlardan səpilməsini araşdırmışıq. İnduksiyasının qiyməti Schwinger sahə qiymətindən çox-çox kiçik olan xarici maqnit sahəsinin relikt elektron neytrinosunun ~10^2 GeV enerjili elektrondan səpilməsində zəif qarşılıqlı təsirə təsir edib-etmədiyini aydınlaşdırmışıq. Müəyyən etmişik ki, elektron neytrinosu-elektron səpilmə prosesində iştirak edən zəif qarşılıqlı təsir, induksiyasının qiyməti Şvinqer sahə qiymətindən çox-çox kiçik olan maqnit sahələri tərəfindən təsirə məruz qalmır. Biz propaqator effektlərinin rolunu təhlil etmiş və prosesin matris elementini və amplitudunu hesablamışıq.

Açar sözlər: neytrinolar, elektrozəif qarşılıqlı təsirlər, aralıq bozonlar, W bozonları, ulduz maqnit sahələri, yer maqnit sahələri.

ВЛИЯЕТ ЛИ ВНЕШНЕЕ МАГНИТНОЕ ПОЛЕ НА СЛАБОЕ ВЗАИМОДЕЙСТВИЕ ПРИ РАССЕЯНИИ ЭЛЕКТРОННОГО НЕЙТРИНО НА ЭЛЕКТРОНЕ?

АННОТАЦИЯ

В рамках теории электрослабого взаимодействия Вайнберга-Салама нами исследовано рассеяние электронного нейтрино достаточно низкой энергии на поперечно-поляризованных ультрарелятивистских электронах в постоянном однородном магнитном поле с величиной индукции, значительно меньшей, чем величина поля Швингера. Мы выяснили, что влияет ли внешнее магнитное поле, величина индукции которого значительно меньше величины поля Швингера, на слабое взаимодействие при рассеянии

реликтового электронного нейтрино на электроне с энергией ~10^2 ГэВ. Мы обнаружили, что магнитные поля, величина индукции которых значительно меньше величины поля Швингера, не влияют на слабое взаимодействие, участвующее в процессе рассеяния электронного нейтрино на электроне. Мы проанализировали роль эффектов пропагатора и рассчитали матричный элемент и амплитуду процесса.

Ключевые слова: нейтрино, электрослабые взаимодействия, промежуточные бозоны, W-бозоны, звездные магнитные поля, земные магнитные поля.

1. INTRODUCTION

In this work we consider the scattering of a sufficiently low-energy electron neutrino by the transversely polarized ultra-relativistic electron

$$\nu_e + e^- \to \nu_e' + e^{-\prime}, \tag{1}$$

in a constant homogeneous magnetic field with the strength

$$B \ll B_0 \tag{2}$$

in the framework of the Weinberg-Salam electroweak interactions theory where ν_e (ν_e') is the electron neutrino in the initial (final) state, $B_0 = m_e^2/e \cong 4.414 \times 10^{13} G$ is the Schwinger field strength in the system of units $c = \hbar = 1$. Both a weak charged current (W-boson) and a weak neutral current (Z-boson) contribute to the process (1) [1] and the related Feynman diagrams of the process in an external magnetic field are given by the Fig. 1 and Fig. 2, respectively.

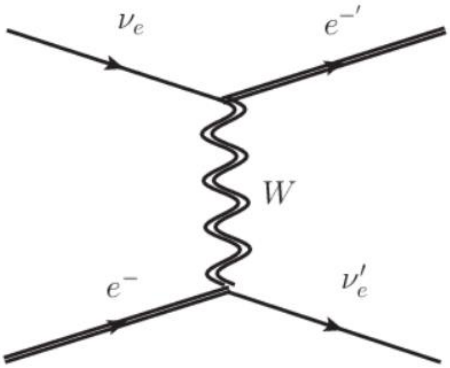

Figure 1. The Feynman diagram describing the process $\nu_e e^- \to \nu_e' e^{-\prime}$ proceeding at the expense of a weak charged current.

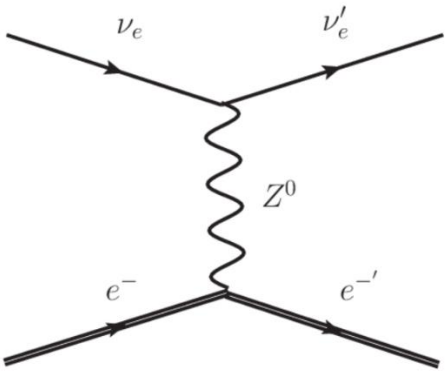

Figure 2. The Feynman diagram describing the process $\nu_e e^- \to \nu_e' e^{-\prime}$ proceeding at the expense of a weak neutral current.

When we say a sufficiently low-energy incident neutrino, we mean the neutrino whose energy is in the range

$$\omega_{min} \ll \omega \ll m_e, \tag{3}$$

where $\omega_{min} = eB/p_\perp$ is the lowest boundary of the energy of the incident neutrino, $p_\perp = (2eBn)^{1/2}$ and n are the transverse momentum and the number of the Landau energy level of the electron in the initial state, respectively. A relic neutrino whose energy is $\omega \cong 1.68 \times 10^{-4} eV$ is a typical example for the sufficiently low-energy neutrino.

We also assume that the energy of the electron in the initial state is $\sim 10^2 GeV$.

Calculation of some physical quantities like the differential probability, cross section, energy-momentum loss etc that are characteristic for the process (1) is connected with calculation of the matrix element or amplitude of the corresponding process. As we indicated both a weak charged current (W-boson) and a weak neutral current (Z-boson) contribute to the process (1). Since we consider the process $\nu_e e^- \to \nu_e' e^{-\prime}$ in an external magnetic field, at the first glance, it seems to us that the rate of this process would be enhanced due to the off-shell charged vector boson. The two natural questions arise: 1) whether the W-boson, the Z-boson and, in general, the weak interaction that is involved in the process (1) is affected by the magnetic field of the strength (2); 2) do the W-boson propagator effect and the Z-boson propagator effect contribute to the relic electron neutrino-electron scattering process at energies $\sim 10^2 GeV$ of the electron in the initial state. The purpose of this work is to clarify the above-mentioned two questions. For this purpose, we investigate the influence of the external magnetic field on the weak interaction that is involved in the process (1), clarify the importance of the propagator effects and calculate the matrix element and amplitude of the process (1).

2. PHYSICAL CONDITIONS

We assume that electrons in the initial and final states are ultra-relativistic

$$\varepsilon^2 \gg m_e^2, \varepsilon'^2 \gg m_e^2 \tag{4}$$

where $\varepsilon = \gamma m_e$, $\gamma = \sqrt{1 + 2fn + (p_z/m_e)^2}$, p_z and n are the energy, relativistic factor, z-component of the momentum and the number of the Landau energy level belonging to the electron in the initial state, respectively. The primed quantities $\varepsilon' = \gamma' m_e$, $\gamma' = \sqrt{1 + 2fn' + (p_z'/m_e)^2}$, p_z' and n' belong to the electron in the final state. f is the dimensionless field parameter characterizing the external magnetic field $f = B/B_0$ where B is the magnitude of the magnetic field vector $\vec{B}$ that is directed along the z-axis and. According to (2)

$$f \ll 1. \tag{5}$$

We also assume that electrons in the initial and final states possess large transverse momenta

$$p_\perp = (2eBn)^{1/2} = m_e(2fn)^{1/2} \gg m_e, \tag{6}$$

$$p_\perp' = (2eBn')^{1/2} = m_e(2fn')^{1/2} \gg m_e. \tag{7}$$

The assumptions (4)-(7) mean that the main contribution to the differential probability of the process (1) comes from the electron states occupying high Landau levels (n, $n' \gg 1$). In this case motion of the electrons in the initial and final states are semiclassical.

We consider the case when the longitudinal momentum of the electrons in the initial state is zero: $p_z = 0$.

Let a sufficiently low-energy incident neutrino fly along the z-axis (along the magnetic field direction). According to (3) the energy of the incident electron neutrino satisfies the condition

$$\frac{f}{\sqrt{\gamma^2-1}} \ll \frac{\omega}{m_e} \ll 1 \tag{8}$$

where $\omega_{min} = eB/p_\perp$.

Experimental observations on neutrino oscillations [2, 3] confirm that a neutrino has a non-zero mass. The latest results of the KATRIN experiment show that $m_\nu < 0.8\, eVc^{-2}$ at 90% confidence level [4]. However, the lowest boundary of the neutrino mass has not been experimentally determined by the KATRIN and other collaborations yet. Here we assume that a neutrino, in particular a relic electron neutrino possesses sufficiently small mass (this case is not excluded). Therefore, we consider a massless neutrino model [1] that is justified for ultra-relativistic neutrinos ($\omega, \omega' \gg m_\nu$ where m_ν is the neutrino mass and ω' is the energy of the scattered neutrino). In the considered physical conditions we can neglect the mass of a neutrino and we can apply the massless neutrino model.

The above indicated conditions and restrictions mean that the differential probability of the process will depend on two parameters [5]: the field parameter

$$\chi = \frac{e}{m_e^3}\left[-\left(F_{\mu\nu}p^\nu\right)^2\right]^{1/2} = \frac{B}{B_0}\frac{p_\perp}{m_e} = [f^2(\gamma^2-1)]^{1/2} \tag{9}$$

and the kinematical parameter

$$\kappa = \frac{2\omega\varepsilon}{m_e^2} = \frac{2kp}{m_e^2} \tag{10}$$

where $F_{\mu\nu} = \partial_\mu A_\nu - \partial_\nu A_\mu$ is the external field tensor of a magnetic type: $F_{\mu\nu}F^{\mu\nu} > 0$, $F^{\mu\nu}\tilde{F}_{\mu\nu} = 0$, $\tilde{F}_{\mu\nu} = (1/2)\varepsilon_{\mu\nu\alpha\beta}F^{\alpha\beta}$ is the dual counterpart tensor corresponding to $F_{\mu\nu}$.

The analyses show that the influence of the external magnetic field on the low-energy neutrino-electron scattering is determined by the parameter [6]

$$\eta = \frac{\chi}{\kappa} = \frac{1}{2}\frac{B}{B_0}\frac{m_e}{\omega}. \tag{11}$$

When the parameter $\eta \gtrsim 1$, the field effects become essentially. To achieve $\eta \gtrsim 1$ for the relic electron neutrino-electron scattering B is to satisfy the condition

$$2.91 \times 10^4\, G \lesssim B \ll 4.41 \times 10^{13} G. \tag{12}$$

3. THE MATRIX ELEMENT OF THE SCATTERING OF AN ELECTRON NEUTRINO BY AN ELECTRON IN A MAGNETIC FIELD

The matrix element of the process $\nu_e e^- \to \nu_e' e^{-\prime}$ in a magnetic field is given by

$$M = M_W + M_Z \tag{13}$$

where

$$M_W = \frac{g^2}{8}\int\left[\overline{\psi}_{e'}(x')O_\alpha\psi_\nu(x')\right]\left[\overline{\psi}_{\nu'}(x)O_\beta\psi_e(x)\right]G_{WB}^{\alpha\beta}(x-x')d^4xd^4x' \quad (14)$$

is the matrix element corresponding to the Feynman diagram of the $\nu_e e^- \to \nu_e' e^{-\prime}$ process proceeding only at the expense of the W-boson exchange (Fig. 1), $G_{WB}^{\alpha\beta}(x-x')$ corresponds to the W-boson propagator in an external constant magnetic field [5], $O_\alpha = \gamma_\alpha(1+\gamma^5)$, $q = k'-k$, γ^α are the Dirac matrices, $\gamma^5 = -i\gamma^0\gamma^1\gamma^2\gamma^3$ [1], $\psi_\nu(x') = (2\omega V)^{-1/2}u(k)exp(ikx')$ is the wave function of the incident neutrino possessing the four-momentum k and the energy ω, $\overline{\psi}_{\nu'}(x') = \psi_{\nu'}^{+}(x')\gamma^0$, $\psi_{\nu'}(x') = (2\omega' V)^{-1/2}u(k')exp(ik'x')$ is the wave function of the scattered neutrino possessing the four-momentum k' and energy ω', V is the normalization volume, $u(k)$ and $u(k')$ are the Dirac bispinors of the incident and scattered neutrinos, respectively, $\psi_e(x)$ ($\psi_{e'}(x)$) is the solution of the Dirac equation in a constant homogeneous external magnetic field for the electron in the initial (final) state, $\overline{\psi}_{e'}(x) = \psi_{e'}^{+}(x)\gamma^0$ (the electrons in the final state are described and denoted with the primed quantities), M_Z is the matrix element corresponding to the Feynman diagram of the $\nu_e e^- \to \nu_e' e^{-\prime}$ process proceeding only at the expense of the Z-boson exchange (Fig. 2) and it is given by

$$M_Z = \frac{g^2}{8\cos^2\theta_w}\int \mathrm{N}_\alpha(x')\Lambda_{Z\beta}(x)G_Z^{\alpha\beta}(x-x')d^4xd^4x' \quad (15)$$

where

$$\mathrm{N}_\alpha(x') = \overline{\psi}_{\nu'}(x')O_\alpha\psi_\nu(x'), \quad (16)$$

$$\Lambda_{Z\beta}(x) = \overline{\psi}_{e'}(x)\gamma_\beta(g_V + g_A\gamma^5)\psi_e(x), \quad (17)$$

$$G_Z^{\alpha\beta}(x-x') = \int G_Z^{\alpha\beta}(q)e^{-iq(x-x')}\frac{d^4q}{(2\pi)^4}, \quad (18)$$

$$G_Z^{\alpha\beta}(q) = -\frac{g^{\alpha\beta}}{q^2-m_Z^2+i0} \quad (19)$$

is the Z-boson propagator, $g = e/\sin\theta_W$, θ_W is the Weinberg angle, $\sin^2\theta_W \cong 0.23$, $q = k'-k$ is the 4-momentum of an intermediate Z-boson, $g_V = -0.5 + 2\sin^2\theta_W$ and $g_A = -0.5$ [1].

We obtain the following result for the squared four-momentum $q = k'-k$ transferred

$$|q^2| = 2kk' \ll |q^2|_{max} \simeq 2\omega\varepsilon \ll m_Z^2. \quad (20)$$

Using this result and the formulae (18) and (19) we can write the following relation for the Z-boson propagator $G_Z^{\alpha\beta}(x-x')$:

$$G_Z^{\alpha\beta}(x-x') = \frac{g^{\alpha\beta}}{m_Z^2}\delta(x-x'). \quad (21)$$

Taking into account (21) and the known relation [1]

$$\frac{g^2}{8m_Z^2\cos^2\theta_W} = \frac{G_F}{\sqrt{2}} \quad (22)$$

in (15) we obtain the related matrix element in four-fermion approximation

$$M_Z = \frac{G_F}{\sqrt{2}}\int \mathrm{N}_\alpha(x)\Lambda_Z^\alpha(x)d^4x = 2\pi\delta(\varepsilon'+\omega'-\varepsilon-\omega)A_Z \quad (23)$$

where

$$\mathrm{N}_\alpha(x) = \overline{\psi}_{\nu'}(x) O_\alpha \psi_\nu(x)\,, \tag{24}$$

$$\Lambda_Z^\alpha(x) = \overline{\psi}_{e'}(x)\gamma^\alpha(g_V + g_A\gamma^5)\psi_e(x), \tag{25}$$

In the matrix element (23) A_Z is the amplitude of the elastic neutrino-electron scattering in four-fermion approximation

$$A_Z = \frac{\sqrt{2}G_F}{4V(\omega\omega')^{1/2}}[\overline{u}(k')\gamma_\alpha(1+\gamma^5)u(k)]j_Z^\alpha(\vec{q}) \tag{26}$$

where

$$j_Z^\alpha(\vec{q}) = \int\left[\overline{\psi}_{e'}(\vec{r})\gamma^\alpha(g_V + g_A\gamma^5)\psi_e(\vec{r})\right]e^{-i\vec{q}\vec{r}}d^3x \tag{27}$$

is the electron current and $d^3x = dx\,dy\,dz$.

4. INFLUENCE OF MAGNETIC FIELD ON WEAK INTERACTION IN NEUTRINO-ELECTRON SCATTERING PROCESS

Since we consider the process $\nu_e e^- \to \nu_e' e^{-\prime}$ in an external magnetic field, at the first glance it seems to us that the rate of this process would be enhanced due to the off-shell charged vector boson (Fig. 1). Let us analyze the influence of the external magnetic field on the off-shell W-boson participating in the process $\nu_e e^- \to \nu_e' e^{-\prime}$.

The typical electromagnetic time that is characteristic for the influence of the external magnetic field on the off-shell W-boson participating in the process $\nu_e e^- \to \nu_e' e^{-\prime}$ is determined by the period of revolution of the off-shell W-boson in an external magnetic field

$$T_w^{em} = \frac{2\pi m_W}{eB\sqrt{1-\frac{v^2}{c^2}}} = \frac{2\pi\varepsilon_W}{eB} = 2\pi\lambda_C\frac{\varepsilon_W}{m_e}\frac{B_0}{B} \tag{28}$$

where ε_W is the energy of the off-shell W-boson participating in the process $\nu_e e^- \to \nu_e' e^{-\prime}$.

It is obtained from (3) or (8) that the maximal value of ω_{min} can be $\omega_{min} \cong 10^{-1}\omega$. In case of a relic electron neutrino ($\omega \cong 1.68 \times 10^{-4} eV$) we have $\omega_{min} \cong 1.68 \times 10^{-5} eV$. If we consider electrons (in the initial state) with the energy of several hundred GeV (e.g., $\varepsilon \cong 550\ GeV$) and use the condition (3) or (8), we obtain the following restriction for the magnetic field

$$f \leq 3.55 \times 10^{-5} \tag{29}$$

or

$$B \leq 1.57 \times 10^9 G. \tag{30}$$

The conditions (12) and (30) can be combined and written as

$$2.91 \times 10^4\ G \leq B \leq 1.57 \times 10^9 G. \tag{31}$$

Taking into account the range for the magnetic field strength determined by the condition (31) and using the formula (28) we obtain the following estimation for the typical electromagnetic time that is characteristic for the influence of the external magnetic field on the off-shell W-boson participating in the process $\nu_e e^- \to \nu_e' e^{-\prime}$

$$10^{-11} s \lesssim T_w^{em} \lesssim 10^{-6} s \tag{32}$$

The maximum energy $\Delta\varepsilon_W$ transferred from the electrons to the neutrinos via the intermediate (off-shell) W-boson (or Z-boson) is in order of the energy of the electron in the initial state: $\Delta\varepsilon_W \sim \varepsilon \sim 10^{11}\ eV$. Using the Heisenberg uncertainty relation for the energy gap $\Delta\varepsilon_W$ and the life-time $\Delta\tau_W$ of the off-shell W-boson in this energy gap we obtain $\Delta\tau_W \sim 1/2\Delta\varepsilon_W \sim 10^{-27}\ s$. If we compare the estimated value for $\Delta\tau_W$ with the characteristic electromagnetic time range (32), we see that $\Delta\tau_W \ll T_{em}$. It means that the magnetic field of the strength $2.91 \times 10^4\ G \leq B \leq 1.57 \times 10^9 G$ does not have time to influence on the weak interaction that is realized by the W-boson in the $\nu_e e^- \to \nu_e' e^{-\prime}$ process. In other words, not only the external magnetic field of the strength (31) but also the external magnetic field of the strength $B \ll B_0$ is not able to affect on the intermediate W-boson during the proceeding of the process (1): the intermediate (off-shell) W-boson does not feel the influence of the external magnetic field and it behaves itself so, as if the external magnetic field is absent. In this case the contribution of the intermediate W-boson can be calculated as in free case when the external magnetic field is absent.

Magnetic field effects on the weak interaction is essential if the magnetic field energy scale $\sqrt{eB}$ is in order of the mass of the W-boson (Z-boson) or more than the mass of the W-boson (Z-boson). However, in the considered case ($2.91 \times 10^4\ G \leq B \leq 1.57 \times 10^9 G$) the magnetic field energy scale is much smaller than the mass of the W-boson (Z-boson)

$$\sqrt{eB} = 0.24 \left(\frac{B}{10^{13}\ G}\right)^{1/2} MeV \ll m_W, m_Z. \tag{33}$$

Therefore, the weak interaction that is involved in the process (1) is unaffected by the magnetic field of the strength (31) and $B \ll B_0$.

However, the magnetic field affects the considered process by deforming the energy spectrum of the electron in both the initial and final state ($\varepsilon = m_e\sqrt{1 + 2fn + (p_z/m_e)^2}$ and $\varepsilon' = m_e\sqrt{1 + 2fn' + (p_z'/m_e)^2}$), by polarizing the spins of the electrons and by changing the phase space of the electron in the final state. Unlike the free case (when an external magnetic field is absent), the presence of a magnetic field leads to the change of the integration over the phase space of the final electron from the classical case to the quantum case

$$\frac{1}{4\pi^3}\int d\Omega \int p'^2\, dp' \to \frac{eB}{2\pi^2}\sum_{n=0}^{n_{max}} g_n \int dp_z' \tag{34}$$

where p_z' is the third component of the momentum of the electron in the final state, $d\Omega$ is the solid angle element, g_n is the degeneracy of the Landau levels of the electron: $g_n = 2$ for the $n > 0$ states and $g_n = 1$ for the $n = 0$ states (ground Landau level).

5. MATRIX ELEMENT OF SCATTERING OF AN ELECTRON NEUTRINO BY AN ELECTRON VIA A CHARGED VECTOR BOSON IN A MAGNETIC FIELD

Thus, since the magnetic field of the strength $2.91 \times 10^4\ G \leq B \leq 1.57 \times 10^9 G$ does not affect the intermediate (off-shell) W-boson participating in the $\nu_e e^- \to \nu_e' e^{-\prime}$ process, in the matrix element (14) we can replace $G_{WB}^{\alpha\beta}(x - x')$ with the $G_W^{\alpha\beta}(x - x')$ for the free case:

$$G_{WB}^{\alpha\beta}(x - x') \to G_W^{\alpha\beta}(x - x') = \int G_W^{\alpha\beta}(q) e^{-iq(x-x')} \frac{d^4q}{(2\pi)^4}, \tag{35}$$

where $G_W^{\alpha\beta}(q)$ is the W-boson propagator,

$$G_W^{\alpha\beta}(q) = -\frac{g^{\alpha\beta}}{q^2 - m_W^2 + i0}. \tag{36}$$

Taking the relation (35) into account in (14) the matrix element of the $\nu_e e^- \to \nu_e' e^{-\prime}$ process proceeding only at the expense of the W-boson exchange is given by

$$M_W = \frac{g^2}{8}\int\left[\overline{\psi}_{e'}(x')O_\alpha\psi_\nu(x')\right]\left[\overline{\psi}_{\nu'}(x)O_\beta\psi_e(x)\right]G_W^{\alpha\beta}(x-x')d^4xd^4x' \tag{37}$$

Let us analyze the contribution of the intermediate W-boson to the $\nu_e e^- \to \nu_e' e^{-\prime}$ process. The magnitude of the squared momentum transfer is

$$q^2 = (p'-k)^2 = m_e^2 - 2\omega\varepsilon'(1-\cos\alpha) \tag{38}$$

where $p'(\varepsilon')$ is the four-momentum (energy) of an electron in the final state, k is the four-momentum of the incident electron neutrino, α is the angle between the electron (in the final state) momentum vector $\vec{p}'$ and an electron neutrino momentum vector $\vec{k}$. As we indicated, we consider the neutrinos whose energy is in the range $1.68\times10^{-5}\ eV \ll \omega \ll 5.11\times10^{5}\ eV$ and the electrons of the energy $\varepsilon \sim 10^2\ GeV$. The calculations show that in this case $\cos\alpha \ll 1$

$$2\omega\varepsilon'(1-\cos\alpha) \approx 2\omega\varepsilon' \gg m_e^2 \tag{39}$$

and

$$|q^2| \approx 2\omega\varepsilon' \ll m_W^2 \tag{40}$$

where m_W is the W-boson mass.

So, the results (35)-(37) and (40) confirm that the contribution of an intermediate W-boson can be neglected in both the presence and absence of an external magnetic field and the four-fermion (low-energetic) approximation of the Weinberg-Salam electroweak interaction theory (Fig. 3) can be applied. The result (40) and the formulae (35) and (36) enable us to write the following relation for the W-boson propagator $G_W^{\alpha\beta}(x-x')$:

$$G_W^{\alpha\beta}(x-x') = \frac{g^{\alpha\beta}}{m_W^2}\delta(x-x'). \tag{41}$$

Using the relation (41) and the Fierz identity [1] we can write the matrix element (37) in a simpler form

$$M_W = \frac{G_F}{\sqrt{2}}\int \mathrm{N}_\alpha(x)\Lambda_W^\alpha(x)d^4x = 2\pi\delta(\varepsilon'+\omega'-\varepsilon-\omega)A_W \tag{42}$$

where

$$\Lambda_W^\alpha(x) = \overline{\psi}_{e'}(x)\gamma^\alpha(1+\gamma^5)\psi_e(x), \tag{43}$$

A_W is the amplitude of the $\nu_e e^- \to \nu_e' e^{-\prime}$ process proceeding only at the expense of the W-boson exchange in four-fermion approximation

$$A_W = \frac{\sqrt{2}G_F}{4V(\omega\omega')^{1/2}}[\overline{u}(k')\gamma^\alpha(1+\gamma^5)u(k)]j_W^\alpha(\vec{q}), \tag{44}$$

$$j_W^\alpha(\vec{q}) = \int\left[\overline{\psi}_{e'}(\vec{r})\gamma^\alpha(1+\gamma^5)\psi_e(\vec{r})\right]e^{-i\vec{q}\vec{r}}d^3x \tag{45}$$

and $\mathrm{N}_\alpha(x)$ is the same as (24).

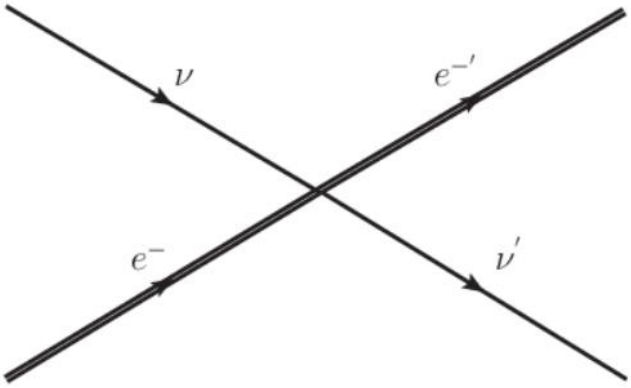

Figure 3. The Feynman diagram of the $\nu e^- \to \nu' e^{-\prime}$ process in the four-fermion (low-energetic) approximation.

6. RESULTANT MATRIX ELEMENT OF SCATTERING OF ELECTRON NEUTRINO BY ELECTRON IN MAGNETIC FIELD

So, taking into account (23) and (42) in (13) we obtain the final expression for the matrix element of the process $\nu_e e^- \to \nu_e' e^{-\prime}$ in the four-fermion (low-energetic) approximation of the Weinberg-Salam electroweak interaction theory

$$M = \frac{G_F}{\sqrt{2}} \int \mathrm{N}_\alpha(x) \Lambda^\alpha_{WZ}(x) d^4x = 2\pi\delta(\varepsilon' + \omega' - \varepsilon - \omega) A_{WZ} \tag{46}$$

where

$$\Lambda^\alpha_{WZ}(x) = \Lambda^\alpha_W + \Lambda^\alpha_Z = \overline{\psi}_{e'}(x)\gamma^\alpha(g_V' + g_A'\gamma^5)\psi_e(x), \tag{47}$$

A_{WZ} is the amplitude of the process $\nu_e e^- \to \nu_e' e^{-\prime}$ in the four-fermion approximation

$$A_{WZ} = A_W + A_Z = \frac{\sqrt{2}G_F}{4V(\omega\omega')^{1/2}} [\overline{u}(k')\gamma_\alpha(1+\gamma^5)u(k)] j^\alpha_{WZ}(\vec{q}), \tag{48}$$

$$j^\alpha_{WZ}(\vec{q}) = j^\alpha_W(\vec{q}) + j^\alpha_Z(\vec{q}) = \int \left[\overline{\psi}_{e'}(\vec{r})\gamma^\alpha(g_V' + g_A'\gamma^5)\psi_e(\vec{r})\right] e^{-i\vec{q}\vec{r}} d^3x, \tag{49}$$

$$g_V' = g_V + 1 = 0.5 + 2\sin^2\theta_W, \tag{50}$$

$$g_A' = g_A + 1 = 0.5. \tag{51}$$

CONCLUSION

For the magnetic fields in the range $2.91 \times 10^4\, G \le B \le 1.57 \times 10^9 G$ and even for the magnetic fields $B \ll B_0$ the magnetic field energy scale is much smaller than the mass of the W-boson (Z-boson). Therefore, the weak interaction that is involved in the process $\nu_e e^- \to \nu_e' e^{-\prime}$ is unaffected by the magnetic field of the strength $2.91 \times 10^4\, G \le B \le 1.57 \times 10^9 G$ and $B \ll B_0$.

It is determined that not only the external magnetic field of the strength $2.91 \times 10^4\, G \le B \le 1.57 \times 10^9 G$ but also the external magnetic field of the strength $B \ll B_0$ is not able to affect on the intermediate W-boson during the proceeding of the process $\nu_e e^- \to \nu_e' e^{-\prime}$: the intermediate (off-shell) W-boson does not feel the influence of the external magnetic field and it behaves itself so, as if the external magnetic field is absent. In this case the contribution of the intermediate W-boson can be calculated as in free case when the external magnetic

field is absent. It is substantiated that in the considered physical conditions the four-fermion (low-energetic) approximation of the Weinberg-Salam electroweak interaction theory can be applied to the $\nu_e e^- \to \nu_e' e^{-\prime}$ process in an external magnetic field. The obtained formulae for the matrix element and amplitude can be used in calculation of the differential probability, cross-section, energy-momentum loss and other physical quantities for the $\nu_e e^- \to \nu_e' e^{-\prime}$ process in an external magnetic field.

REFERENCES

1. L. B. Okun. *Leptons and Quarks*, North Holland, Amsterdam, 1984 (republished by Nauka, Moscow, 1990).
2. Y. Fukuda et al. (Super-Kamiokande Collaboration), Phys. Rev. Lett. 81, 1562, 1998.
3. Q. R. Ahmad et al. (SNO Collaboration). Phys. Rev. Lett. 89, 011301, 2002.
4. M. Aker et al. (KATRIN Collaboration). Nature Physics. 18, 160-166, 2022.
5. I. M. Ternov, V. Ch. Zhukovskii, and A. V. Borisov. *Quantum Prcesses in Strong External Fields*. Mosk. Gos. Univ., Moscow, 1989.
6. V. A. Guseinov, I. G. Jafarov, and R. E. Gasimova. Phys. Rev. D, v.75, No8, 073021, 2007.

JOURNAL OF BAKU ENGINEERING UNIVERSITY - PHYSICS

2023. Volume 7, Number 2 ***Pages 110-115***

PASC: 61.46.-w
UOT:539.216

"INVESTIGATION OF POLYMER COMPOSITES BY IMPEDANCE SPECTROSCOPY METHOD"

NARGIZ MEHDIYEVA

Baku Engineering University

Khirdalan city, Hasan Aliyev str

nmehdiyeva@beu.edu.az

ABSTRACT

The purpose of the work is to acquire HDPE-PKR-3M composite materials and investigate them using impedance spectroscopy. This method determines the complex impedance over a wide range of frequencies and analyzes the obtained sample with equivalent circuits consisting of ideal resistors, capacitors, and inductive elements, all having the same frequency dependence. The impedance spectroscopy provides a spectrum for heterogeneous systems, differentiating electrically heterogeneous regions based on dielectric permittivity and conductivity in the Nyquist diagram (relationship of real and imaginary parts of impedance, Z"=f(Z')). This diagram yields a multicomponent spectrum for regions with varying dielectric properties, such as ideal resistors, capacitors, and inductive elements. On the other hand, homogenous regions in the electric domain, which exhibit a characteristic semicircle, can be analyzed with impedance spectroscopy. Additionally, any factor influencing the impedance of the sample-electrode system can be studied using impedance spectroscopy.

The article explores the authenticity of the real and imaginary components of impedance, as well as the phase shift (φ), for HDPE+5% and HDPE+10% PKR-3M composite samples in relation to the external electric field intensity (23:10^6 Hs). Additionally, a Nyquist diagram has been constructed based on the changes in intensity. The studied samples were obtained using the hot pressing method.

KEYWORDS: 1-high-density polyethylene, 2-polymer composite, 3-impedance, 4-spectroscopy, 5-piezoelectric ceramics, 6-Nyquist diagram

"ПРОВЕДЕНИЕ ИССЛЕДОВАНИЙ ПОЛИМЕРНЫХ КОМПОЗИТОВ МЕТОДОМ ИМПЕДАНСНОЙ СПЕКТРОСКОПИИ"

РЕЗЮМЕ

Работа направлена на получение композитных материалов ВДПЭ-PKR-3M и их исследование с использованием импедансной спектроскопии. Этот метод определяет комплексное сопротивление в широком диапазоне частот и анализирует полученный образец с использованием эквивалентных цепей, состоящих из идеальных резисторов, конденсаторов и катушек, все с одинаковой зависимостью от частоты. Импедансная спектроскопия предоставляет спектр для гетерогенных систем, разделяя электрически неоднородные области на основе диэлектрической проницаемости и проводимости в диаграмме Найквиста (зависимость действительной и мнимой частей импеданса, Z"=f(Z')). Эта диаграмма дает многокомпонентный спектр для областей с различными диэлектрическими свойствами, такими как идеальные резисторы, конденсаторы и катушки. С другой стороны, однородные области в электрической области, проявляющие характерный полукруг, могут быть проанализированы с использованием импедансной спектроскопии. Кроме того, любой фактор, влияющий на импеданс системы образец-электрод, может быть изучен с использованием импедансной спектроскопии.

Статья исследует подлинность действительных и мнимых компонентов импеданса, а также сдвига фаз (φ) для композитных образцов ВДПЭ+5% и ВДПЭ+10% PKR-3M относительно интенсивности внешнего электрического поля (23:10^6 Hs). Кроме того, построена диаграмма Найквиста на основе изменений интенсивности. Изученные образцы были получены с использованием метода горячего прессования.

КЛЮЧЕВЫЕ СЛОВА: 1-полиэтилен высокой плотности, 2-полимерный композит, 3-импеданс,4-спектроскопия, 5-пьезокерамические материалы, 6-диаграмма Найквиста

POLIMER KOMPOZİTLƏRİN İMPEDANS SPEKTROSKOPİYASI ÜSULU İLƏ TƏDQİQİ

XÜLASƏ

İşin məqsədi YSPE-PKR-3M kompozit materialları alıb onların impedans spektroskopiya üsulu ilə tədqiq etməkdir. Hansı ki, geniş tezliklər oblastında kompleks impedansı təyin edir və ideal rezistorlar,kondensatorlar və induktivlik sarğacından ibarət olan və tədqiq olunan nümunə ilə eyni tezlik aslılığına malik ekvivalent sxemlərin köməyi ilə analiz edir. Heterogen sistemlərin dielektrik nüfuzluğu və keçiriciliyi ilə fərqlənən elektrik cəhətdən heterogen oblastları Nyquist diaqramında (impedansın həqiqi və xəyali hissələrinin Z"=f(Z') aslılığı) çox komponentli spektr verir, lakin elektrik cəhətdən homogen oblastlar, hansılar ki, bir xarakterik yarmdariə verir. Nümunə-elektrod sistemini impedansına təsir edə biləcək hər bir faktor impedans spektroskopiya üsulunun köməyi ilə öyrənilə bilər.

Məqalədə YSPE+5% və YPSE+10% PKR-3M kompozit nümunələri üçün impendansın həqiqi və xəyali hissələrinin həmçinin φ faza sürüşməsinin xarici elektrik sahəsinin təzliyindən ($23:10^6$ Hs) aslılığı öyrənilmiş və tezliyin dəyişməsinə uyğun Nqyuist diaqrami qurulmuşdur.Tədqiq olunan nümunələr isti preslənmə üsulu ilə alınmışdır.

AÇAR SÖZLƏR: 1-yüksək sıxlıqlı polietilen, 2-polimer kompozit, 3-impedans,4-spektroskopiya, 5-pyezoelektrik keramika , 6-Nyquist diaqramı

INTRODUCTION:

Keramic materials and polymer composites prepared based on them are of interest both from a fundamental scientific standpoint and from an applied perspective. One such material is the PKR-3M piezoceramics ($PbTiO_3$-$PbZrO_3$-$PbNb_{2/3}Zn_{1/3}O_3$-$PbNb_{2/3}Mg_{1/3}O_3$-MnO_2) obtained at the Physics Research Institute of the Southern Federal University in Rostov, Russia. The use of these materials' dispersed particles (powder) as a filler is explained by their high piezoelectric parameters and extreme electro-physical characteristics, correlated with the presence of the morphotropic phase boundary (MPB) and structural phase transition.

It is worth noting that impedance spectroscopy, in addition to other informative methods like thermal activation spectroscopy, is one of the effective techniques that determine the correlation between the composition and macroscopic properties of the composite. With the help of this method, it becomes possible to identify and analyze the dielectric and electrical conductivity characteristics of materials, gather information about the transport of carriers by observing the real microstructure of the sample, and describe qualitatively and quantitatively the role of particle volume, surface, and interfaces of phases. Furthermore, the method allows for considering the influence of characteristic Maxwell-Wagner effects on non-uniform structures.

The presented work provides the initial results of the impedance spectroscopy study of HDPE+PKR-3M composite systems with various concentrations, obtained through hot pressing of a homogenous mixture of high-density polyethylene (HDPE) and PKR-3M piezoelectric ceramic powder.

RESEARCH METHOD:

The presented work provides the initial results of the investigation of a HDPE +PKR-3M composite system with varying concentrations, obtained by hot pressing a homogeneous mixture of high-density polyethylene (HDPE) and PKR-3M piezoelectric ceramic powder using the impedance spectroscopy method.

1.Sample Acquisition Process Involves the Following Stages:

The powders of the matrix and filler are sieved to obtain the respective dispersions.

Components are mixed in a ceramic crucible until a homogenous mixture is obtained.

From this mixture, samples with a thickness of ~200 μm and a diameter of 30 mm are obtained at a temperature of 373 K and a pressure of 15 MPa, with a 5-minute holding period.

Aluminum foil contacts with a thickness of 7 μm are applied to both surfaces of the samples.

The obtained disc-shaped experimental elements are rapidly quenched in an "ice-water" mixture.

The obtained samples have a 0-3 relationship, indicating a specific arrangement of filler particles within the matrix.

The investigation of HDPE+PKR-3M composites is conducted using a parallel combination of a resistor and a capacitor in a two-electrode scheme. Measurements are performed in a sandwich-type measurement chamber with the value of U=1V screened and combined. The measurements are carried out in a quasi-capacitor with a frequency range of (25-10^6) Hz. The measurements are conducted at a speed of 1 kHz. The examined samples are placed between electrodes made of non-corrosive stainless steel. Temperature is controlled using the MMX-400 electronic temperature controller. E7-20 type impedance measuring device with a broad frequency range is utilized to conduct the measurements.

Based on the experiments, the absolute value $|Z|(f)$ and the phase angle $\varphi(f)$ between the impedance and the voltage have been measured for the complete complex resistance. Subsequently, using the expressions $Z'(f) = |Z|(f)\cos\varphi(f)$ and $Z''(f) = |Z|(f)\sin\varphi(f)$, the spectra of the real and imaginary components of the complex impedance have been calculated appropriately. These measurements provide the opportunity to determine and analyze the electro-physical characteristics of the investigated samples. The relative error in impedance measurements has not exceeded 5%.

Frequency dependencies of the impedance of HDPE+5%PKR-3M composite samples.

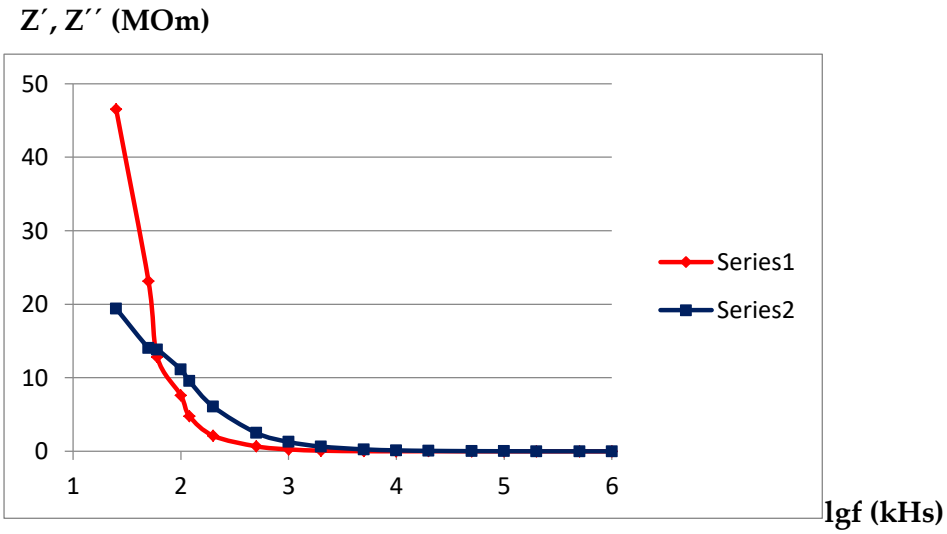

Figure 1. Frequency dependence of Z' (1) and Z'' (2) for HDPE+5% PKR-3M composite samples.

In Figure 1, the dependencies of the real (Z') and imaginary (Z'') components of the complex impedance on the frequency of the external electric field are presented. As observed in the figure, both Z' and Z'' sharply decrease with the increase in frequency (the rate of decrease for Z'' is significantly larger compared to Z'). It is noteworthy that, in the low-frequency range (f < 500), the increase in impedance is associated with the displacement of positive and negative charges towards the electrodes and the presence of a delicate layer characterized by significant electrical conduction in the proximity of the electrodes.[2] Therefore, measuring the impedance of polymer composites in various frequency ranges allows for distinguishing processes related to electrode (surface) and volume events, as well as determining important electro-physical characteristics of the investigated composites.

Selecting the equivalent circuit of the investigated composites and determining optimal values for the circuit elements are achieved by plotting the impedance spectra Z(f) obtained in experiments in Nyquist diagrams, representing the Z' real and Z'' imaginary components. It is evident that each point on the plot of the impedance locus reflects the real and imaginary components of the impedance measured at a specific frequency within the investigated frequency range.

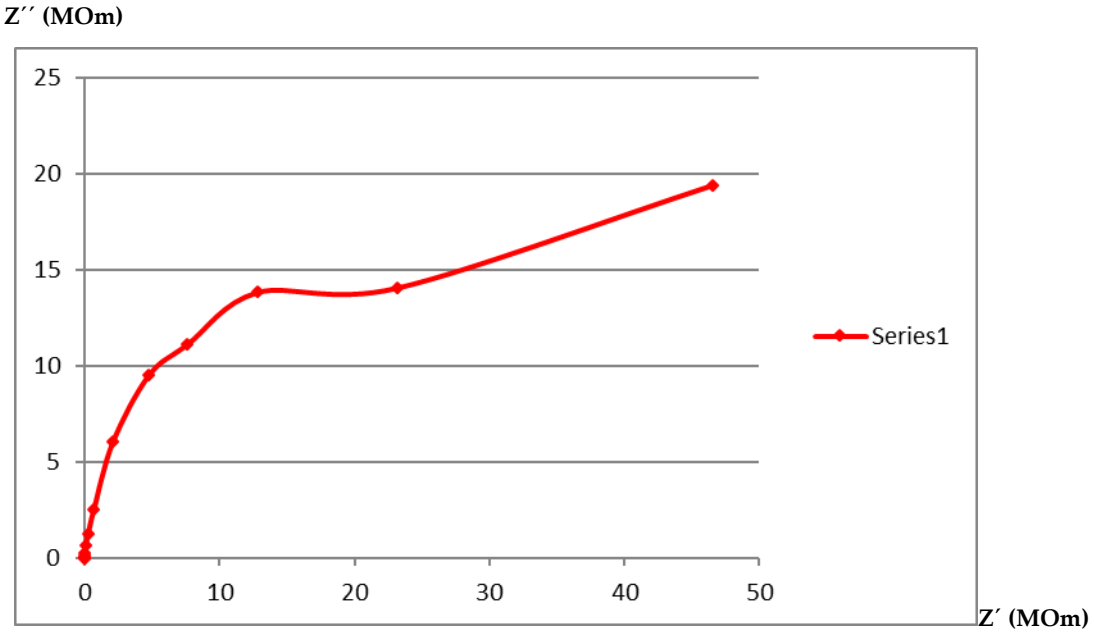

Figure 2. Nyquist diagram for HDPE+5% PKR-3M composite samples.

In Figure 2, the Nyquist diagram is shown for the HDPE+5% PKR-3M composite sample. The graph of Z'' as a function of Z' exhibits a globular shape at high frequencies and a linear segment at low frequencies. The relaxation frequency of the sample corresponding to the maximum value of Z'' on the semicircle of the diagram defines the relaxation time $\tau x=1/2\pi f\approx 5.31*10^{-3}$s, characterizing the molecular relaxation of the material [3].

2.The process of obtaining the samples combines the following stages:

The powders of the matrix and filler are passed through a sieve to obtain the respective dispersions.

The components are mixed in a ceramic crucible until a homogeneous mixture is obtained.

From this mixture, samples with a thickness of ~166 μm and a diameter of 30 mm are obtained at a temperature of 373 K and a pressure of 15 MPa, with a 5-minute holding period.

Aluminum foil contacts with a thickness of 7 μm are applied to both surfaces of the samples.

The obtained disc-shaped experimental elements are rapidly quenched in an "ice-water" mixture.

The obtained samples exhibit a 0-3 relationship, and the concentrations shown in the work are volume concentrations. The relative error in impedance measurements did not exceed 10%.

For the 90%HDPE+10%PKR-3M composite samples, the frequency dependencies of the impedance are investigated.

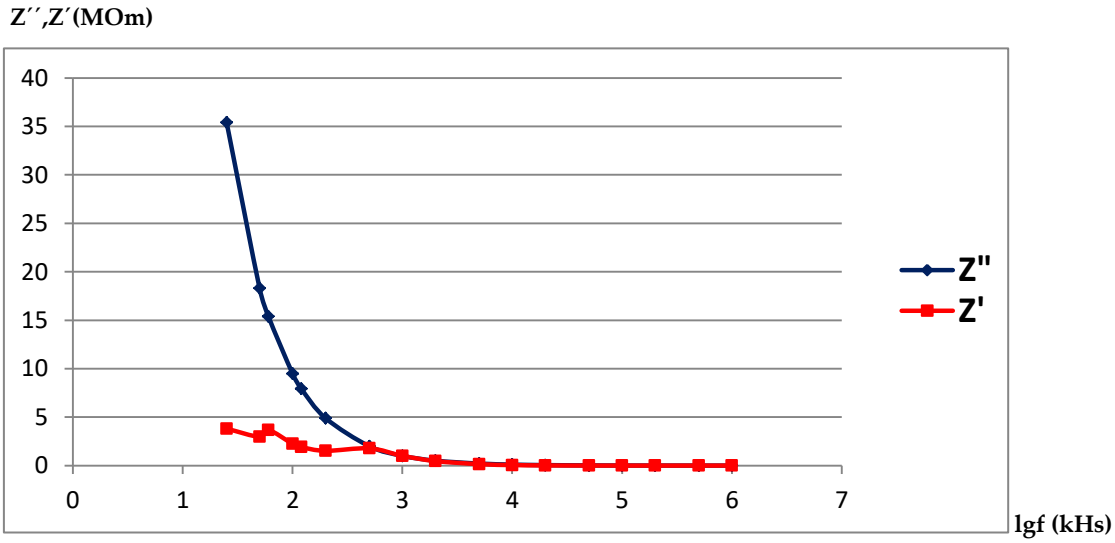

Figure 3. Frequency dependence of Z'' (1) and Z' (2) for HDPE+10% PKR-3M composite samples.

In Figure 1, the frequency dependencies of the real (Z') and imaginary (Z'') components of the complex impedance are provided as a function of the external electric field's frequency. As depicted in the figure, both Z' and Z'' sharply decrease with the increase in frequency (the rate of decrease for Z'' is significantly larger compared to Z'). It is noteworthy that, in the low-frequency range (f > 500), the increase in impedance is associated with the displacement of positive and negative charges towards electrodes of opposite signs and the presence of a delicate layer characterized by significant electrical conduction in the proximity of the electrodes.[2] Therefore, measuring the impedance of polymer composites in various frequency ranges allows for distinguishing processes related to surface and volume events that condition the current passing through the sample, as well as determining important electro-physical characteristics of the investigated composites.

RESULTS

HDPE+5% PKR-3M composite samples obtained by hot pressing were subjected to impedance spectroscopy, measuring the real and imaginary components Z′=|Z|cosφ and Z″=|Z|sinφ, as well as the frequency dependence of the phase shift φ between current and voltage.

In the Nyquist diagram, the characteristic relaxation time τx=5.31*10^-3s was calculated corresponding to the maximum of Z″.

Similarly, HDPE+10% PKR-3M composite samples obtained by hot pressing were analyzed using impedance spectroscopy, measuring the real and imaginary components Z′=|Z|cosφ and Z″=|Z|sinφ, along with the frequency dependence of the phase shift φ between current and voltage.

The φ angle dependence on frequency (lgf) was illustrated for the HDPE+10% PKR-3M composite sample.

It should be noted that addressing these issues requires a more comprehensive investigation of the electrical and dielectric properties of such composites.

REFERENCES

1. E.Barsukov,J.R.Macdonal. Impedance spectroscopy: theory, experiment and application.Willey,N.Y 2005, pages 595.
2. Б.А.Беляев, Н.А.Дрокин. Исследовние электрофизических характеристик границы электрод-жидкий кристалл методом импедасной спектроскопии.ФТТ, 2015,т.57,№1,170-175
3. Б.А.Беляев, Н.А.Дрокин, А.Н.Масленников Исследовние методом импедасной спуктроскопии допированных ионным сурфактантом жидких кристаллов.ФТТ, 2014,т.56,№7,1403-141
4. А.А. Лепешев, А.В. Павлов, Н.А. Дрокин Импедансная спектроскопия (BeO+TiO2)-керамики с добавкой наночастиц TiO2 Journal of Siberian Federal University. Engineering & Technologies, 2019, 12(3), 366-380
5. Carter, C.W. Impedance of networks containing resistances and two reactances. Bell Sys. Tech. J. 4:387-401; 1925. 6. Gabrielli, C., ed. Proceedings of the First International Symposium on Electrochemical Impedance Spectroscopy. Electrochim. Acta 35:1483-1670; S1-S18; 1990.

INSTRUCTIONS FOR AUTHORS

1. "The Baku Engineering University Journal-Physics" accepts original unpublished articles and reviews in the research field of the author.
2. Articles are accepted in English.
3. File format should be compatible with **Microsoft Word** and must be sent to the electronic mail (**journal@beu.edu.az**) of the Journal. The submitted article should follow the following format:

- Article title, author's name and surname
- The name of workplace
- Mail address
- Abstract and key words

4. The title of the article should be in each of the three languages of the abstract and should be centred on the page and in bold capitals before each summary.
5. **The abstract** should be written in **9 point** type size, between **100** and **150** words. The abstract should be written in the language of the text and in two more languages given above. The abstracts of the article written in each of the three languages should correspond to one another. The keywords should be written in two more languages besides the language of the article and should be at least three words.
6. . **UDC** and **PACS** index should be used in the article.
7. The article must consist of the followings:

- Introduction
- Research method and research
- Discussion of research method and its results
- In case the reference is in Russian it must be given in the Latin alphabet with the original language shown in brackets.

8. **Figures, pictures, graphics and tables** must be of publishing quality and inside the text. Figures, pictures and graphics should be captioned underneath, tables should be captioned above.
9. **References** should be given in square brackets in the text and listed according to the order inside the text at the end of the article. In order to cite the same reference twice or more, the appropriate pages should be given while keeping the numerical order. For example: [7, p.15].

Information about each of the given references should be full, clear and accurate. The bibliographic description of the reference should be cited according to its type (monograph, textbook, scientific research paper and etc.) While citing to scientific research articles, materials of symposiums, conferences and other popular scientific events, the name of the article, lecture or paper should be given.

Samples:

a) ***Article:*** Demukhamedova S.D., Aliyeva İ.N., Godjayev N.M.. *Spatial and electronic structure af monomerrik and dimeric conapeetes of carnosine üith zinc,* Journal of structural Chemistry, Vol.51, No.5, p.824-832, 2010

b) ***Book:*** Christie ohn Geankoplis. *Transport Processes and Separation Process Principles.* Fourth Edition, Prentice Hall, p.386-398, 2002

c) ***Conference paper:*** Sadychov F.S., Aydın C., Ahmedov A.İ.. Appligation of Information – Commu-nication Technologies in Science and education. II International Conference."*Higher Twist Effects In Photon- Proton Collisions", Bakı, 01-03 Noyabr, 2007, ss 384-391*

References should be in 9-point type size.

10. The margins sizes of the page: - Top 2.8 cm. bottom 2.8 cm. left 2.5 cm, right 2.5 cm. The article main text should be written in Palatino Linotype 11 point type size single-spaced. Paragraph spacing should be 6 point.
11. The maximum number of pages for an article should not exceed 15 pages
12. The decision to publish a given article is made through the following procedures:

- The article is sent to at least to experts.
- The article is sent back to the author to make amendments upon the recommendations of referees.
- After author makes amendments upon the recommendations of referees the article can be sent for the publication by the Editorial Board of the journal.

YAZI VƏ NƏŞR QAYDALARI

1. "Journal of Baku Engineering University" Fizika- əvvəllər nəşr olunmamış orijinal əsərləri və müəllifin tədqiqat sahəsi üzrə yazılmış icmal məqalələri qəbul edir.
2. Məqalələr İngilis dilində qəbul edilir.
3. Yazılar **Microsoft Word** yazı proqramında, (**journal@beu.edu.az**) ünvanına göndərilməlidir. Göndərilən məqalələrdə aşağıdakılara nəzərə alınmalıdır:

- Məqalənin başlığı, müəllifin adı, soyadı,
- İş yeri,
- Elektron ünvanı,
- Xülasə və açar sözlər.

4. **Məqalədə başlıq hər xülasədən əvvəl** ortada, qara və böyük hərflə xülasələrin yazıldığı hər üç dildə olmalıdır.
5. **Xülasə** 100-150 söz aralığında olmaqla, 9 punto yazı tipi böyüklüyündə, məqalənin yazıldığı dildə və bundan əlavə yuxarıda göstərilən iki dildə olmalıdır. Məqalənin hər üç dildə yazılmış xülasəsi bir-birinin eyni olmalıdır. Açar sözlər uyğun xülasələrin sonunda onun yazıldığı dildə verilməklə ən azı üç sözdən ibarət olmalıdır.
6. Məqalədə UOT və PACS kodları göstərilməlidir.
7. Məqalə aşağıdakılardan ibarət olmalıdır:

- Giriş,
- Tədqiqat metodu
- Tədqiqat işinin müzakirəsi və onun nəticələri,
- İstinad ədəbiyyatı rus dilində olduğu halda orjinal dili mötərzə içərisində göstərməklə yalnız Latın əlifbası ilə verilməlidir.

8. **Şəkil**, **rəsm**, **grafik** və **cədvəllər** çapda düzgün, aydın çıxacaq vəziyyətdə və mətn içərisində olmalıdır. Şəkil, rəsm və grafiklərin yazıları onların altında yazılmalıdır. Cədvəllərdə başlıq cədvəlin üstündə yazılmalıdır.
9. **Mənbələr** mətn içərisində kvadrat mötərizə daxilində göstərilməklə məqalənin sonunda mətn daxilindəki sıra ilə düzülməlidir. Eyni mənbəyə iki və daha cox istinad edildikdə əvvəlki sıra sayı saxlanmaqla müvafiq səhifələr göstərilməlidir. Məsələn: [7,səh.15].

Ədəbiyyat siyahısında verilən hər bir istinad haqqında məlumat tam və dəqiq olmalıdır. İstinad olunan mənbənin biblioqrafik təsviri onun növündən (monoqrafiya, dərslik, elmi məqalə və s.) asılı olaraq verilməlidir. Elmi məqalələrə, simpozium, konfrans, və digər nüfuzlu elmi tədbirlərin materiallarına və ya tezislərinə istinad edərkən məqalənin, məruzənin və ya tezisin adı göstərilməlidir.

Nümunələr:

a) ***Məqalə:*** Demukhamedova S.D., Aliyeva İ.N., Godjayev N.M.. *Spatial and electronic structure af monomeric and dimeric complexes of carnosine with zinc,* Journal of structural Chemistry, Vol.51, No.5, p.824-832, 2010

b) ***Kitab:*** Christie ohn Geankoplis. *Transport Processes and Separation Process Principles*. Fourth Edition, Prentice Hall, 2002

c) ***Konfrans:*** Sadychov F.S., Aydın C., Ahmedov A.İ.. Appligation of Information-Communication Technologies in Science and education. II International Conference. "*Higher Twist Effects In Photon- Proton Collisions", Bakı, 01-03 Noyabr, 2007, ss 384-391*

Mənbələr 9 punto yazı tipi böyüklüyündə olmalıdır.

10. **Səhifə ölçüləri:** üstdən 2.8 sm, altdan 2.8 sm, soldan 2.5 sm və sağdan 2.5 sm olmalıdır. Mətn 11 punto yazı tipi böyüklüyündə, **Palatino Linotype** yazı tipi ilə və tək simvol aralığında yazılmalıdır. Paraqraflar arasında 6 punto yazı tipi aralığında məsafə olmalıdır.
11. Orijinal tədqiqat əsərlərinin tam mətni bir qayda olaraq 15 səhifədən artıq olmamalıdır.
12. Məqalənin nəşrə təqdimi aşağıdakı qaydada aparılır:

- Hər məqallə ən azı iki ekspertə göndərilir.
- Ekspertlərin tövsiyələrini nəzərə almaq üçün məqalə müəllifə göndərilir.
- Məqalə, ekspertlərin tənqidi qeydləri müəllif tərəfindən nəzərə alındıqdan sonra Jurnalın Redaksiya Heyəti tərəfindən çapa təqdim oluna bilər.

YAZIM KURALLARI

1. "Journal of Baku Engineering University-Physics" önceler yayımlanmamış orijinal çalışmaları ve yazarın kendi araştırma alanın-da yazılmış derleme makaleleri kabul etmektedir.
2. Makaleler İngilizce kabul edilir.
3. Makaleler Microsoft Word yazı programında, (**journal@beu.edu.az**) adresine gönderilmelidir. Gönderilen makalelerde şunlar dikkate alınmalıdır:

- Makalenin başlığı, yazarın adı, soyadı,
- İş yeri,
- E-posta adresi,
- Özet ve anahtar kelimeler.

4. **Özet** 100-150 kelime arasında olup 9 font büyüklüğünde, makalenin yazıldığı dilde ve yukarıda belirtilen iki dilde olmalıdır. Makalenin her üç dilde yazılmış özeti birbirinin aynı olmalıdır. Anahtar kelimeler uygun özetin sonunda onun yazıldığı dilde verilmekle en az üç sözcükten oluşmalıdır.
5. Makalede UOT ve PACS tipli kodlar gösterilmelidir.
6. Makale şunlardan oluşmalıdır:

- Giriş,
- Araştırma yöntemi
- Araştırma
- Tartışma ve sonuçlar,
- İstinat Edebiyatı Rusça olduğu halde orjinal dili parantez içerisinde göstermekle yalnız Latin alfabesi ile verilmelidir.

7. **Şekil, Resim, Grafik** ve **Tablolar** baskıda düzgün çıkacak nitelikte ve metin içerisinde olmalıdır. Şekil, Resim ve grafiklerin yazıları onların alt kısımda yer almalıdır. Tablolarda ise başlık, tablonun üst kısmında bulunmalıdır.
8. **Kullanılan kaynaklar**, metin dâhilinde köşeli parantez içerisinde numaralandırılmalı, aynı sırayla metin sonunda gösterilmelidir. Aynı kaynaklara tekrar başvurulduğunda sıra muhafaza edilmelidir. Örneğin: [7,seh.15].

Referans verilen her bir kaynağın künyesi tam ve kesin olmalıdır. Referans gösterilen kaynağın türü de eserin türüne (monografi, derslik, ilmî makale vs.) uygun olarak verilmelidir. İlmi makalelere, sempozyum, ve konferanslara müracaat ederken makalenin, bildirinin veya bildiri özetlerinin adı da gösterilmelidir.

Örnekler:

a) ***Makale:*** Demukhamedova S.D., Aliyeva İ.N., Godjayev N.M.. *Spatial and Electronic Structure of Monomerik and Dimeric Conapeetes of Carnosine Üith Zinc,* Journal of Structural Chemistry, Vol.51, No.5, p.824-832, 2010

b) ***Kitap:*** Christie ohn Geankoplis. *Transport Processes and Separation Process Principles.* Fourth Edition, Prentice Hall, p.386-398, 2002

c) ***Kongre:*** Sadychov F.S., Aydın C., Ahmedov A.İ. Appligation of Information-Communication Technologies in Science and education. II International Conference. "*Higher Twist Effects In Photon- Proton Collisions", Bakı, 01-03 Noyabr, 2007, ss 384-391*

Kaynakların büyüklüğü 9 punto olmalıdır.

9. **Sayfa ölçüleri**; üst: 2.8 cm, alt: 2.8 cm, sol: 2.5 cm, sağ: 2.5 cm şeklinde olmalıdır. Metin 11 punto büyüklükte **Palatino Linotype** fontu ile ve tek aralıkta yazılmalıdır. Paragraflar arasında 6 puntoluk yazı mesafesinde olmalıdır.
10. Orijinal araştırma eserlerinin tam metni 15 sayfadan fazla olmamalıdır.
11. Makaleler dergi editör kurulunun kararı ile yayımlanır. Editörler makaleyi düzeltme için yazara geri gönderilebilir.
12. Makalenin yayına sunuşu aşağıdaki şekilde yapılır:

- Her makale en az iki uzmana gönderilir.
- Uzmanların tavsiyelerini dikkate almak için makale yazara gönderilir.
- Makale, uzmanların eleştirel notları yazar tarafından dikkate alındıktan sonra Derginin Yayın Kurulu tarafından yayına sunulabilir.

13. Azerbaycan dışından gönderilen ve yayımlanacak olan makaleler için,(derginin kendilerine gonderilmesi zamani posta karşılığı) 30 ABD Doları veya karşılığı TL, T.C. Ziraat Bankası/Üsküdar-İstanbul 0403 0050 5917 No'lu hesaba yatırılmalı ve makbuzu üniversitemize fakslanmalıdır.

ПРАВИЛА ДЛЯ АВТОРОВ

1. «Journal of Baku Engineering University» - Физика публикует оригинальные, научные статьи из области исследования автора и ранее не опубликованные.
2. Статьи принимаются на английском языке.
3. Рукописи должны быть набраны согласно программы **Microsoft Word** и отправлены на электронный адрес **(journal@beu.edu.az)**. Отправляемые статьи должны учитывать следующие правила:

- Название статьи, имя и фамилия авторов
- Место работы
- Электронный адрес
- Аннотация и ключевые слова

4. **Заглавие статьи** пишется для каждой аннотации заглавными буквами, жирными буквами и располагается по центру. Заглавие и аннотации должны быть представлены на трех языках.
5. **Аннотация**, написанная на языке представленной статьи, должна содержать 100-150 слов, набранных шрифтом 9 punto. Кроме того, представляются аннотации на двух других выше указанных языках, перевод которых соответствует содержанию оригинала. Ключевые слова должны быть представлены после каждой аннотации на его языке и содержать не менее 3-х слов.
6. В статье должны быть указаны коды UOT и PACS.
7. Представленные статьи должны содержать:

- Введение
- Метод исследования
- Обсуждение результатов исследования и выводов.
- Если ссылаются на работу на русском языке, тогда оригинальный язык указывается в скобках, а ссылка дается только на латинском алфавите.

8. **Рисунки, картинки, графики и таблицы** должны быть четко выполнены и размещены внутри статьи. Подписи к рисункам размещаются под рисунком, картинкой или графиком. Название таблицы пишется над таблицей.
9. **Ссылки** на источники даются в тексте цифрой в квадратных скобках и располагаются в конце статьи в порядке цитирования в тексте. Если на один и тот же источник ссылаются два и более раз, необходимо указать соответствующую страницу, сохраняя порядковый номер цитирования. Например: [7, стр.15]. Библиографическое описание ссылаемой литературы должно быть проведено с учетом типа источника (монография, учебник, научная статья и др.). При ссылке на научную статью, материалы симпозиума, конференции или других значимых научных мероприятий должны быть указаны название статьи, доклада или тезиса.

Например:

a) ***Статья:*** Demukhamedova S.D., Aliyeva I.N., Godjayev N.M. *Spatial and electronic structure of monomeric and dimeric complexes of carnosine with zinc,* Journal of Structural Chemistry, Vol.51, No.5, p.824-832, 2010

b) ***Книга:*** Christie on Geankoplis. *Transport Processes and Separation Process Principles.* Fourth Edition, Prentice Hall, 2002

c) ***Конференция:*** Sadychov F.S, Fydin C,Ahmedov A.I. Appligation of Information-Communication Nechnologies in Science and education. II International Conference. *"Higher Twist Effects In Photon-Proton Collision",* Bakı,01-03 Noyabr, 2007, ss.384-391

Список цитированной литературы набирается шрифтом 9 punto.

10. **Размеры страницы:** сверху 2.8 см, снизу 2.8 см, слева 2.5 и справа 2.5. Текст печатается шрифтом **Palatino Linotype**, размер шрифта 11 punto, интервал-одинарный. Параграфы должны быть разделены расстоянием, соответствующим интервалу 6 punto.
11. Полный объем оригинальной статьи, как правило, не должен превышать 15 страниц.
12. Представление статьи к печати производится в ниже указанном порядке:

- Каждая статья посылается не менее двум экспертам.
- Статья посылается автору для учета замечаний экспертов.
- Статья, после того, как автор учел замечания экспертов, редакционной коллегией журнала может быть рекомендована к печати.